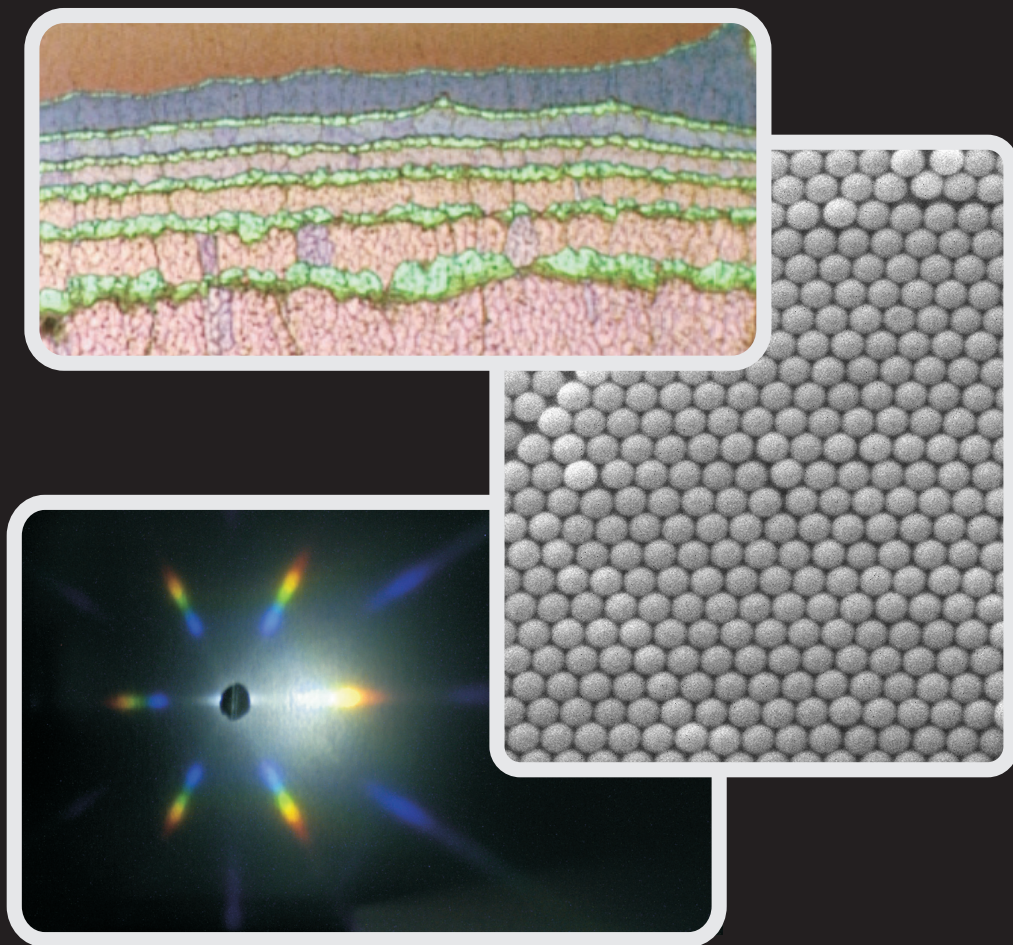


# An optical study of opal based photonic crystals



Juan Francisco Galisteo López  
Madrid 2005



# **AN OPTICAL STUDY OF OPAL BASED PHOTONIC CRYSTALS**

Un estudio óptico de cristales fotónicos basados en ópalos

Memoria presentada para optar al Grado de Doctor en  
Ciencias Físicas por:

**Juan Francisco Galisteo López**

Director:

**Dr. Ceferino López Fernández**

Tutora:

**Dra. Luisa E. Bausá López**

Departamento de Física de Materiales  
Facultad de Ciencias  
Universidad Autónoma de Madrid

Instituto de Ciencia de Materiales de Madrid  
Consejo Superior de Investigaciones Científicas

Junio 2005

Tesis defendida el 6 de junio de 2005 en el Departamento de Física de Materiales  
de la Universidad Autónoma de Madrid

Tribunal: Prof. Luis Viña Liste  
Prof. Willem L. Vos  
Prof. Juan José Sáenz Gutiérrez  
Dr. Hernán Míguez García  
Prof. Jordi Martorell Pena

Impreso en ICMM-CSIC, Madrid, España  
ISBN: 84-689-2810-0

*A mis padres.*  
*A Patricia.*



## Agradecimientos:

A lo largo de estos años han sido muchas las personas que, de una forma u otra, han contribuido a que este trabajo saliese adelante. En primer lugar me gustaría agradecer a mi director de tesis, Cefe López, por haberme acogido en su grupo y haberme dado la oportunidad de trabajar y aprender en él. Por haber puesto la ilusión y el escepticismo en los momentos adecuados para que todo saliese adelante.

Aan het begin van mijn wetenschappelijke carrière had ik het genoeg om bij de Universiteit van Amsterdam onder de supervisie van Prof. Willem Vos te werken. Ik zou hem voor zijn steun tijdens die tijd en voor het maken van het een prettige ervaring willen danken.

Para la realización del trabajo contenido en esta memoria conté con la ayuda inestimable de una serie de personas:

En el capítulo 2 me gustaría agradecer a la Dra. E. Palacios y a E. Martínez por los coloides de PS y PMMA y a Beatriz Hernández por las discusiones y consejos.

Al Prof. Carlos Zaldo por permitirme emplear la esfera integradora para los resultados presentados en el capítulo 3. A la Dra. E. Palacios por el crecimiento de algunas muestras y la ayuda en la caracterización óptica.

A la Dra. Luisa E. Bausá del Departamento de Física de Materiales de la Universidad Autónoma de Madrid por permitirme emplear el MOPO para las fotografías del capítulo 4. Al Dr. Florencio García-Santamaría por las discusiones y las valiosas ideas aportadas. A la doctora Rosalía Serna del Instituto de Óptica “Daza de Valdés” por ayudarme con las medidas de elipsometría.

Al Dr. Matteo Galli del Dipartimento di Fisica “A. Volta” de la Universidad de Pavía por su ayuda con las medidas de interferometría de luz blanca del capítulo 5. También por las discusiones en la interpretación de los mismos junto al Prof. Claudio Andreani.

Al Dr. Fernando López Tejeira y al Dr. José Sanchez-Dehesa del Departamento de Física de la Materia Condensada de la Universidad Autónoma de Madrid por los cálculos de bandas y las discusiones que dieron lugar a los resultados presentados en el capítulo 6.

A los doctores Femius Koenderink, Gijs van Soest y Jaime Gómez-Rivas y a Wim Koops, del grupo “Waves in Complex Media” de la Universidad de Ámsterdam, por el apoyo experimental para llevar a cabo el montaje con el que se realizaron las medidas presentadas en el capítulo 7.

Durante el período de trabajo en la Universidad de Ámsterdam, conté con la financiación de la fundación “Stichting voor Fundamenteel Onderzoek der Materie” (FOM). Durante el período de trabajo en el ICMM-CSIC conté con la financiación del proyecto MAT2003-01237 del Ministerio de Ciencia y Tecnología así como del proyecto PHOREMOST de la Comunidad Europea. Las estancias en

la Universidad de Pavía fueron posibles gracias a la financiación de los proyectos PHOREMOST (Comunidad Europea) y COST-P11 (European Science Foundation).

En este tiempo he colaborado con mucha gente, siendo los más cercanos los miembros del grupo dirigido por el Dr. Cefe López en el Instituto de Ciencia de Materiales de Madrid (ICMM-CSIC). Todos ellos han hecho que estos años hayan sido un período de aprendizaje a muchos niveles. En primer lugar quisiera agradecer a Bea, con quien he compartido despacho del primer al último día, por estos años en los que tanto he disfrutado. A Floren, con quien pasé grandes momentos compartiendo despacho y discutiendo. Espero que en el futuro podamos trabajar juntos de nuevo, porque fue un placer. A Álvaro, que siempre estuvo cerca para discutir resultados o para quitarle peso a la cosa con una buena broma y ayudar a recuperar la objetividad. A Lola Golmayo, aportando su experiencia para que todo fuese mejor. A David quien, a pesar de llevar poco tiempo entre nosotros, introdujo nuevos aires y buenos momentos. A los teóricos de la UAM, José Sanchez-Dehesa (gracias por esas discusiones, con las que tanto aprendí) y a Fernando López-Tejeira. A la conexión de Valencia, Marta, Silvia, Isabelle, Roberto y el Profesor Francisco Meseguer. Y a toda la gente que pasó por el grupo y fue dejando rastro, Elisabeth, Elisa, Antonio...

También dentro del ICMM hubo mucha gente con la que no llegué a colaborar científicamente pero con los que compartí buenos momentos; Angel Muñoz, siempre dispuesto a echar una mano, Carlos Prieto y sus chicos, Merche, Felix e Isa, José Ángel Gago, Nieves, Ricardo, Joaquín, el grupo de Teatro (por poner un toque artístico entre tanta ciencia), Marisa (por hacer de mi despacho un sitio habitable), etc.

During my stay at the University of Amsterdam I had the opportunity to work with a number of people I would like to thank. Femius (who survived sharing an office with me), Gijs (por enseñarme Amsterdam y por los intercambios culturales), Manu, Lydia, Wim, Jaime, Denis, Martijn, Boris, Patrick and Yuri (un gran científico y mejor persona, con quien fue un placer “platicar” y aprender). I would also like to thank Prof. Ad Lagendijk for his support and for hosting me in his group during that time.

Near the end of my thesis I spent some weeks at the Dipartimento di Fisica “A. Volta”, at the University of Pavia and I would like to thank all the people with whom I interacted; Prof. Claudio Andreani for hosting me in his group and for enjoyable scientific discussions; Dr. Maddalena Patrini for making my stay possible; all the guys in the group, Daniele, Marco, Gabriele, etc; and specially Dr. Matteo Galli, with whom I enjoyed some exhausting measurement days and scientific discussions.

Fuera del ámbito científico ha habido mucha gente con la que he compartido este tiempo, y sin la ayuda de los cuales esto no hubiese posible. Maria, inmigrante

perpetua y eterna compañera durante estos años, desde California a Laciana pasando por el Raval, que se sigan repitiendo las visitas; Mercedes, siempre estableciéndose y a punto de partir, gracias por estar siempre ahí; Alberto, dándome siempre su apoyo desde su exilio francés; Dani e Ici, gracias por rescatarme en los momentos adecuados, en Delft o Alcorcón; Dani, profesor por las tierras manchegas; Natalia; Marian y Laura.

Quiero agradecer a mis padres su apoyo y su cariño incondicionales durante todo este tiempo. Por todo lo que de ellos, y con ellos, he aprendido.

Finalmente me gustaría agradecer a Patricia, la persona que me ha acompañado a lo largo de todos estos años. Porque ha sido un placer haber hecho este viaje contigo.

Madrid, Junio 2005



*Ever tried. Ever failed. No matter. Try Again. Fail again. Fail better.*

*Samuel Beckett*



## GENERAL INDEX:

### CHAPTER 1

<b>Introduction: Photonic crystals .....</b>	<b>9</b>
1. Photonic Crystals .....	9
2. Energy bands in Photonic Crystals .....	11
3. Fabrication methods.....	15
4. Applications .....	18
5. Defects in Photonic Crystals.....	20
6. This thesis .....	21
7. References.....	22

### CHAPTER 2

<b>Fabrication and structural characterization of artificial opals .....</b>	<b>25</b>
1. Introduction.....	25
2. Vertical deposition method .....	26
3. Structural characterization .....	29
4. Conclusions and future work .....	37
5. References.....	39

### CHAPTER 3

<b>Optical study of the L-pseudogap in thin film opals .....</b>	<b>41</b>
1. Introduction.....	41
2. Optical properties: finite size effects .....	42
3. Effects of disorder.....	48
4. Angle resolved measurements .....	55
5. Conclusions and future work .....	62
6. References.....	63

### CHAPTER 4

<b>Optical properties of artificial opals in the high energy regime .....</b>	<b>65</b>
1. Introduction.....	65
2. Optical properties: scalability and finite size effects .....	66
3. Physical origin of the bands .....	70
4. Diffraction in photonic crystals .....	74
5. Comparison with band structure .....	78
6. Conclusions and future work .....	86
7. References.....	88

**CHAPTER 5**

**White light interferometry of thin film opals ..... 91**

- 1. Introduction..... 91
- 2. Experimental ..... 92
- 3. Low energy spectral region..... 95
- 4. High energy spectral region ..... 101
- 5. Conclusions and future work ..... 106
- 6. References..... 107

**CHAPTER 6**

**Polarization dependence of the optical response of artificial opals ..... 109**

- 1. Introduction..... 109
- 2. Symmetry of photonic bands and incident beam ..... 110
- 3. Angle resolved reflectivity..... 111
- 4. Conclusions and future work..... 114
- 5. References..... 115

**CHAPTER 7**

**Angle resolved reflectivity of single-domain photonic crystals: Effects of disorder ..... 117**

- 1. Introduction..... 117
- 2. Experimental ..... 118
- 3. Determination of mosaic spread ..... 119
- 4. Angle resolved reflectivity..... 121
- 5. Effects of disorder..... 124
- 6. Conclusions and future work ..... 125
- 7. References..... 127

**Appendix 1**

**Photonic band structures for opal based systems: PWEM vs. SWA..... 129**

**Appendix 2**

**Infiltration of polystyrene thin film opals with SiO<sub>2</sub>.....135**

**Conclusiones generales.....137**

**Lista de publicaciones.....139**

# CHAPTER 1

---

## Introduction: Photonic crystals

### 1. Photonic Crystals

Photonic crystals are a type of artificial structures which, over the past two decades, have emerged as a promising means to control the radiation dynamics of active materials and the propagation of electromagnetic radiation in ways not permitted by conventional materials.

In essence, a photonic crystal is a material in which the refractive index is periodically modulated on a length scale comparable to the wavelength of light. In this sense, the simplest photonic crystal one can consider is the dielectric stack or Bragg reflector, in which the periodicity takes place along one dimension. In such a system, the shape of the dispersion relation deviates from that of the constituent materials appearing as a set of allowed and forbidden frequency intervals (see figure 1). The appearance of such forbidden intervals or “gaps” is a consequence of Bragg diffraction by the planes forming the crystal, and their spectral position and width are determined both by the period and the refractive indices of the constituent materials. For those frequencies contained within these gaps, the associated wave vector takes on imaginary values and light propagating along the crystal with those frequencies is exponentially attenuated.

Although Bragg reflectors have been thoroughly studied over the past few decades and their optical properties are well understood,<sup>1</sup> it is when the periodicity is extended to the three dimensions of space that the full potential of such structures is achieved. In this situation, one expects to find the aforementioned gaps along each direction of propagation within the crystal. In principle, forbidden intervals may not necessarily span the same spectral region for different directions, and one may then speak of “pseudogaps”. But under certain conditions regarding the amplitude of the refractive index modulation, the symmetry of the lattice, its topology and the filling fraction of the constituent materials one may reach a situation where gaps for all directions within the crystal share a common frequency range. Such spectral range is known as a photonic band gap (PBG); a frequency interval for which no light may propagate within the crystal regardless of its

direction. A PBG can only take place in 3D photonic crystals and has become, since the first proposal of such structures,<sup>2,3</sup> the most sought for phenomenon in photonic crystal research. This is due to the fact that the density of electromagnetic modes (DOS) vanishes for those frequencies contained in the PBG, and spontaneous emission of light sources located within the crystal may be completely inhibited.

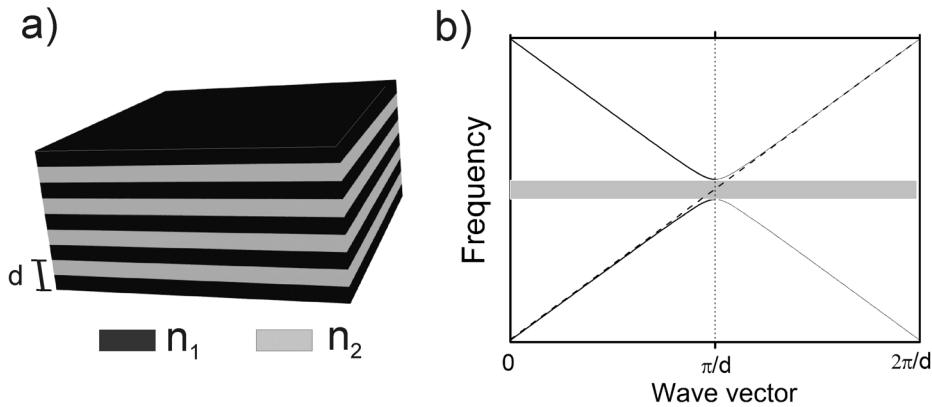


Figure 1: (a) Bragg mirror consisting of alternating dielectric layers with refractive index  $n_1$  and  $n_2$  with period “ $d$ ”. (b) Dispersion relation for propagation parallel to the direction of periodicity (solid line), and dispersion relation for a homogeneous medium (dashed line). Grey box indicates a forbidden frequency interval.

Although of utmost importance, the existence of a PBG is not the only characteristic which makes photonic crystals fascinating materials. The DOS may not only be reduced but also enhanced by appropriately tailoring the crystal. Thus the strength of the optical field within the crystal may be enhanced, which constitutes an advantage if dealing with optically active constituents.

In terms of light propagation within the crystal, the existence of a 2D or 3D periodicity allows for the observation of anomalous refraction effects. By anomalous we refer to deviations from predictions of Snell’s law, which properly describes light refraction in conventional unstructured materials. Super-prism effects<sup>4</sup> (where large steering of the refracted beam takes place for small variations of the wavelength or direction of the incident one) or even negative refraction<sup>5</sup> have been predicted for 2D and 3D systems and experimentally observed in the former.

In this chapter a brief review of certain topics concerning photonic crystal research will be given which will help in both, introducing and understanding the work presented in this memory. Section 2 deals with dispersion relations in photonic crystals, as a tool for describing the optical properties of such systems.

Once the theory behind photonic crystals is introduced, in section 3 the different approaches to the fabrication of 3D systems are reviewed. After introducing some of the proposed applications for these systems in section 4, the important issue of defects in photonic crystals will be dealt with in section 5. Finally, a summary of the material contained in the following chapters, and which constitutes the body of the thesis, will be given.

## 2. Energy bands in Photonic Crystals

The optical properties of a photonic crystal are directly related to its dispersion relation. In this sense, dispersion relations or photonic band structures (as commonly termed due to their similarity with electronic bands in solids) have been used both as design tools for predicting systems with given optical properties and as a means to interpret the optical response of fabricated structures. In deriving the dispersion relation of a photonic crystal, a number of concepts from solid state physics (Brillouin Zone, reciprocal lattice, etc.) are used due to the similarity of the problem of photons in a periodic refractive index and electrons in a periodic potential. As a matter of fact most band structure calculation methods have been borrowed from the electronic case.

The starting point for determining the photonic band structure of a PC is Maxwell's equations which, in the absence of charges or currents, may be expressed as:

$$\begin{aligned}\nabla \times \mathbf{H}(\mathbf{r},t) - \frac{1}{c} \frac{\partial \mathbf{D}(\mathbf{r},t)}{\partial t} &= 0, \quad \nabla \cdot \mathbf{B}(\mathbf{r},t) = 0 \\ \nabla \times \mathbf{E}(\mathbf{r},t) + \frac{1}{c} \frac{\partial \mathbf{B}(\mathbf{r},t)}{\partial t} &= 0, \quad \nabla \cdot \mathbf{D}(\mathbf{r},t) = 0\end{aligned}\tag{1}$$

Next we make use of the constitutive relations which relate  $\mathbf{E}(\mathbf{r},t)$  to  $\mathbf{D}(\mathbf{r},t)$  and  $\mathbf{B}(\mathbf{r},t)$  to  $\mathbf{H}(\mathbf{r},t)$ . Although these relations may take on a complicated form, a simplified expression may be obtained if one assumes non-magnetic, linear, isotropic and lossless materials, together with the fact that their dielectric constant is not frequency dependent. In this situation we have:

$$\begin{aligned}\mathbf{D}(\mathbf{r},t) &= \varepsilon(\mathbf{r}) \cdot \mathbf{E}(\mathbf{r},t) \\ \mathbf{H}(\mathbf{r},t) &= \mathbf{B}(\mathbf{r},t)\end{aligned}\tag{2}$$

Combining (1) with (2) we obtain a wave equation for any of the fields. It is the one for the magnetic field that is usually employed. Separating  $\mathbf{H}(\mathbf{r},t)$  into a spatial field pattern times a harmonically varying temporal part we obtain the following wave equation:

$$\nabla \times \left[ \frac{1}{\varepsilon(\mathbf{r})} \nabla \times \mathbf{H}(\mathbf{r}) \right] = \frac{c^2}{\omega^2} \mathbf{H}(\mathbf{r}) \quad (3)$$

This equation has the form of an eigenvalue problem with eigenvectors  $\mathbf{H}(\mathbf{r})$  and eigenvalues  $(\omega/c)^2$ . The choice for solving this particular equation is due to the fact that the operator acting on  $\mathbf{H}(\mathbf{r})$  is a Hermitian one, which simplifies the problem. The most common approach to solve (3) is the use of the plane wave expansion method (PWEM),<sup>6</sup> adapted from electronic band structure theory. Due to the existence of a discrete translational symmetry in the system Bloch's theorem can be applied to the eigenvectors  $\mathbf{H}(\mathbf{r})$  which can therefore be expressed as the product:

$$\mathbf{H}(\mathbf{r}) = \mathbf{u}_{\mathbf{k}n}(\mathbf{r}) e^{i\mathbf{k}\mathbf{r}} \quad (4)$$

where  $\mathbf{u}_{\mathbf{k}n}(\mathbf{r})$  is a periodic function having the periodicity of the lattice and  $\mathbf{k}$  is a wave vector contained in the first Brillouin zone. Constraining the solutions to the first Brillouin zone causes a folding of the dispersion relation which organizes into bands labeled with the integer  $n$ .

The periodic functions  $\mathbf{u}_{\mathbf{k}n}(\mathbf{r})$  and  $\varepsilon(\mathbf{r})^{-1}$  can be expanded into a Fourier series over the reciprocal lattice vectors  $\mathbf{G}$ :

$$u_{n\mathbf{k}}(\mathbf{r}) = \sum_{\mathbf{G}} \mathbf{u}_{n\mathbf{k}}^{\mathbf{G}} e^{i\mathbf{G}\mathbf{r}}, \quad \frac{1}{\varepsilon(\mathbf{r})} = \sum_{\mathbf{G}} \eta_{\mathbf{G}} e^{i\mathbf{G}\mathbf{r}} \quad (5)$$

Insertion of (4) and (5) into (3) yields a system of  $2N$  equations for each wave vector  $\mathbf{k}$  in the first Brillouin zone. Here  $N$  is the number of plane waves considered in the expansion in (5), and the factor 2 accounts for the two polarizations. Obtaining the dispersion relation is then reduced to the diagonalization of a  $2N \times 2N$  matrix, where a large enough  $N$  is needed to yield good accuracy.

Approximate solutions of the problem may be obtained using the so called scalar wave approximation (SWA)<sup>7</sup> in the two band model. In this approach the vectorial nature of the field is neglected and only two terms from the expansion of  $\mathbf{u}_{\mathbf{k}n}(\mathbf{r})$  and the dielectric constant are retained. This simplifies the problem and an analytical expression may be obtained for the dispersion relation of the crystal which, for certain systems, may yield results close to the exact ones (see appendix 1).

Figure 2 shows two band structures calculated<sup>8</sup> for systems readily available experimentally; that of a face centered cubic (FCC) arrangement of  $\text{SiO}_2$  spheres in an air background, and a similar system of interconnected air spheres in a silicon background. In the horizontal axis we represent the wave vector  $k$  which follows a trajectory on the Brillouin zone (depicted in the inset) linking high symmetry points which define its irreducible part. In the vertical axis, frequency is represented in reduced units of  $a/\lambda$ , where  $a$  is the lattice parameter and  $\lambda$  the wavelength of light in vacuum. The convenient use of such units is justified by the

scalability of the solutions of the problem. The absence of a fundamental length scale in the above equations implies that a change in the length scale of the system is translated into a corresponding change in the energy scale of the eigenvalues so that the product  $\omega a$  remains fixed. In the first situation (figure 2a) we observe how a forbidden frequency interval appears along the  $\Gamma L$  direction for a reduced frequency  $a/\lambda \sim 0.6$ . This corresponds to the case of the pseudogap, that is, a frequency interval for which light may not propagate along certain directions. For this particular symmetry the appearance of a PBG requires a larger refractive index contrast  $\delta n = n_2/n_1$  and a different topology, having the low index material forming the spheres.<sup>9</sup> This is achieved in figure 2b where the refractive index contrast is increased to 3.45. We can see how a complete PBG takes place between the 8<sup>th</sup> and 9<sup>th</sup> band at reduced frequencies 0.85. The appearance of the PBG is favored in the present system due to the fact that an FCC lattice presents the most spherical Brillouin zone of all 3D Bravais lattices. This means that the periodicity is similar along different directions and therefore it is more probable that forbidden intervals overlap for a sufficiently large refractive index contrast.

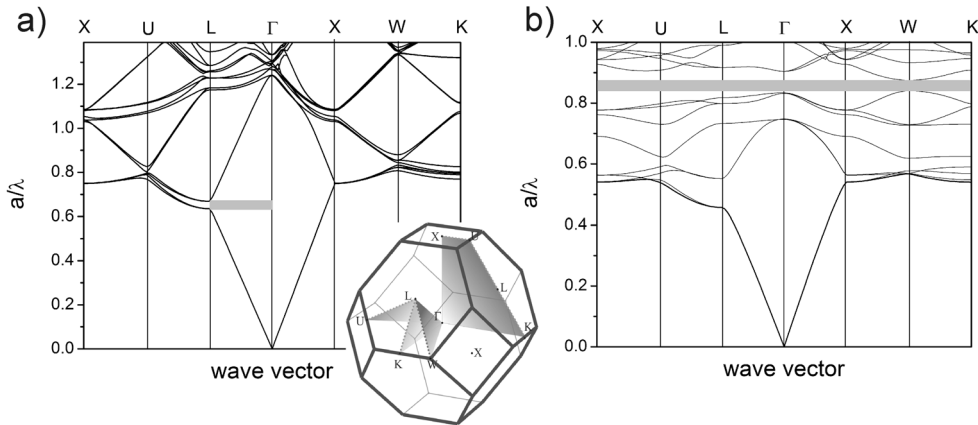


Figure 2: (a) Band structure for an FCC arrangement of dielectric spheres ( $n=1.45$ ) in air, calculated along the high symmetry points defining the irreducible Brillouin zone. Pseudogap along the  $\Gamma L$  direction is denoted as a grey band. (b) Equivalent band structure for an arrangement of air spheres in a dielectric matrix ( $n=3.45$ ). PBG appears as a grey band. Inset shows the Brillouin zone for an FCC lattice.

But photonic band structures do not only provide information on the existence of forbidden intervals, they also allow to study the way light propagates through them. The issue of light propagation in photonic crystals is studied in terms of equi-frequency (or dispersion) surfaces (EFS). An EFS is just the collection of all allowed wave vectors for a certain frequency, and is equivalent to the index ellipsoid in continuous materials. Once the band structure of a crystal is known, the

EFS for a certain frequency may be obtained by searching for all allowed bands for that particular frequency. In a homogeneous and isotropic material EFS are just spheres given by:

$$k = \frac{\omega n}{c} \quad (6)$$

where  $n$  is the refractive index of the material and  $c$  the speed of light in vacuum. If one considers refraction at the interface between two homogeneous and isotropic materials, and carries an EFS analysis, the situation is that sketched in figure 3a. The wave vector inside the second medium is determined by the conservation of the component of the wave vector parallel to the interface, and is parallel to the direction of propagation of energy. This yields the well known expression for Snell's law:

$$n_1 \sin \theta_1 = n_2 \sin \theta_2 \quad (7)$$

where  $n_i$  and  $\theta_i$  are the refractive index and propagation angle inside each medium.

If the second medium is a photonic crystal the situation becomes more complicated. Now the EFS departs from the spherical shape and may take on rather complex forms reflecting the strong anisotropy of the band structure. An example is given in figure 3b. Here only a transversal section of the EFS is considered for the sake of clarity. Propagation is assumed to take place in the plane defined by the normal to the interface and the incident wave vector. A number of differences are evident between both situations. On the one hand the wave vector inside the photonic crystal,  $\mathbf{k}_2$ , determined by the conservation of its component parallel to the interface as in the homogeneous medium case, is not parallel to the direction of propagation of energy ( $\mathbf{v}_g$ ). The latter is parallel to the group velocity in a photonic crystal,<sup>6</sup> which is given by:

$$\mathbf{v}_g = \nabla_{\mathbf{k}} \omega \quad (8)$$

and is therefore normal to the EFS. In this situation Snell's law is not valid anymore and a proper description of light propagation within a photonic crystal can only be done in terms of EFS.

Some of the peculiarities of light propagation in photonic crystals may be understood by looking a bit more carefully into these EFS. We consider a situation in which the frequency or angle of incidence in medium 1 are such that the  $\mathbf{k}$  conservation line falls near a region of high curvature of the EFS in the photonic crystal (point C in figure 3b). In this situation the angle of propagation inside the crystal may undergo extremely large variations for very small changes in the angle of incidence (or frequency) of the incident beam, what is commonly termed super-prism effect.<sup>4</sup> For crystals with a sufficiently large refractive index modulation it can happen that, in the surroundings of forbidden gaps, EFS become spherical again as in the case of the homogeneous dielectric.<sup>5</sup> In this situation Snell's law becomes applicable again and an effective refractive index may be defined for describing light propagation within the crystal. Due to the folding of the bands,

these EFS can be so that their radius decreases with frequency, as opposite to the homogeneous dielectric case. According to (8) this implies that a negative effective refractive index may be defined for certain frequencies. This is different from the case of figure 3b where negative refraction may happen for certain incident angles only and no effective refractive index may be defined.

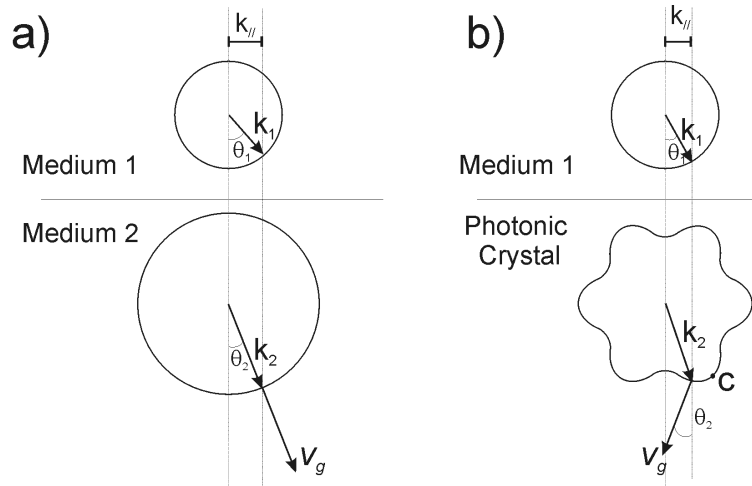


Figure 3: (a) Refraction at the interface between two homogeneous dielectrics. (b) Refraction at the interface between a homogeneous dielectric and a photonic crystal.

A complete description of the propagation of light within a photonic crystal requires not only the knowledge of energy bands (and therefore EFS). Knowing which modes can be excited by an externally incident plane wave is crucial. In certain situations an incident photon of a given frequency may couple to a number of bands, each carrying light in different directions.<sup>10</sup> Furthermore, some bands may not be accessible at all by externally incident plane waves due to symmetry reasons, leading to the false believe that forbidden intervals are present in the band structure.<sup>6</sup>

### 3. Fabrication methods

The theory behind the optical properties of photonic crystals has been extensively studied over the past two decades and a number of fascinating phenomena have been predicted, as already mentioned in section 2. But experimental realization of the necessary structures to test those predictions has been lacking in many cases. The reason for this becomes apparent if one takes into account the fact that the working range for a photonic crystal is dictated by the spatial periodicity of its refractive index. Therefore if one wants to operate in the visible or near infrared side of the electromagnetic spectrum, where most applications are devised for, spatial modulations of the refractive index of a few

hundred nanometers to one micron are needed. This represents a challenge for currently available technology and is inspiring an enormous effort among scientists from many disciplines, from materials science to organic chemistry or engineering.

In principle one would desire a successful technique that is easy to be implemented, has low costs, and yields good quality and reproducible structures involving a reasonable time. In this sense, a number of fabrication methods have been inspired or directly borrowed from other disciplines as is the case of band structure calculations. In this section we summarize some of the most common techniques for the fabrication of 3D photonic crystals in the optical regime. Most of them may be divided into three groups, each carrying its own advantages and drawbacks.

Lithographic methods, which use well developed techniques from the field of microelectronics were the first ones to yield structures predicted to have a PBG in the near infrared part of the spectrum,<sup>11,12</sup> based on the so-called “wood-pile” structure (figure 4a).<sup>13</sup> These methods are rather versatile in terms of the symmetry of the fabricated structure and allow for the introduction of designed defects,<sup>12</sup> mandatory for most applications (see below). Their main drawbacks are the expensive technology and the large time scales involved in the fabrication process. Up to date only crystals with thickness of two unit cells have been reported.

The most popular approach to the fabrication of 3D photonic crystals is that of self-assembly. This method is based on the natural tendency of monodisperse colloidal particles to self assemble into ordered arrays commonly termed artificial opals, after their similarity with precious gems.<sup>14</sup> Its potential as photonic crystals was already acknowledged in the first proposal in 1987,<sup>2</sup> and soon after the first artificial opals were optically characterized in terms of photonic bands.<sup>15</sup> Ever since, a large number of publications related to artificial opals as photonic crystals have appeared. Initially artificial opals were grown by means of sedimentation, letting a colloidal suspension settle under gravity and collecting an ordered sediment after the evaporation of the solvent. Later on, methods such as the vertical deposition one<sup>16</sup> were developed to overcome certain limitations of sedimented samples (see chapter 2). What has made self-assembly so popular is the fact that a number of cheap and well established methods for synthesizing monodisperse colloidal particles made of silica and a number of polymers are available. Furthermore, the growth processes do not require any expensive instrumentation.

Initial samples grown by sedimentation<sup>15,17</sup> had a number of drawbacks concerning the difficulty to control sample thickness and the fact that they were not easy to manipulate. These issues were then improved by the introduction of the vertical deposition method.<sup>16</sup> Other drawbacks are associated with both preparation methods such as the low refractive index contrast, the fixed symmetry of the samples and the amount of uncontrolled disorder present, the latter being detrimental for applications (see below). Extensive research is being developed to solve these three issues. A route to increase the refractive index contrast of artificial opals is to infiltrate their pores with high refractive index materials and then remove the original structure, obtaining the so called “inverse opals” (figure

4b). In this way a number of materials have been successfully infiltrated into these samples,<sup>18</sup> some of them with a sufficiently high refractive index contrast to provide structures predicted to have a PBG.<sup>19-22</sup> Also by doing a controlled infiltration of the pores with different materials, the band structure of these systems may be tailored.<sup>23</sup> In this sense, modifying the unit cell provides a degree of freedom not available by the fixed symmetry of the structure. Disorder remains to date the main problem with these structures.

Holographic lithography has been recently introduced and has become a promising technique.<sup>24</sup> By exposing a photoresist to the interference pattern created by a set of non coplanar laser beams, one may create in it a periodic distribution of crosslinked polymer. The non exposed areas may then be removed, rendering a periodic 3D structure. Structures created in this way are very versatile. The crystal symmetry can be varied with the relative angles between the laser beams, and the shape of the repeating units will depend on the relative amplitudes and polarizations. This fabrication method yields samples of good quality (see figure 4c) in a reduced time (typically a few hours), and in principle does not require expensive equipment besides a laser, polymer and some basic optics. As in the case of artificial opals, samples fabricated with this technique do not possess a PBG due to the low refractive index contrast between the polymer and air. Therefore, further processing is needed, something which up to date is lacking.

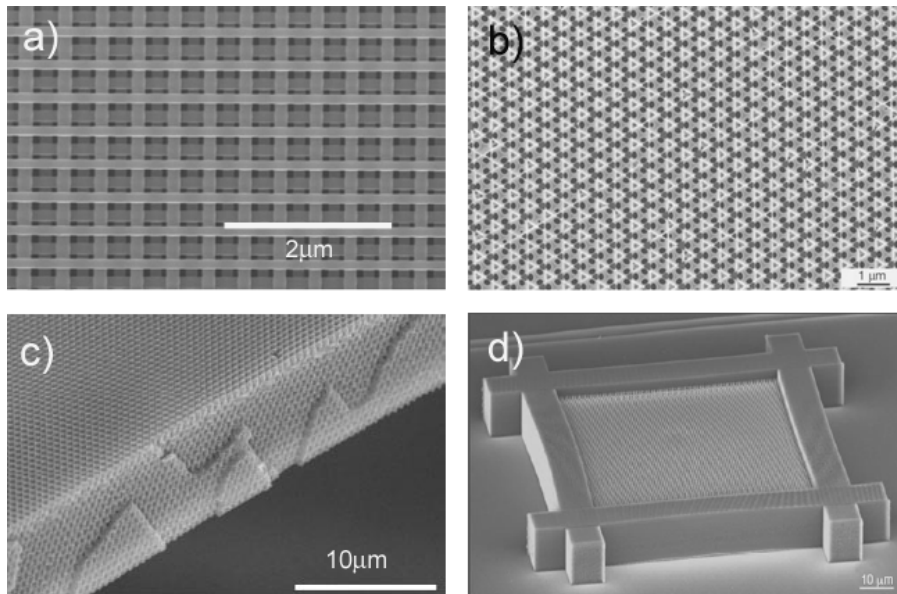


*Figure 4: 3D photonic crystals fabricated by: (a) lithography, (b) self assembly and further processing to obtain an inverse opal, (c) holographic lithography and (d) direct laser writing. Images have been taken from references 12, 21, 24 and 25.*

A number of alternative methods have been developed for the fabrication of 3D photonic crystals in the optical regime, but have not become as popular as the ones above. This has been due to the difficulties of the process, the impossibility of yielding good quality samples or just to the recent development of the technique. Among these we can mention techniques based on focused ion beam milling,<sup>26</sup> nanorobotic manipulation<sup>27</sup> or direct laser writing (see figure 4d).<sup>28</sup>

## 4. Applications

Applications proposed for photonic crystals are numerous and mainly focused on the fabrication of devices that may reproduce the operational principles of the different components of an integrated circuit, applied to photons instead of electrons as information carriers. This is achieved by exploiting the way these structures interact with electromagnetic radiation. Nowadays, most experimental demonstrations have been performed on either 1D or 2D systems. Demonstrations in 3D systems are scarce due to difficulties associated with the fabrication. These applications may in principle be divided into two groups depending on whether a PBG is required.

By appropriately introducing a defect into a perfectly periodic lattice possessing a PBG, one introduces a localized mode into the forbidden interval. One can then tailor the spectral position of that localized state so that it coincides with the emission of internal light sources which can only go into that mode. In this sense losses are absent, and a thresholdless laser may be achieved. This idea, dating back to the very first proposal of a photonic crystal<sup>2</sup> has not been realized in 3D systems mainly due to limitations imposed by the fabrication techniques. Nevertheless, low threshold lasing action has been demonstrated in cavities present in a 2D photonic crystal where vertical confinement was achieved by means of total internal reflection (TIR).<sup>29,30</sup>

Extending the defects into a line, wave-guides may be introduced into a photonic crystal where light confinement is achieved by means of Bragg diffraction rather than TIR. This allows introducing sharp bends of 90° or 120° in spatial dimensions not allowed by conventional TIR guiding. The combination of waveguides and cavities coupled between them permits the design of add-drop filters. Again, experimental demonstrations have only appeared for the case of 2D structures (see figure 5a) where vertical confinement still relies on TIR.<sup>31-34</sup> For the 3D case, theoretical predictions indicate that similar results could be achieved,<sup>35</sup> and systems with wave guiding structures are readily available (figure 5b).<sup>12</sup>

But not all applications rely on the existence of PBG or even forbidden intervals. As previously mentioned, refraction in these structures may present an anomalous behavior not governed by Snell's law. By an adequate design of EFS photonic crystals may be employed as light deflection devices such as (de)multiplexers, spatially separating several signals with similar frequencies traveling along the same direction.<sup>36</sup> Anomalous refraction may also be used to

generate self-collimation phenomena which correct for any divergence of an incoming beam into an optical circuit.<sup>37</sup> An example of the effect of anomalous dispersion on the propagation of similar frequencies with identical direction as they enter a photonic crystal is represented in figure 5c.

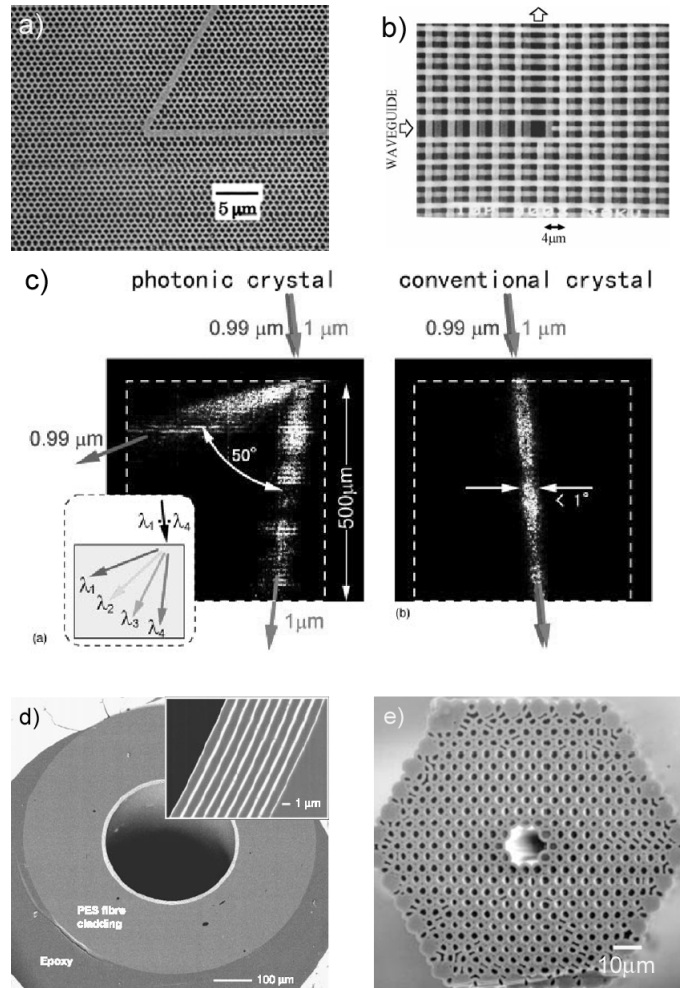


Figure 5: (a) 120° bend in a waveguide inserted in a 2D photonic crystal (ref. 34), (b) 90° bend in a waveguide inserted in a “wood-pile” photonic crystal (ref. 12), (c) Anomalous refraction in a 2D photonic crystal compared to an unstructured material (ref. 36), (d) Optical fiber surrounded by a 1D photonic crystal (ref. 40) and (e) Optical fiber surrounded by a 2D photonic crystal (ref. 42).

Also relying on the propagation of light rather than on forbidden intervals a number of applications have been proposed in which the use of “slow-photon” bands is considered. These bands are typically flat for given wave vectors, and thus have a zero group velocity associated. This implies a long interaction time between

electromagnetic radiation propagating along the crystal and the materials which constitute it. This represents a clear advantage if one (or more) of the constituent materials are optically active. For the case of 2D systems, lasing in the absence of a cavity has been reported and explained in terms of low group velocity bands.<sup>38</sup> In 3D artificial opal based photonic crystals, the low group velocity associated to the edges of pseudogaps has been employed for demonstrating enhanced optical gain.<sup>39</sup>

Up to the present date, the only application based on photonic crystals which has been commercialized is that of optical fibers (see figure 5d and 5e). These fibers may employ Bragg diffraction instead of TIR as a means to confine light into the fiber core. This is done by surrounding it by a 1D<sup>40,41</sup> or 2D<sup>42</sup> photonic crystal presenting forbidden intervals which avoids light propagating through the core to exit it. Since light confinement does not rely in TIR one may, for instance, construct a fiber with an air core which allows the transmission of high intensities without much signal distortion due to non linear effects, and minimizes losses occurring during the coupling of light into the fiber. In the case of fibers with 2D crystals one may also guide light by means of TIR having a material core, achieving endless single-mode performance.<sup>43</sup>

## 5. Defects in Photonic Crystals

The issue of defects in photonic crystals is of great importance. A defect is basically any interruption of an otherwise perfectly periodic structure. The effect of disorder in a photonic crystal is to introduce localized states and generate incoherent scattering. Since the optical properties of a photonic crystal rely on the existence of energy bands, which arises as a consequence of coherent scattering of light, the presence of disorder will certainly affect its optical performance. But contrary to what one may think disorder is not always detrimental for photonic crystals. If defects are introduced in a controlled manner (*wanted* defects), they can act as cavities introducing localized states in the forbidden interval which, if appropriately designed, are the basis for many applications (the cavity for a laser, wave guides, etc.). In this sense, defects have a similar effect as in solid state where one may introduce donor or acceptor localized states inside the gaps.<sup>44</sup>

If disorder takes place in a random manner (*unwanted* defects) the optical properties of a photonic crystal may be completely spoiled. Forbidden intervals are filled with localized states which, for a given amount of disorder may even close an existing PBG turning the density of electromagnetic modes inside to a non-zero value.<sup>45</sup> On the other hand, propagation in allowed bands can not be simply described by means of Bloch modes having a well defined propagation direction due to the presence of incoherent scattering.

The influence of disorder in the optical properties of photonic crystals has been a subject of strong interest in theoretical and experimental research. In order to fully understand how disorder affects the optical performance of a photonic crystal, it is the interplay of order and disorder which must be considered. From a

technological point of view disorder may prevent the use of photonic crystals for any application both in the 2D and 3D cases. But the presence of disorder in photonic crystals also allows for the observation of exciting phenomena. In one of the seminal publications of 1987, it was pointed out that the combination of a controlled amount of disorder with an ordered lattice could lead to the observation of Anderson localization of light.<sup>3</sup>

## 6. This thesis

The work described in the present memory deals with the optical properties of photonic crystals. In particular, the systems under study are opal based photonic crystals grown by means of self assembly methods.

Chapter 2 presents a description of the growth process of thin film artificial opals employed in some of the following chapters. A structural characterization of the samples is presented by means of different techniques.

Chapter 3 deals with the optical properties of thin film opals in the energy region where the pseudogap due to Bragg diffraction by the {111} family of planes parallel to the surface takes place. A study of the effect of the sample size on the optical response is presented. The effect of disorder on the optical properties is also considered. Finally, the structural characterization performed in chapter 2 is used to orient the sample and probe the optical properties of the samples along high symmetry directions.

The high energy spectral region where higher order Bragg diffraction by the {111} planes as well as diffraction by other families of planes takes place is dealt with in chapter 4. The relationship between optical diffraction, energy bands and its effect on the optical properties is discussed.

In chapter 5 phase sensitive measurements on thin film opals are presented. The phase delay introduced by the samples in a broad spectral region (which spans the low and high energy regions) is measured. This allows to further extract an effective refractive index and the group velocity for propagation perpendicular to the sample surface. The results are compared with previous optical characterization presented in chapters 3 and 4.

Chapter 6 presents experimental evidence of the polarization dependence of the optical response of silica artificial opals grown by means of sedimentation.

Finally chapter 7 presents single domain angle-resolved reflectivity measurements on a different type of opal based photonic crystals (namely TiO<sub>2</sub> inverse opals). These measurements allow obtaining information on the optical properties of the samples as well as performing a structural characterization. The effects of disorder on the optical properties of the samples are also discussed.

## 7. References

---

- <sup>1</sup> Yariv, A. and Yeh, P. “*Optical waves in crystals*”, Wiley & Sons, USA (1984).
- <sup>2</sup> Yablonovitch, E. “*Inhibited Spontaneous Emission in Solid-State Physics and Electronics.*” *Physical Review Letters* **58**, 2059-2062 (1987).
- <sup>3</sup> John, S. “*Strong Localization of Photons in Certain Disordered Dielectric Superlattices.*” *Physical Review Letters* **58**, 2486-2489 (1987).
- <sup>4</sup> Kosaka, H., *et al.* “*Superprism phenomena in photonic crystals.*” *Physical Review B* **58**, 10096-10099 (1998).
- <sup>5</sup> Notomi, M. “*Theory of light propagation in strongly modulated photonic crystals: Refractionlike behavior in the vicinity of the photonic band gap.*” *Physical Review B* **62**, 10696-10705 (2000).
- <sup>6</sup> A detailed description of the method may be found in: Sakoda, K. “*Optical properties of photonic crystals*”, Springer-Verlag, Berlin (2001).
- <sup>7</sup> Shung, K. W. K. and Tsai, Y. C. “*Surface Effects and Band Measurements in Photonic Crystals.*” *Physical Review B* **48**, 11265-11269 (1993).
- <sup>8</sup> All band structures presented in this thesis have been calculated with the “*M.I.T. Photonic Bands*” (MPB) freeware (available at <http://ab-initio.mit.edu/mpb/>) unless stated otherwise.
- <sup>9</sup> Sozuer, H. S., Haus, J. W. and Inguva, R. “*Photonic Bands - Convergence Problems with the Plane-Wave Method.*” *Physical Review B* **45**, 13962-13972 (1992).
- <sup>10</sup> Ochiai, T. and Sanchez-Dehesa, J. “*Superprism effect in opal-based photonic crystals.*” *Physical Review B* **64**, art. no.-245113 (2001).
- <sup>11</sup> Lin, S. Y., *et al.* “*A three-dimensional photonic crystal operating at infrared wavelengths.*” *Nature* **394**, 251-253 (1998).
- <sup>12</sup> Noda, S., Tomoda, K., Yamamoto, N. and Chutinan, A. “*Full three-dimensional photonic bandgap crystals at near-infrared wavelengths.*” *Science* **289**, 604-606 (2000).
- <sup>13</sup> Ho, K. M., *et al.* “*Photonic Band-Gaps in 3-Dimensions - New Layer-by-Layer Periodic Structures.*” *Solid State Communications* **89**, 413-416 (1994).
- <sup>14</sup> Jones, J. B., Segnit, E. R. and Sanders, J. V. “*Structure of Opal.*” *Nature* **204**, 990-991 (1964).
- <sup>15</sup> Astratov, V. N., *et al.* “*Optical spectroscopy of opal matrices with CdS embedded in its pores: Quantum confinement and photonic band gap effects.*” *Nuovo Cimento Della Societa Italiana Di Fisica D-Condensed Matter Atomic Molecular and Chemical Physics Fluids Plasmas Biophysics* **17**, 1349-1354 (1995).
- <sup>16</sup> Jiang, P., Bertone, J. F., Hwang, K. S. and Colvin, V. L. “*Single-crystal colloidal multilayers of controlled thickness.*” *Chemistry of Materials* **11**, 2132-2140 (1999).
- <sup>17</sup> Mayoral, R., *et al.* “*3D long-range ordering in an SiO<sub>2</sub> submicrometer-sphere sintered superstructure.*” *Advanced Materials* **9**, 257-260 (1997).

## References

---

- <sup>18</sup> See Lopez, C. “*Materials aspects of photonic crystals.*” *Advanced Materials* **15**, 1679-1704 (2003) and referents therein.
- <sup>19</sup> Blanco, A., *et al.* “*Large-scale synthesis of a silicon photonic crystal with a complete three-dimensional bandgap near 1.5 micrometres.*” *Nature* **405**, 437-440 (2000).
- <sup>20</sup> Miguez, H., *et al.* “*Germanium FCC structure from a colloidal crystal template.*” *Langmuir* **16**, 4405-4408 (2000).
- <sup>21</sup> Vlasov, Y. A., Bo, X. Z., Sturm, J. C. and Norris, D. J. “*On-chip natural assembly of silicon photonic bandgap crystals.*” *Nature* **414**, 289-293 (2001).
- <sup>22</sup> Juarez, B. H., Rubio, S., Sanchez-Dehesa, J. and Lopez, C. “*Antimony trisulfide inverted opals: Growth, characterization, and photonic properties.*” *Advanced Materials* **14**, 1486-1490 (2002).
- <sup>23</sup> Garcia-Santamaria, F., *et al.* “*Photonic band engineering in opals by growth of Si/Ge multilayer shells.*” *Advanced Materials* **15**, 788-790 (2003).
- <sup>24</sup> Campbell, M., *et al.* “*Fabrication of photonic crystals for the visible spectrum by holographic lithography.*” *Nature* **404**, 53-56 (2000).
- <sup>25</sup> Deubel, M., *et al.* “*Direct laser writing of three-dimensional photonic-crystal templates for telecommunications.*” *Nature Materials* **3**, 444-447 (2004).
- <sup>26</sup> Chelnokov, A., *et al.* “*Near-infrared Yablonovite-like photonic crystals by focused-ion-beam etching of macroporous silicon.*” *Applied Physics Letters* **77**, 2943-2945 (2000).
- <sup>27</sup> Garcia-Santamaria, F., *et al.* “*Nanorobotic manipulation of microspheres for on-chip diamond architectures.*” *Advanced Materials* **14**, 1144-1147 (2002).
- <sup>28</sup> Sun, H. B., Matsuo, S. and Misawa, H. “*Three-dimensional photonic crystal structures achieved with two-photon-absorption photopolymerization of resin.*” *Applied Physics Letters* **74**, 786-788 (1999).
- <sup>29</sup> Painter, O., *et al.* “*Two-dimensional photonic band-gap defect mode laser.*” *Science* **284**, 1819-1821 (1999).
- <sup>30</sup> Park, H. G., *et al.* “*Electrically driven single-cell photonic crystal laser.*” *Science* **305**, 1444-1447 (2004).
- <sup>31</sup> Mekis, A., *et al.* “*High transmission through sharp bends in photonic crystal waveguides.*” *Physical Review Letters* **77**, 3787-3790 (1996).
- <sup>32</sup> Lin, S. Y., *et al.* “*Experimental demonstration of guiding and bending of electromagnetic waves in a photonic crystal.*” *Science* **282**, 274-276 (1998).
- <sup>33</sup> Noda, S., Chutinan, A. and Imada, M. “*Trapping and emission of photons by a single defect in a photonic bandgap structure.*” *Nature* **407**, 608-610 (2000).
- <sup>34</sup> Tokushima, M., Kosaka, H., Tomita, A. and Yamada, H. “*Lightwave propagation through a 120 degrees sharply bent single-line-defect photonic crystal waveguide.*” *Applied Physics Letters* **76**, 952-954 (2000).
- <sup>35</sup> Chutinan, A. and Noda, S. “*Highly confined waveguides and waveguide bends in three-dimensional photonic crystal.*” *Applied Physics Letters* **75**, 3739-3741 (1999).

- <sup>36</sup> Kosaka, H., *et al.* “*Photonic crystals for micro lightwave circuits using wavelength-dependent angular beam steering.*” *Applied Physics Letters* **74**, 1370-1372 (1999).
- <sup>37</sup> Kosaka, H., *et al.* “*Self-collimating phenomena in photonic crystals.*” *Applied Physics Letters* **74**, 1212-1214 (1999).
- <sup>38</sup> Meier, M., *et al.* “*Laser action from two-dimensional distributed feedback in photonic crystals.*” *Applied Physics Letters* **74**, 7-9 (1999).
- <sup>39</sup> Vlasov, Y. A., *et al.* “*Enhancement of optical gain of semiconductors embedded in three-dimensional photonic crystals.*” *Applied Physics Letters* **71**, 1616-1618 (1997).
- <sup>40</sup> Temelkuran, B., *et al.* “*Wavelength-scalable hollow optical fibres with large photonic bandgaps for CO<sub>2</sub> laser transmission.*” *Nature* **420**, 650-653 (2002).
- <sup>41</sup> Hart, S. D., *et al.* “*External reflection from omnidirectional dielectric mirror fibers.*” *Science* **296**, 510-513 (2002).
- <sup>42</sup> Russell, P. “*Photonic crystal fibers.*” *Science* **299**, 358-362 (2003).
- <sup>43</sup> Birks, T. A., Knight, J. C. and Russell, P. “*Endlessly single-mode photonic crystal fiber.*” *Optics Letters* **22**, 961-963 (1997).
- <sup>44</sup> Yablonovitch, E., *et al.* “*Donor and Acceptor Modes in Photonic Band-Structure.*” *Physical Review Letters* **67**, 3380-3383 (1991).
- <sup>45</sup> Li, Z. Y. and Zhang, Z. Q. “*Fragility of photonic band gaps in inverse-opal photonic crystals.*” *Physical Review B* **62**, 1516-1519 (2000).

## CHAPTER 2

---

# Fabrication and structural characterization of artificial opals

### 1. Introduction

As mentioned in the first chapter, self-assembly techniques constitute the most popular approach to the fabrication of 3D photonic crystals. Based on the natural tendency of monodisperse colloidal particles to organize into ordered arrays, these methods represent the best option due to ease of fabrication and economy of the process. Besides these advantages, self-assembly provides us with artificial opals. In the most favorable situation an artificial opal will consist of a face centered cubic (FCC) arrangement of spherical scatters which, for the appropriate refractive index contrast can develop a complete photonic band gap (PBG).<sup>1</sup> Even if a PBG is absent, these structures are interesting on its own as they represent a playground to explore the optical properties of photonic crystals. Artificial opals and related structures obtained by self assembly have been used to explore enhancement of optical gain,<sup>2</sup> second<sup>3</sup> and third<sup>4</sup> harmonic generation, or Faraday rotation,<sup>5</sup> and have been further predicted to present anomalous refraction.<sup>6</sup>

Initially, artificial opals were grown by sedimentation of monodisperse colloidal particles in solution.<sup>7,8</sup> Samples grown in this way usually presented an uncontrollable thickness and a large variety of defects (point defects, dislocations, mosaic spread, stacking faults,...). In addition, these samples were not easy to handle due to its fragility (unless further processing<sup>9,10</sup> was done to enhance their mechanical stability) and took long periods to grow due to the slow sedimentation rate needed to obtain a good crystalline order.

Over the past few years a new method known as the vertical deposition method<sup>11</sup> has emerged as an alternative to sedimentation. Besides the improvement in fabrication time (a few days are needed compared to sedimentation, which required up to several months), samples grown by vertical deposition present

smaller defect concentration, controllable thickness and are easier to handle since they are grown on solid substrates.

In this chapter, after presenting a qualitative description of the process, experimental conditions are given to obtain samples with high quality in terms of its optical response. Afterwards, a structural characterization of the samples is carried out by means of optical and electronic microscopy as well as optical diffraction. This will allow us to select the best regions for carrying out an optical characterization as will be shown in future chapters.

## 2. Vertical deposition method

Since its introduction in 1999 by Jiang *et al.*,<sup>11</sup> the vertical deposition method has become the most spread within self-assembly techniques to fabricate opal-based 3D photonic crystals. The method is based on previous work by Nagayama and co-workers<sup>12-14</sup> in which the formation of colloidal monolayers was studied. Both techniques are based on the convective self-assembly of colloids on a substrate by the action of a moving meniscus.

Although extensively used for over five years now, the mechanism of crystal formation is not well understood to the present date.<sup>15</sup> Only a qualitative explanation has been given, and a number of parameters which influence crystal growth (most of them borrowed from the monolayer problem<sup>12</sup>) have been determined.

In a typical procedure, a flat substrate is introduced in a vial containing a colloidal suspension which wets the substrate, a meniscus forming at the line where the substrate, air and liquid meet (figure 1). Crystal growth begins at the point of the meniscus where its thickness is below the diameter of the sphere.<sup>12</sup> Menisci are formed between the spheres, which are pulled towards the substrate and attracted to each other due to capillary forces which tend to order them in a close packed monolayer. Solvent flow towards the meniscus region (which compensates for evaporation) drags spheres from the suspension and these are incorporated to the ordered monolayer. Under the appropriate conditions involving colloid concentration and evaporation rate,<sup>12</sup> more than one layer may begin to grow at the meniscus. These new layers grow in a peculiar manner, where the boundary between an “n” layer region and an “n+1” one presents square packing instead of the hexagonal one. This configuration has been attributed to an optimal filling of the meniscus region.<sup>16</sup>

But the exact transition from the 2D ordering to the formation of a 3D FCC structure is not understood. It is assumed that colloidal particles are dragged to the ordered array by means of solvent flow and are incorporated to it. Therefore the optimal conditions for the growth of a sample with good crystalline order should include an evaporation rate which allows for the ordering of particles at the meniscus, as well as the presence of a reservoir of particles in the solution to be

incorporated to the ordering region. Initial experiments carried out by Jiang *et al.*<sup>11</sup> consisted in a solution of silica spheres in ethanol, and were limited by the sphere size. For spheres with a diameter above ca. 400 nm, sedimentation decreased the sphere concentration and yielded poor quality samples. This certainly represented a problem, since particles with diameters above 600 nm are required in order to fabricate silicon inverse opals with a PBG around 1.5  $\mu\text{m}$ . This issue was overcome in 2001 by Vlasov and co-workers<sup>17</sup> by introducing a temperature gradient in the vial containing the solution, so that convective flow would prevent particle sedimentation. By doing this, particles with a diameter up to 1  $\mu\text{m}$  were ordered in samples having thickness as large as 20 layers on crystalline silicon substrates.

Later on, samples were also grown by vertical deposition using an aqueous solution of polymer colloids<sup>18</sup>, as in the original works by Nagayama, and solving the sedimentation issue by just placing the vial containing the solution in an oven at a fixed temperature. The main advantage of working with polymer colloids in water is that the effect of sedimentation may be compensated using a much lower temperature than with silica, due to the smaller density difference. This permits a slower evaporation rate, and therefore a better crystalline quality of the sample obtained. Although there is a general consensus on the critical role played by the temperature in the growth of such samples, several publications<sup>18-23</sup> mention optimum temperatures in a much too wide a range (50°C to 95°C) for apparently very similar conditions.

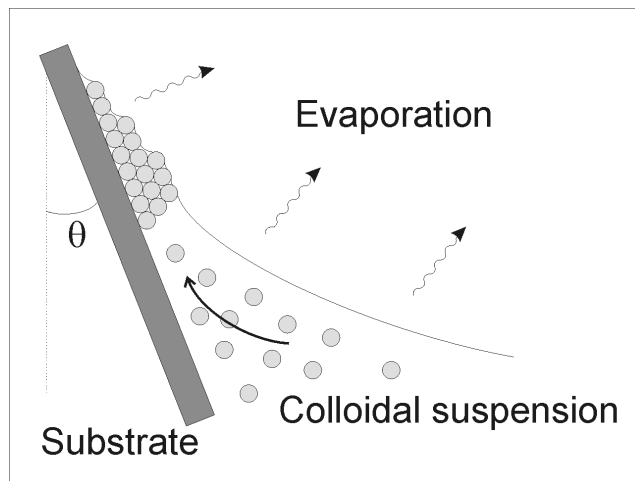


*Figure 1: Schematic of the vertical deposition method. A substrate (dark grey) is placed in a colloidal suspension which wets it. The substrate is inclined at an angle  $\theta$ . Ordering of the spheres takes place at the meniscus.*

Other parameters which influence the growth of the samples are the diameter and concentration of the colloids, which are known to determine the thickness of the samples. In general, higher concentrations and smaller colloids yield samples

with a larger number of layers. Further, colloid size and temperature are not independent parameters. Larger colloids will need higher temperatures to prevent sedimentation.

The aim of the present work was to find the conditions which yield the highest optical quality samples. That is, those samples whose optical response was less affected by disorder (see chapter 3). In order to do so we have employed the vertical deposition method using polystyrene spheres for different temperatures (35-65°C) and concentrations (0.05-0.4%vol.). Spheres grown by means of surfactant-free emulsion polymerization were prepared by E. Castillo-Martínez and Dr. E. Palacios-Lidón. Its diameter was determined to be 705 and 505 nm by comparing the Bragg peak from normal incidence reflectance spectra (for samples with sufficient number of layers) with calculated bands assuming a refractive index for polystyrene equal to the bulk value (see chapter 3). These values were in agreement with 712 and 511 nm (with 3% polydispersity) obtained from transmission electron microscopy (TEM). Spheres purchased from Duke scientific were estimated to have a diameter of 1090 nm from reflectivity measurements, which coincided with the value of 1100 nm provided by the suppliers (1% polydispersity). In the sphere diameter range 505-705 nm we found similar results, in terms of sample thickness and optical quality, independent of sphere size. For spheres with a diameter of 1090 nm, these conditions varied.

The substrates employed were clean hydrophilic glass microscope slides or pieces of a crystalline silicon wafer. Glass microscope slides were placed in HCl 33% overnight and then rinsed in de-ionized water and dried in a nitrogen flow. Silicon wafers were cleaned for 10 minutes in a HF solution (1%) and then placed in a H<sub>2</sub>SO<sub>4</sub>/H<sub>2</sub>O<sub>2</sub> solution (3:2 vol.) for 30 minutes. In a typical procedure the substrate was placed inside a 20 ml vial containing 8 ml of an aqueous suspension of polystyrene spheres. The vial was placed inside an oven where the temperature was kept constant with a precision of 1°C. The substrates were left inside the oven over a period of time long enough as to allow for sample growth over a distance of 1cm along the vertical direction (the lateral dimension was fixed by the substrate width; 1.3cm). Therefore samples grown for lower temperatures needed longer times.

It was found that the temperature that yielded samples showing the best optical properties was 45°C for spheres with a diameter of 505-705 nm and 50°C for the 1090 nm ones. The time needed to grow a sample with 1cm length was 60 hours in the first case and 50 in the second. For lower temperatures, samples grown for the same concentration presented a smaller number of layers as well as poorer quality. This is probably due to the fact that for lower temperatures, sedimentation competes with convective fluxes and the reservoir of particles in the meniscus decreases with time. On the contrary, for higher temperatures, thicker samples are obtained at the price of lowering the optical quality.

In general, the thickness of the sample for a fixed temperature could be controlled with the colloid concentration. Nevertheless variations of up to 30% in

the number of layers present in the central part of the sample (the most homogeneous in terms of thickness) could be found.

Finally we mention that some publications have pointed out the importance of other parameters such as relative humidity (RH) of the sample environment (in controlling the evaporation rate for a fixed temperature),<sup>23</sup> substrate inclination and meniscus shape.<sup>24</sup> For the samples grown in this research there was no control on RH, although it was found that covering the vial with a beaker (volume of 1 litre) the sample quality was improved, probably due to a reduction in evaporation rate. The best results were for substrates inclined 20°-30° with respect to the vertical. We now proceed to present structural characterization of the samples grown under the above mentioned conditions.

### 3. Structural characterization

#### a. Optical microscopy:

Optical microscopy allows for a preliminary study of the samples which yields information on the way growth takes place. Figure 2 shows typical photographs taken in reflectance with a 10x microscope objective, from samples made out of 505 nm spheres grown under the above mentioned optimal conditions on glass substrates.

In figure 2b we can see the initial stages of sample growth which takes place at the top of the sample. The arrow indicates the growth direction which is parallel to the meniscus moving direction. It can be appreciated how the sample grows forming terraces of increasing number of layers in its first stages. The color of the terraces varies from brown (one layer) to pink (eight layers). It is interesting to note how at the boundary between two terraces with different number of layers, a shiny green region appears. The reason for this color will be discussed below. Although these colors are particular for samples with this sphere diameter, a similar behavior was observed for larger colloids.

In the central region of the sample (~1.5mm away from the edges and the top) we observe a more homogeneous distribution of the terraces. Figure 2c shows a typical region where the number of layers changes from 8 (top) to 9 (bottom). The green shiny regions at the terrace boundaries mentioned above seem to disappear as the number of layers increases. In the central region only a few spots are found. Regions with a constant thickness usually have dimensions of 0.5-3mm in the growth direction and up to 1cm in the direction perpendicular to it. In these regions cracks are apparent as dark lines parallel to the growth direction. These cracks are common to this type of samples, and are believed to be originated during the drying process.<sup>11</sup>

As we move towards the lateral edges of the sample the morphology changes quite abruptly as shown in figure 2d. We can see how at the edge the sample presents the same terrace-like shape as at the top. As we move towards the center,

the boundaries between terraces are curved, indicating the transition from the vertical behavior at the edge, to the horizontal one at the center. Further, the above mentioned cracks curve away from the vertical towards the edge, as indicated by the arrow. This is probably due to a deformation of the meniscus at the substrate edge, something which may be observed with the naked eye as the substrate is placed in the vial. The way this deformation influences crystalline order will be discussed below. As observed at the top, shiny green regions are apparent at the boundaries between the terraces.

If the substrate presents regions that are not hydrophilic, the growth at the top of the sample does not occur along a line parallel to the meniscus, but presents an abrupt profile. For such samples, shiny green regions up to 1mm in size may be found (figure 3).

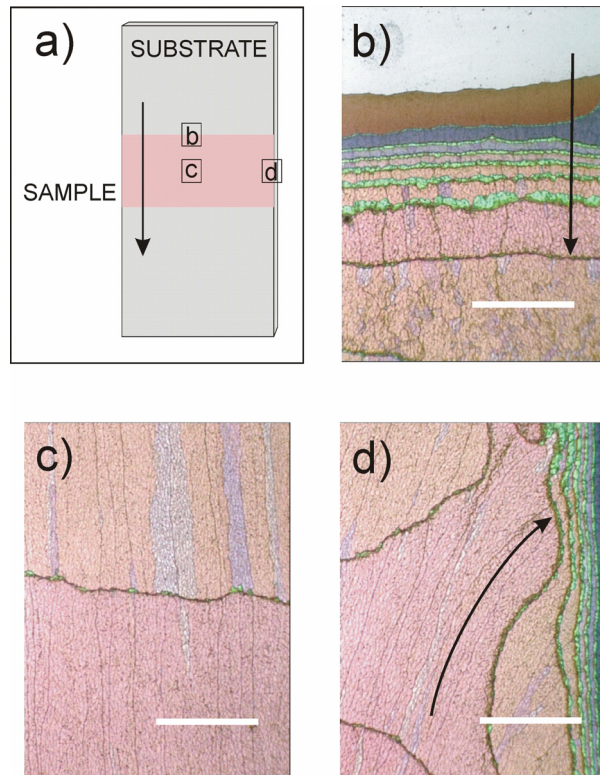


*Figure 2: (a) Schematic representation of substrate (grey) and sample (pink). The vertical arrow indicates the growth direction. Rectangles indicate regions from where the following pictures were collected in samples made out of 505nm spheres: (b) Top of the sample showing initial stages of growth. Arrow indicates growth direction. (c) Central region. (d) Edge of sample, close to substrate edge. The curved arrow indicates the direction of cracks. Scale bar is 375µm in all three cases.*

Samples grown on silicon substrates presented similar characteristics as those grown on glass. Only certain regions appeared to present no deposit, probably due to the fact that were not hydrophilic.

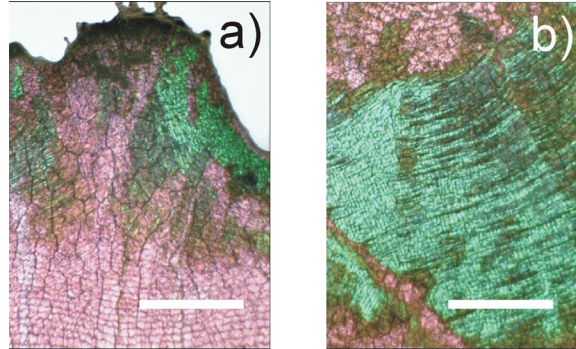


Figure 3: (a) Detail of the top of a sample grown on a poorly hydrophilic substrate. (b) Shiny green region close to the top of the sample. Scale bars are 375  $\mu\text{m}$  in both cases.

#### **b. Scanning electron microscopy:**

Although optical microscopy gives some valuable information on the morphology and growth of the samples, a technique with a larger spatial resolution is needed in order to investigate crystalline order at a more local level. In this sense Scanning Electron Microscopy (SEM) has been the ideal tool for a more in-depth structural characterization of photonic crystals.

SEM micrographs were obtained with a FEI Quanta 200 model. Before observation samples were coated with a thin gold film in order to avoid charging effects. Figures 4 and 5 show SEM micrographs corresponding to samples grown under the optimal conditions mentioned before. All the images shown correspond to samples having 505 nm diameter spheres. For other sphere sizes similar features were observed.

Figure 4a shows a detail of the sample surface. The image was taken from the central part of the sample. Hexagonal order characteristic of the  $\{111\}$  planes in an FCC structure or the  $\{0001\}$  ones in a hexagonal close packed (HCP) is evident. The growth direction is along the horizontal axis of the photograph. A number of defects may be appreciated in this image such as dislocations, vacancies and local distortions of the lattice originated by polydispersity. Images taken at a lower magnification (figure 4b) show the cracks already observed with optical microscopy. A tendency is observed for cracks to appear along rows of spheres, defining hexagonal patterns. These cracks appear every 50-80  $\mu\text{m}$ . A closer look into the regions at both sides of a crack shows that the crystalline orientation is the same across the crack. This has led to the belief that these cracks appear in the process of drying of the crystal, once the ordering has taken place.<sup>11</sup>

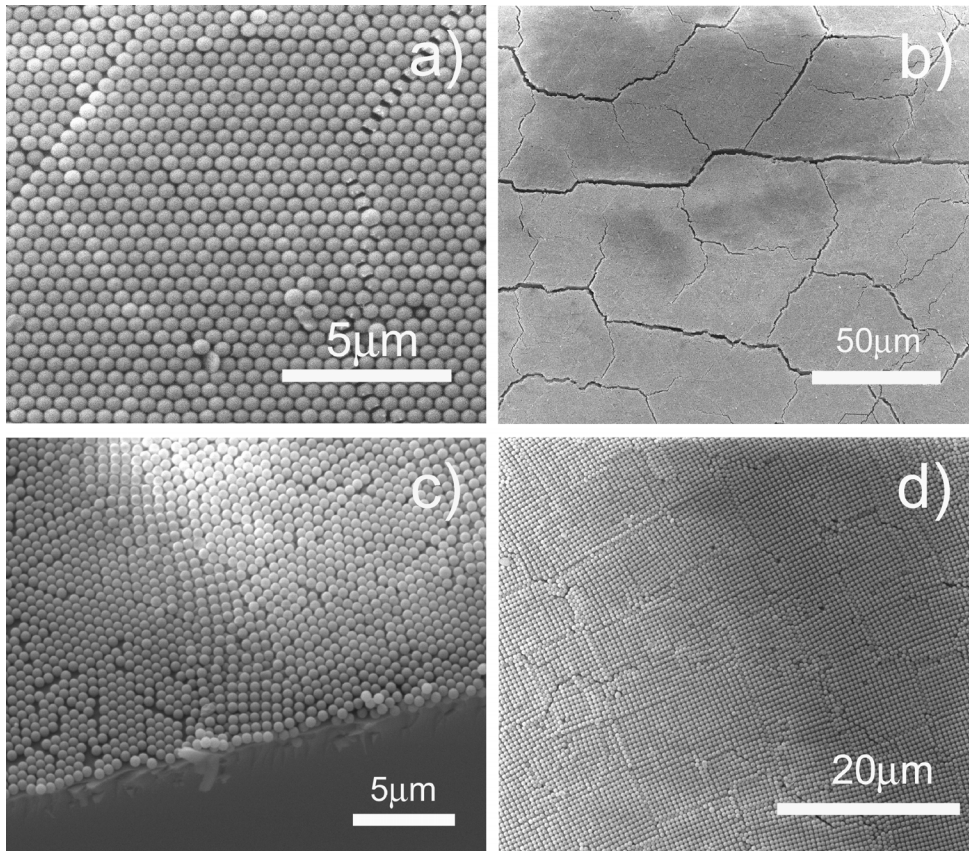


Figure 4: SEM images taken from different samples with sphere diameter 505 nm. Details are given in the text.

Inspection of the first stages of the crystal growth reveals the terraces already observed in optical microscopy. Figure 4c shows an image of this region where the number of layers increases from left to right. As the number of layers increases, an alternation in the order of the stacked layers can be appreciated, between hexagonal and square packing, as mentioned earlier. The origin of the shiny green colors observed at the terrace boundaries is originated by these square layers. As a matter of fact, if we inspect the large shiny green regions observed in poorly hydrophilic substrates, we find rather large areas showing square order parallel to the surface (figure 4d). This order seems to remain for layers below the surface one (figure 5a). Square order over large regions has been previously observed<sup>17,20</sup> and associated with  $\{200\}$  families of planes from FCC structures. The order present in the samples can not only be observed at the surface but also through the volume of the crystal in cleft samples. Figure 5b shows the edge of a sample presenting square order, a signature of FCC ordering.<sup>25</sup> These planes are not to be mistaken with the square ones present at the surface (figure 4d), as these are  $\{200\}$  planes not parallel to the surface. Other cleft regions (figure 5c) allow for the observation

of hexagonal facets other than the  $\{111\}$ . In these facets, dislocations present at the surface are now seen to run the entire crystal.

Figure 5d shows the bottom of the sample, where the growth process stops once the sample is withdrawn from the vial. It can be seen how the crystal ends in an abrupt manner at an angle nearly perpendicular to the substrate. This indicates that, as opposite to sedimented opals where growth is assumed to happen parallel to the surface, here the direction of sample growth is parallel to that of meniscus advance. Covering the sample we find a layer of disordered spheres which probably forms when the meniscus sweeps over the crystal as it is withdrawn from the suspension.

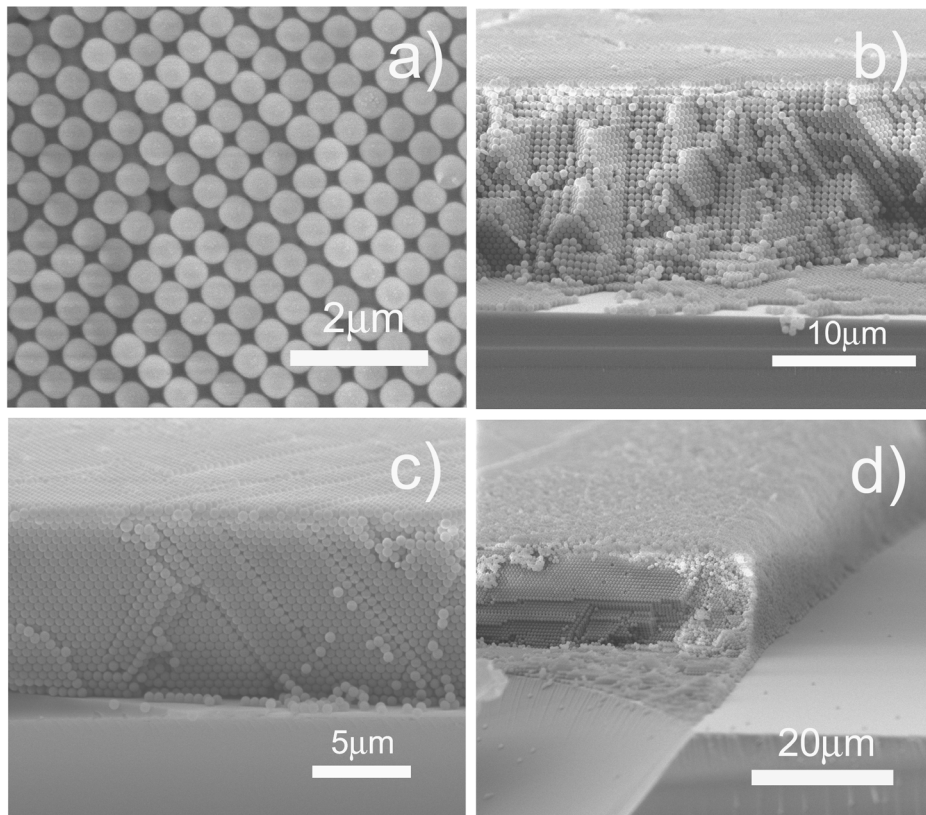


Figure 5: (a)-(d) SEM images taken from different samples with sphere diameter 505 nm. Details are given in the text.

### c. Optical diffraction:

From what we have seen so far, the combination of optical and electron microscopy gives a good idea on the way samples grow, the presence of disorder both at a microscopic and macroscopic level, etc. Another technique which may

offer useful information, and which can be considered as complementary to the former two is optical diffraction.

Diffraction patterns obtained with visible light have been observed in colloidal photonic crystals presenting a very low refractive index contrast and used to obtain information on the order present in the volume of the crystal.<sup>26</sup> They were modeled in a single scattering approximation as a superposition of diffraction from 2D arrays of spheres which are stacked in a certain order. Depending on the geometry of the 2D array, as well as the stacking sequence the diffraction pattern will vary. For close packed crystals with hexagonal planes parallel to its surface, hexagonal or triangular patterns are expected depending on the stacking sequence. For pure FCC crystals (ABCABC or CBACBA sequences<sup>27</sup>) a triangular pattern (C3 symmetry) is expected. Hexagonal diffraction patterns (C6 symmetry) are obtained for HCP (ABAB sequence), random close packed (RCP) or twinned FCC (that is, presenting both sequences ABCABC and CBACBA) structures.

These patterns have also been observed in a number of publications concerning opal-based photonic crystals, all of them in the form of thin film opals grown by the vertical deposition method. Vlasov et al.<sup>17</sup> observed a hexagonal diffraction pattern in reflection and associated it with Bragg diffraction by the {220} families of planes. Later, Goldenberg and co-workers<sup>21,28</sup> observed hexagonal and triangular diffraction patterns from thin film opals both in reflection and transmission and interpreted them as diffraction from successive 2D hexagonal arrays, as in previous research with colloidal crystals. In reference 22 hexagonal diffraction patterns projected on the sample itself were associated with diffraction from the first layer of spheres. In the last two cases, the pattern was modeled with the grating equation  $m\lambda = d(\sin\varphi + \sin\theta)n$ . Here  $\lambda$  is the wavelength of light in vacuum,  $m$  is the diffraction order,  $d$  the grating period ( $0.866 \cdot d_{sph}$  for a hexagonal 2D array of spheres with diameter  $d_{sph}$ ),  $\varphi$  is the angle between the incident beam and the sample normal,  $\theta$  is the angle between the diffracted beam and the sample normal and  $n$  the refractive index of the surrounding medium (air in the first case and glass in the second).

In order to extract structural information about our samples we have studied the transmitted diffraction pattern of laser beams. Figure 6 shows some photographs, for a sample consisting of spheres of 705 nm diameter and the 476 nm line from an argon laser, collected on a screen placed 5 cm away from the sample and parallel to it. Similar patterns were also observed in reflection.

Figures 6b-6d show the diffraction pattern obtained for samples having 1, 2 and 3 layers. The diffraction pattern evolves from the characteristic hexagonal one corresponding to a close-packed monolayer to a triangular pattern indicating FCC ordering if we assume the single scattering model (SSM) predictions. As we displace the beam along the sample the orientation of the pattern remains unchanged.

If the sample thickness is increased to 6 layers, the diffraction pattern is of the hexagonal type (figure 6e). If we now lower the refractive index contrast of the sample by infiltrating it with ethanol, the pattern recovers the C3 symmetry. Further, different regions may be found where the pattern changes from three spots

to the complementary ones (figures 6f and 6g). According to the SSM this would indicate the existence of FCC regions with reversed stacking sequences.

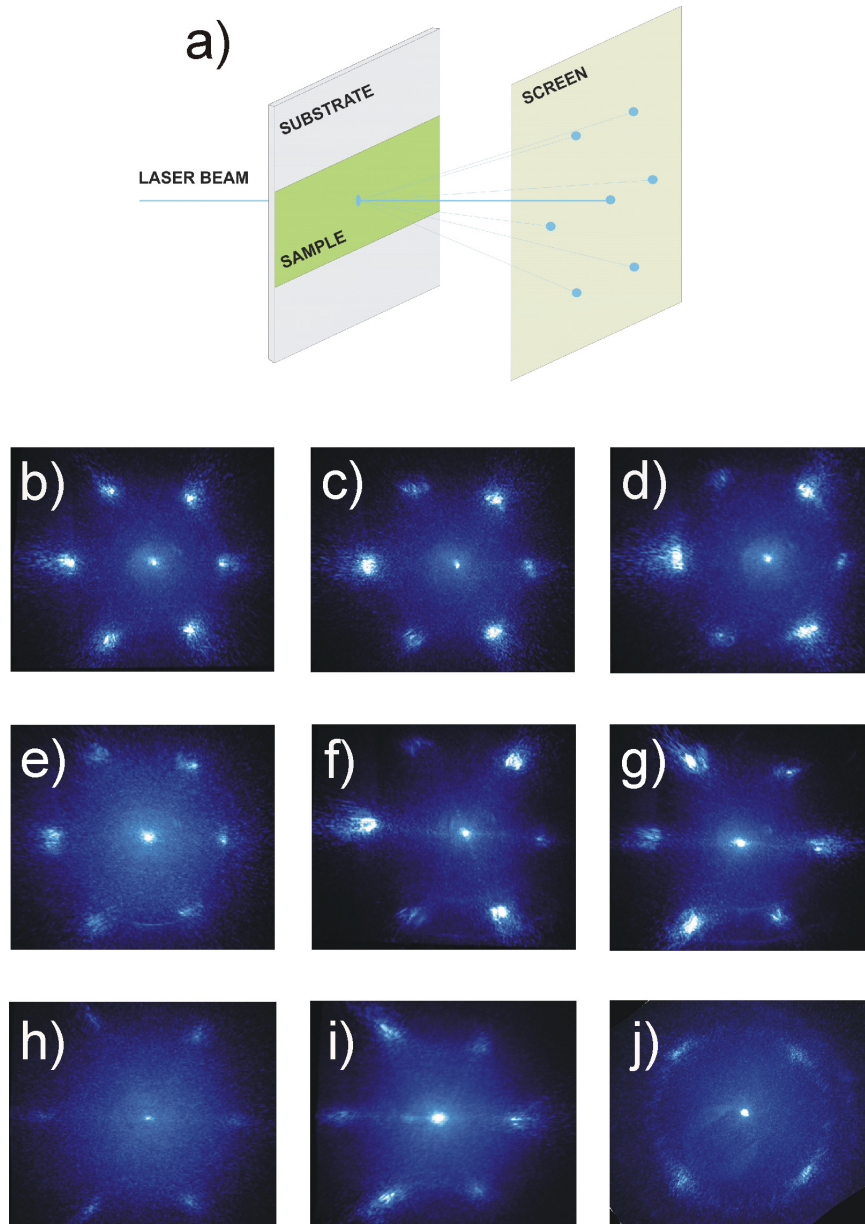
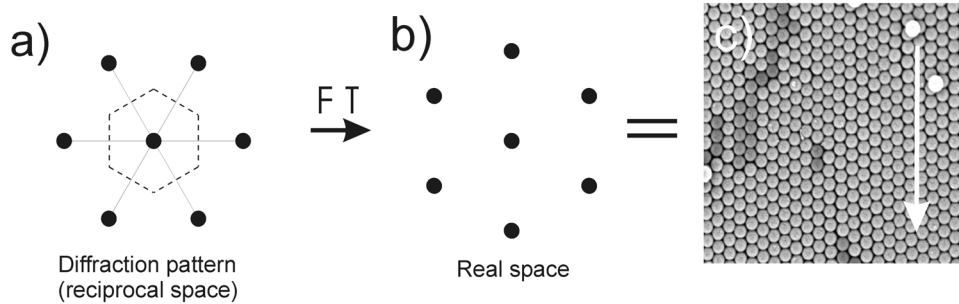


Figure 6: (a) Diagram of diffraction set-up. (b-j) Diffraction patterns collected from different samples. Details on the photographs are given in the text.

Hexagonal patterns for samples having 20 layers present spots which are narrower along the circumference which joins them (figure 6h). Lowering the refractive index contrast we recover the C3 symmetry, but now all spots remain visible (figure 6i). Broadening of the spots along the circumference is a signature of randomness in the plane. This coincides with the SEM photographs of regions having fewer layers (i.e. figure 4c), where a less dense packing was observed and an in-plane mosaic spread is evident. Finally, square patterns may be observed (figure 6j) in the large green regions which appear for poorly hydrophilic substrates. This also agrees with SEM observations (figure 4d). Here, besides the broadening, diffraction spots are superimposed on a circular halo which resembles Debye-Scherrer rings of fluid-like structures, indicating worse crystalline quality.

If we follow the arguments from single scattering models, the fact that with the number of layers the C3 symmetry of the pattern is lost could indicate that FCC ordering disappears for thick samples. Although it is not likely that single scattering arguments will hold for systems having such a high refractive index contrast as ours, except for the case of few layers and of contrast lowering by ethanol infiltration.

Although extracting information about the bulk order is not immediate due to the doubtful validity of single scattering arguments in our systems, the observation of square facets in SEM inspection is a clear signature of FCC ordering. Nevertheless information regarding sample growth and orientation may be extracted from the above mentioned patterns. Since the diffraction pattern can be considered as the Fourier transform of the periodic array present in the surface, diffraction spots may be assigned to reciprocal lattice points. Therefore by rotating the diffraction pattern  $30^\circ$  we obtain the arrangement of spheres in the direct space, as shown in figure 7. It is seen then that the way spheres are ordered into a periodic array by the moving meniscus, is in the form of rows parallel to the direction in which the meniscus moves, indicated in the SEM picture of figure 7c by an arrow. This confirms observations of the samples under SEM (figure 4a). Here we must note that this observation contradicts the claim in reference<sup>29</sup> that spheres arrange in rows parallel to the meniscus for samples grown in similar conditions, and agrees with observations of 2D hexagonal monolayer formation.<sup>12</sup> The fact that the pattern remains unchanged as we displace the beam along the sample further confirms SEM observations of preserved order at both sides of cracks. If the beam reaches the lateral edges of the sample we observe that the hexagonal/triangular pattern rotates towards the edge. This coincides with the curving of the cracks observed with optical microscopy. As spheres tend to order in rows perpendicular to the meniscus, its deformation at the substrate edges brings about a deviation of crystal orientation in the plane parallel to the surface. Besides giving valuable information on the morphology and growth of the samples, these diffraction patterns may also be used for sample orientation when angle resolved measurements are carried out, as will be discussed in chapter 3.



*Figure 7: (a) Diagram of the diffraction pattern projected on the screen. Dashed hexagon represents the Brillouin zone of the surface 2D lattice. (b) Fourier transform of the pattern representing the real space distribution of the spheres. (c) SEM photograph of the sample oriented along its vertical axis (parallel to the growth direction, indicated by an arrow).*

Finally we have studied the angular evolution of the diffraction patterns on the screen obtained with laser beams and fitted them to the grating equation for samples with different sphere diameters.<sup>a</sup> The values obtained were  $521 \pm 4$  nm,  $726 \pm 3$  nm and  $1130 \pm 2$  nm, slightly above the ones mentioned previously but within the observed dispersion. The results were reproducible as the sample was rotated  $60^\circ$  around an axis parallel to its normal, evidencing C6 symmetry.

#### 4. Conclusions and future work

In this chapter, after giving a brief summary of previous results on opal based photonic crystal fabrication by the vertical deposition method, the experimental conditions for the growth of samples with high optical quality are given. These samples consist of polystyrene spheres deposited on glass microscope slides or silicon wafers.

Afterwards, a structural characterization of the samples grown has been presented. By means of optical microscopy information is gathered on the way samples grow. The initial stages of sample growth take place forming terraces of increasing number of layers at the sample top and lateral edges which yields a homogeneous region in the central part. Cracks appear perpendicular to the meniscus.

SEM inspection allows obtaining structural information at a more local level. Besides detecting several types of defects (dislocations, cracks, point defects, etc.), evidence of FCC ordering with different orientations (namely  $\{111\}$  and  $\{200\}$

---

<sup>a</sup> Results for the 1090 spheres were obtained by Dr. Matteo Galli at Dipartimento di Fisica “A. Volta”, Università di Pavia (Italy).

planes parallel to the surface) is found. Further, observations regarding the growth process are made which complement those from optical microscopy.

Finally optical diffraction experiments are carried out. Results may be associated with predictions from colloidal crystal research for thin samples and low refractive index contrast. For thicker samples, although an interpretation is not immediate, optical diffraction provides a means of orienting the samples and confirms previous observations by SEM concerning sample growth.

## 5. References

- <sup>1</sup> Sozuer, H. S., Haus, J. W. and Inguva, R. “*Photonic Bands - Convergence Problems with the Plane-Wave Method.*” *Physical Review B* **45**, 13962-13972 (1992).
- <sup>2</sup> Vlasov, Y. A., *et al.* “*Enhancement of optical gain of semiconductors embedded in three-dimensional photonic crystals.*” *Applied Physics Letters* **71**, 1616-1618 (1997).
- <sup>3</sup> Martorell, J., Vilaseca, R. and Corbalan, R. “*Second harmonic generation in a photonic crystal.*” *Applied Physics Letters* **70**, 702-704 (1997).
- <sup>4</sup> Markowicz, P. P., *et al.* “*Dramatic enhancement of third-harmonic generation in three-dimensional photonic crystals.*” *Physical Review Letters* **92** (2004).
- <sup>5</sup> Koerdt, C., Rikken, G. and Petrov, E. P. “*Faraday effect of photonic crystals.*” *Applied Physics Letters* **82**, 1538-1540 (2003).
- <sup>6</sup> Ochiai, T. and Sanchez-Dehesa, J. “*Superprism effect in opal-based photonic crystals.*” *Physical Review B* **64**, art. no.-245113 (2001).
- <sup>7</sup> Astratov, V. N., *et al.* “*Optical spectroscopy of opal matrices with CdS embedded in its pores: Quantum confinement and photonic band gap effects.*” *Nuovo Cimento Della Societa Italiana Di Fisica D-Condensed Matter Atomic Molecular and Chemical Physics Fluids Plasmas Biophysics* **17**, 1349-1354 (1995).
- <sup>8</sup> Mayoral, R., *et al.* “*3D long-range ordering in an SiO<sub>2</sub> submicrometer-sphere sintered superstructure.*” *Advanced Materials* **9**, 257-260 (1997).
- <sup>9</sup> Astratov, V. N., *et al.* “*Photonic band gaps in 3D ordered fcc silica matrices.*” *Physics Letters A* **222**, 349-353 (1996).
- <sup>10</sup> Miguez, H., *et al.* “*Control of the photonic crystal properties of fcc-packed submicrometer SiO<sub>2</sub> spheres by sintering.*” *Advanced Materials* **10**, 480-483 (1998).
- <sup>11</sup> Jiang, P., Bertone, J. F., Hwang, K. S. and Colvin, V. L. “*Single-crystal colloidal multilayers of controlled thickness.*” *Chemistry of Materials* **11**, 2132-2140 (1999).
- <sup>12</sup> Denkov, N. D., *et al.* “*Mechanism of Formation of 2-Dimensional Crystals from Latex-Particles on Substrates.*” *Langmuir* **8**, 3183-3190 (1992).
- <sup>13</sup> Denkov, N. D., *et al.* “*2-Dimensional Crystallization.*” *Nature* **361**, 26-26 (1993).
- <sup>14</sup> Dimitrov, A. S. and Nagayama, K. “*Continuous convective assembling of fine particles into two-dimensional arrays on solid surfaces.*” *Langmuir* **12**, 1303-1311 (1996).
- <sup>15</sup> Norris, D. J., *et al.* “*Opaline photonic crystals: How does self-assembly work?*” *Advanced Materials* **16**, 1393-1399 (2004).
- <sup>16</sup> Pieranski, P., Strzelecki, L. and Pansu, B. “*Thin Colloidal Crystals.*” *Physical Review Letters* **50**, 900-903 (1983).
- <sup>17</sup> Vlasov, Y. A., Bo, X. Z., Sturm, J. C. and Norris, D. J. “*On-chip natural assembly of silicon photonic bandgap crystals.*” *Nature* **414**, 289-293 (2001).
- <sup>18</sup> Meng, Q. B., Gu, Z. Z., Sato, O. and Fujishima, A. “*Fabrication of highly ordered porous structures.*” *Applied Physics Letters* **77**, 4313-4315 (2000).

- <sup>19</sup> Ye, Y. H., LeBlanc, F., Hache, A. and Truong, V. V. "Self-assembling three-dimensional colloidal photonic crystal structure with high crystalline quality." *Applied Physics Letters* **78**, 52-54 (2001).
- <sup>20</sup> Meng, Q. B., *et al.* "Assembly of highly ordered three-dimensional porous structure with nanocrystalline TiO<sub>2</sub> semiconductors." *Chemistry of Materials* **14**, 83-88 (2002).
- <sup>21</sup> Goldenberg, L. M., *et al.* "Ordered Arrays of large latex particles organized by vertical deposition." *Langmuir* **18**, 3319-3323 (2002).
- <sup>22</sup> Wostyn, K., *et al.* "Optical properties and orientation of arrays of polystyrene spheres deposited using convective self-assembly." *Journal of Chemical Physics* **118**, 10752-10757 (2003).
- <sup>23</sup> McLachlan, M. A., Johnson, N. P., De La Rue, R. M. and McComb, D. W. "Thin film photonic crystals: synthesis and characterisation." *Journal of Materials Chemistry* **14**, 144-150 (2004).
- <sup>24</sup> Im, S. H., Kim, M. H. and Park, O. O. "Thickness control of colloidal crystals with a substrate dipped at a tilted angle into a colloidal suspension." *Chemistry of Materials* **15**, 1797-1802 (2003).
- <sup>25</sup> Miguez, H., *et al.* "Evidence of FCC crystallization of SiO<sub>2</sub> nanospheres." *Langmuir* **13**, 6009-6011 (1997).
- <sup>26</sup> Amos, R. M., *et al.* "Fabrication of large-area face-centered-cubic hard-sphere colloidal crystals by shear alignment." *Physical Review E* **61**, 2929-2935 (2000).
- <sup>27</sup> Ashcroft, N. W. and Mermin, N. D. "Solid State Physics", Saunders College Publishing, Philadelphia (1976).
- <sup>28</sup> Goldenberg, L. M., J. Wagner, J. Stumpe, B. R. Paulke and E. Gornitz. "Optical properties of ordered arrays of large latex particles." *Physica E-Low-Dimensional Systems & Nanostructures* **17**, 433-435 (2003).
- <sup>29</sup> Velikov, K. P., Christova, C. G., Dullens, R. P. A. and van Blaaderen, A. "Layer-by-layer growth of binary colloidal crystals." *Science* **296**, 106-109 (2002).

## CHAPTER 3

---

# Optical study of the L-pseudogap in thin film opals

### 1. Introduction

Since the early stages of photonic crystal research, calculated band structures have been used for the design of systems with certain properties (i.e. existence of a PBG, anomalous refraction, etc.). These predictions were then employed as guidelines for the fabrication of the crystals. In most cases, the predictions were aimed at systems having forbidden frequency intervals which were then characterized by means of reflectance or transmittance spectroscopy.

Energy bands have also been employed as a means of control in the process of photonic crystal fabrication. In the particular case of artificial opals, the spectral position of the L-pseudogap (either by direct comparison with calculated bands or by using a modified Bragg's law) has been used to determine lattice parameters (and therefore sphere sizes),<sup>1-3</sup> pore filling fraction in the fabrication of composite and inverse opals of different materials,<sup>1-7</sup> deformations (accidental or intentional) of the system during its synthesis,<sup>8,9</sup> etc.

Energy bands are calculated assuming a perfect and infinite periodic system, while real systems to be characterized are certainly finite and present a number of imperfections. This brings up a number of questions on the validity of the comparison between experimental results and calculated bands. From a practical point of view one may ask oneself for what size does the crystal reach the infinite crystal behaviour (in terms of optical properties) so that a comparison with the band structure is reliable. From a more fundamental perspective, it is interesting to know how the optical properties of the crystal evolve as a function of its size.

In this chapter a study is presented on the evolution of the L-pseudogap as a function of the number of  $\{111\}$  planes for thin film opals made of polystyrene spheres. The study is carried out by means of reflectance and transmittance spectroscopy along the  $\Gamma L$  direction in reciprocal space, that is, normal incidence on the  $\{111\}$  planes parallel to the surface. The evolution of several parameters

usually employed for comparing the experimental peaks with the pseudogap extracted from the bands (such as the full width at half maximum, FWHM, its centre and edges) is studied as a function of sample thickness as well as substrate nature. Experimental results are found to be properly described in a qualitative manner by predictions obtained with the Scalar Wave Approximation (SWA).

Afterwards, the influence of disorder -which is known to modify the optical response of photonic crystals- on the previous measurements is considered in order to elucidate whether the former results may be explained solely in terms of finite size effects and the interaction between the crystal and electromagnetic radiation.

Once the threshold thickness for which the optical properties of the system reach a stationary behaviour has been determined, angle resolved reflectivity is used to experimentally determine the band structure along high symmetry directions.

## 2. Optical properties: finite size effects

The samples used have been described in Chapter 2. They consist of thin film opals made out of polystyrene spheres. Normal incidence reflectance and transmittance measurements were carried out with a microscope attached to a FTIR spectrometer (Bruker IFS-66/S). For these measurements a 4x objective with a 1.5mm aperture

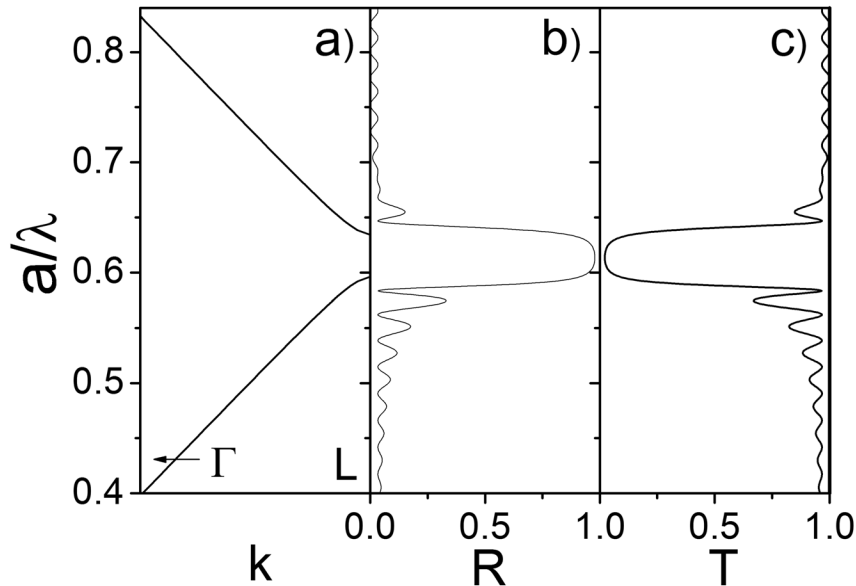
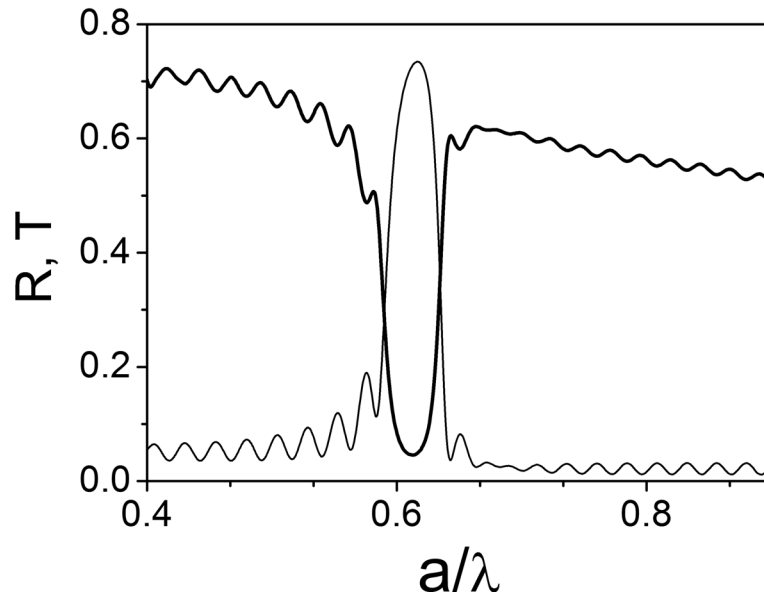


Figure 1: (a) Band structure for a wave vector parallel to the  $\Gamma L$  direction in a polystyrene opal. (b) Reflectance and (c) transmittance spectra calculated for a sample 25 layers thick. All calculations were performed with the SWA.

was used. A tungsten halogen lamp was used as light source. The probe beam had a diameter at its focus of 375nm and an angular aperture of 6°. Detection was performed with a nitrogen cooled InSb detector.

The spectral region considered for this study comprises reduced frequencies  $0.35 < a/\lambda < 0.9$ . Along the  $\Gamma L$  direction, the band structure in this region presents a linear behavior similar to that of a homogeneous medium which splits at the edges of the Brillouin zone as a consequence of Bragg diffraction by the  $\{111\}$  planes (figure 1a). In the absence of absorption and/or disorder reflectance and transmittance measurements provide identical information as all light that is not reflected is transmitted. This can be appreciated in figure 1, where the band structure is represented together with reflectance and transmittance spectra calculated with the SWA model.<sup>10</sup>

The spectra present high (low) reflectance (transmittance) for those frequencies contained in the pseudogap. Transparency regions filled with secondary oscillations are found at both sides of the gap, in the spectral region where calculated bands are linear. These oscillations are Fabry-Perot resonances originated by interference of light reflected at both interfaces of the sample.<sup>10</sup>



*Figure 2: Reflectance (thin line) and transmittance (thick line) spectra measured at normal incidence on a sample 25 layers thick grown on a glass substrate.*

In the presence of disorder light propagating through the crystal is scattered by the different imperfections of the lattice and the incident beam is attenuated, a diffuse cone originating around it. This affects reflectance and transmittance spectra in different manners. Reflectivity peaks become less intense,<sup>11,12</sup> rounded in shape,<sup>3</sup> asymmetric and may even become spectrally wider in the presence of a

mosaic spread.<sup>13</sup> Fabry-Perot oscillations at both sides of the peak lose definition. On the other hand transmission increases for those frequencies contained in the pseudogap, while decreasing for those frequencies outside.<sup>14-16</sup> Transmission may also present spectral broadening by a mosaic spread.<sup>17</sup> These changes may be appreciated in figure 2, where reflectance and transmittance spectra measured at normal incidence on a sample 25 layers thick grown on a glass substrate are presented.

In a disordered sample the transmittance outside the pseudogap decreases with sample thickness as well as with refractive index contrast and thus hampers the determination of parameters such as the FWHM commonly used to compare experimental results with calculated bands. This is the reason why reflectance spectra are the customary measurements to compare with theory. We will then concentrate on this type of measurements to study the evolution of the optical response of our samples as a function of thickness. In particular, attention will be paid to the evolution of the reflectance peak; its FWHM, centre and edges, all being regularly used for comparison with energy bands.

The band structure was calculated both, with the plane wave expansion method (PWEM)<sup>18</sup> and with the SWA model. Since the band structure represents the dispersion relation of the infinite crystal, it can not account for the evolution of the optical properties of the finite system. In order to model this we used spectra calculated with the SWA. Figure 3 shows experimental and calculated reflectance spectra for a sample grown on a glass substrate together with the corresponding energy bands. Both spectra present a maximum in reflectance for those frequencies contained in the stop band, surrounded by secondary oscillations where the dispersion relation behaves linearly. These Fabry-Perot oscillations may then be used to estimate the sample thickness provided we know the effective refractive index  $n_{\text{eff}}$  of the crystal. For inhomogeneous media,  $n_{\text{eff}}$  is usually defined in the long wavelength limit ( $\lambda \rightarrow \infty$ ) where the wavelength is too large to “see” the inhomogeneities of the structure. But then again, photonic crystals are not usual inhomogeneous media since multiple scattering takes place in a coherent way which leads to the formation of a well defined dispersion relation divided into bands. As long as the incident beam can couple to these bands, the crystal behaves as a transparent medium with a  $n_{\text{eff}}$  which may be estimated from the slope of the band.<sup>19</sup> In order to find the crystal thickness we consider secondary oscillations in the low energy region below the pseudogap. For these frequencies the slope of the band hardly varies and we may then associate a well defined  $n_{\text{eff}}$  (1.41) to the crystal.

If we compare the two spectra in figure 3 we can appreciate how the spectral position of the Bragg peak and the Fabry-Perot oscillations coincide, although it can be seen that the latter present a mismatch for reduced frequencies above 0.85 where experimental ones seem to become closer to each other. This agrees with the fact that bands calculated exactly with the MPB present a smaller slope at these frequencies than those calculated with the SWA, which implies a larger effective refractive index. This difference in the calculated bands is likely associated to the

fact that the SWA does not take into account higher order diffractions by  $\{111\}$  planes, as well as diffraction by other families of planes (see appendix 1). Besides these minor discrepancies we can see that both, the intensity as well as the width of the peaks, present differences. These will be dealt with later on.

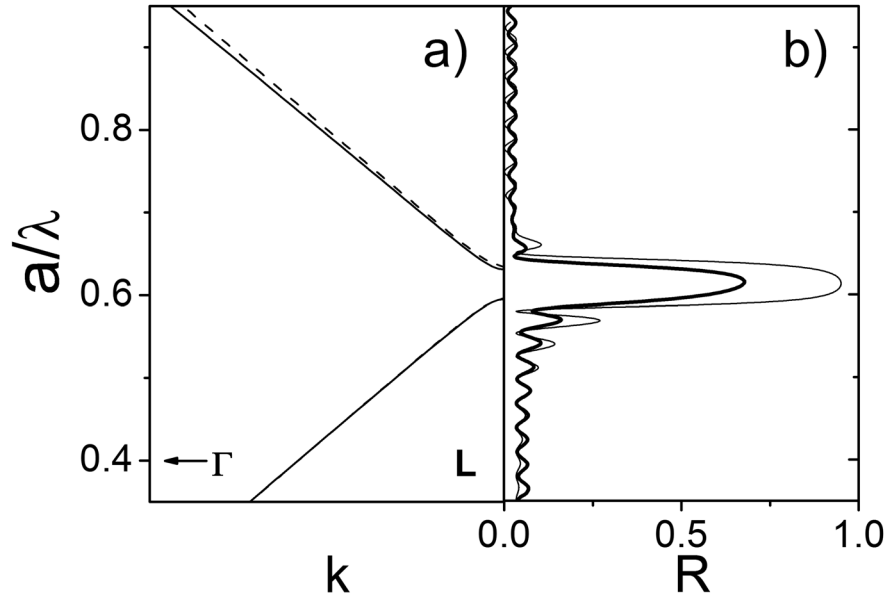


Figura 3: (a) Band structure for a polystyrene opal calculated with the PWEM (solid line) and the SWA (dashed line). Reflectance spectra measured (thick line) and calculated with the SWA (thin line) for an artificial opal 23 layers thick.

We now proceed to study the evolution of the reflectance peak; its FWHM, centre and edges as a function of crystal thickness. This is done for samples grown on glass and crystalline silicon substrates. Results are presented in figure 4. Experimental results appear as open (glass substrate) and solid circles (silicon substrate). Horizontal lines correspond to the spectral position of the pseudogap for the infinite crystal as extracted from band structure calculation performed with the PWEM (dashed line) and SWA (solid line). Curves indicate predictions obtained with SWA for finite samples grown on silicon (solid) and glass substrates (dashed).

Figure 4a represents the evolution of the FWHM edges. For both types of substrate we can appreciate a similar trend, although for the case of the silicon substrate the edges are displaced to larger frequencies. In both cases we can see that for samples thicker than 35 layers experimental results converge to the pseudogap edges predicted by the PWEM. This behavior is qualitatively reproduced by the SWA results.

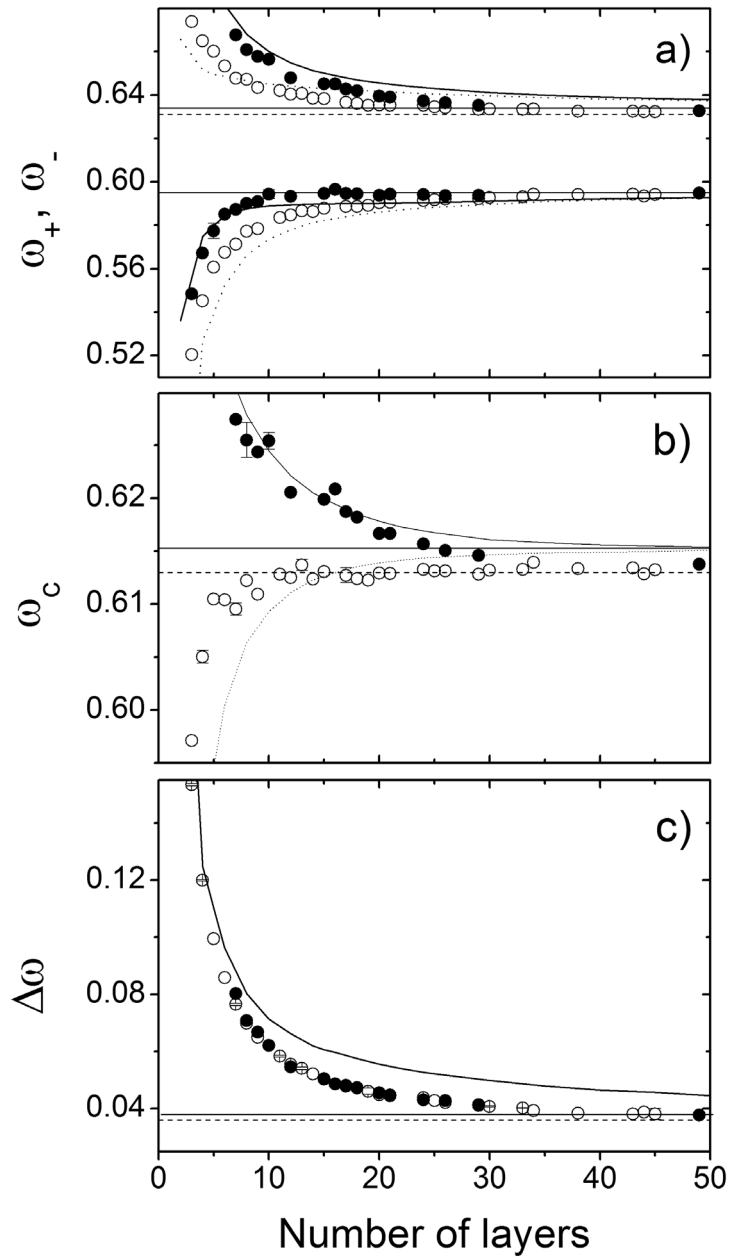


Figure 4: Evolution of the edges  $\omega_+$ ,  $\omega_-$  (a), center  $\omega_c$  (b), and FWHM itself  $\Delta\omega$  (c) as a function of the number of  $\{111\}$  planes parallel to the crystal surface. Experimental results correspond to samples grown on silica (open circles) and silicon (closed circles) substrates. Dotted and solid curves represent predictions obtained with the SWA for those systems. Horizontal lines correspond to predictions for the infinite crystal obtained from bands calculated with PWEM (dashed) and SWA (solid).

The difference between both types of substrate becomes even more pronounced if we consider the centre of the FWHM (figure 4b). Here we see that, depending on the type of substrate, glass or silicon, the peak centre will either monotonically increase or decrease in frequency as a function of sample thickness. Finally, both sets of data tend to the infinite crystal limit extracted from the bands, although in the case of the glass substrate this happens for thinner samples than in the silicon one, as only ten layers are needed. Again SWA predictions qualitatively coincide with experimental results, and converge to the limit extracted from the bands calculated under that approximation.

Since the only difference between both substrates considered is their refractive index the above results indicate that in the initial stages of formation of the Bragg peak, which will ultimately reveal the existence of a forbidden frequency interval, and which happens as a consequence of multiple scattering between crystal planes, reflections at the crystal boundaries are relevant. As one would expect, as the thickness of the crystal increases the effect of the interfaces decreases and the internal reflections dominate the optical response as indicated by the tendency of experimental results towards the infinite crystal limit.

If we now consider the evolution of the FWHM (figure 4c), we find that the experimental results coincide for both substrates. The FWHM of the reflectance peak decreases with crystal thickness until reaching a stationary value, close to that predicted by the PWEM for the infinite crystal, in samples 35 layers thick. The SWA predictions reproduce qualitatively this trend, only they seem to overestimate the experimental value. Besides the limitations of the SWA, which only account for one third of this overestimation (see appendix 1 and horizontal lines in figure 4d), another source of error could be the fact that the measurements were performed with a certain angular aperture. This, however would lead to a broadening of the experimental peak which can be estimated to be as small as 2%. The possible impact of structural disorder will be dealt with in the following section.

The FWHM being independent on the substrate used, we can assume this parameter as representative of the interaction of the photonic crystal with electromagnetic radiation alone in the process of the stop band formation. The FWHM can be further used to quantify the finite size effects on the optical response of the crystal. Nevertheless, the effect of finitude on the spectral position of the Bragg peak must be taken into account since  $\omega_c$  is usually employed for determining lattice parameters and filling fractions. Therefore, in the absence of a characterization like the one presented here, using  $\omega_c$  could lead to incorrect results for thin samples. Specially considering that thin film opals are becoming the most spread technique in self assembled photonic crystals, and any application based on them will certainly require the use of miniaturized systems.

In a publication concerning the finite size effects in similar samples (silica thin film opals), Bertone *et. al.*<sup>20</sup> only considered the evolution of the FWHM. Their experimental results were overestimated by SWA predictions for thin samples and underestimated for thick samples. This is probably due to the fact that they carried out their comparison from transmission measurements in which “a smoothly

varying monotonic background” (sic) was subtracted. This background was most likely due to disorder, which effect is expected to be more evident for thicker samples. Further, in their work no comparison was made with any band structure prediction for the infinite crystal.

### 3. Effects of disorder

Next, the effect of structural disorder in the previous measurements is investigated in order to determine whether it contributes to the observed FWHM or, on the contrary, experimental results are solely due to finite size effects and the interaction between electromagnetic radiation and the photonic crystal.

As mentioned earlier, in the presence of disorder the optical properties of the sample will be altered with respect to those of the perfect crystal. On the one hand imperfections in the unit cell such as missing spheres or spheres displaced from its lattice position or having size dispersion will generate scattering. In the presence of a mosaic spread, with the crystal comprising several domains with their normal oriented in different directions, the Bragg peak in normal incidence may present inhomogeneous broadening. In our case we do not expect such broadenings due to the fact that the sample is grown on substrates flat within a few nanometers over distances much larger than the probe beam. SEM observations further confirm this, as inspection of cleaved samples evidenced domains which run the entire crystal. Stacking faults in the direction parallel to the surface are also a common type of disorder in opal based photonic crystals. Since this type of disorder does not affect the periodicity in the probe direction we do not expect that it modifies the optical response, at least in the spectral region of interest.<sup>21,22</sup>

According to the above, we expect the main contribution from disorder in our case to be the attenuation of the incident beam with the consequent generation of diffuse intensity. This will affect the optical properties in a different way depending on the spectral region under consideration. This can be appreciated if we estimate the diffuse intensity as a function of reduced frequency. Since polystyrene does not absorb for the frequencies considered,<sup>23</sup> diffuse intensity  $D$  may be deduced from reflectance and transmittance measurements as  $D=1-R-T$ . That is, as all light that is not reflected or transmitted in the incident direction. This is shown in figure 5 for a sample 38 layers thick, together with the corresponding band structure.

Experimental spectra of scattered light present three distinct features: a monotonic increase for those frequencies outside the pseudogap (which corresponds to the commonly observed decrease in transmitted intensity<sup>2-17</sup>), an enhancement at its low frequency edge and an abrupt decrease for those frequencies within it. This behaviour may be explained taking into account the way light propagates inside the crystal in this spectral range as well as the band structure for frequencies adjacent to the incident one.<sup>17,24</sup>

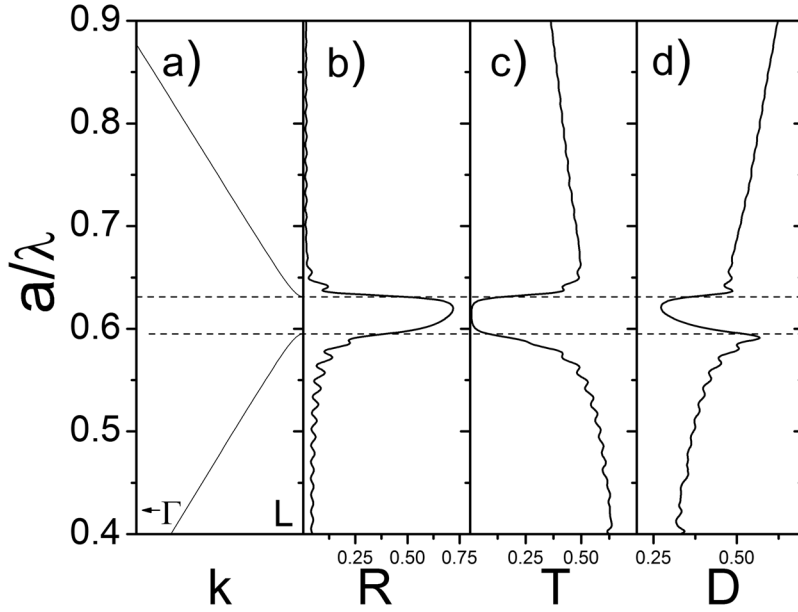


Figure 5: (a) Band structure calculated with the PWEM. (b) Reflectance, (c) transmittance and (d) diffuse intensity spectra for a sample 38 layers thick. Horizontal dashed lines represent the theoretical edges of the pseudogap.

As mentioned previously, in the presence of disorder light propagating through the crystal will eventually scatter, most likely elastically, and this will change its propagation direction within the crystal. That is, its wave vector will change by an amount  $\Delta\mathbf{k}$ . For those frequencies at the pseudogap edges photonic bands flatten and light spends a long time inside the crystal (for a perfect infinite crystal photonic modes corresponding to these frequencies are stationary waves). Therefore the probability for scattering events to take place increases. One would therefore expect an enhancement in diffuse intensity. On the other hand, for those frequencies contained in the pseudogap, light is exponentially attenuated. Therefore the probability of light being scattered will be smaller than for frequencies out of the pseudogap or at its edges. The penetration length inside the crystal being a minimum for those frequencies near the pseudogap centre, one would expect a smaller contribution to the scattered intensity for them.

According to the above, the diffuse intensity spectra should present a symmetric behavior with respect to the pseudogap centre, with maxima at its edges and a dip within it. The experimentally observed asymmetry can be accounted for by the band structure for directions adjacent to the incident one. That is, for those directions along which scattered intensity will propagate.<sup>24</sup>

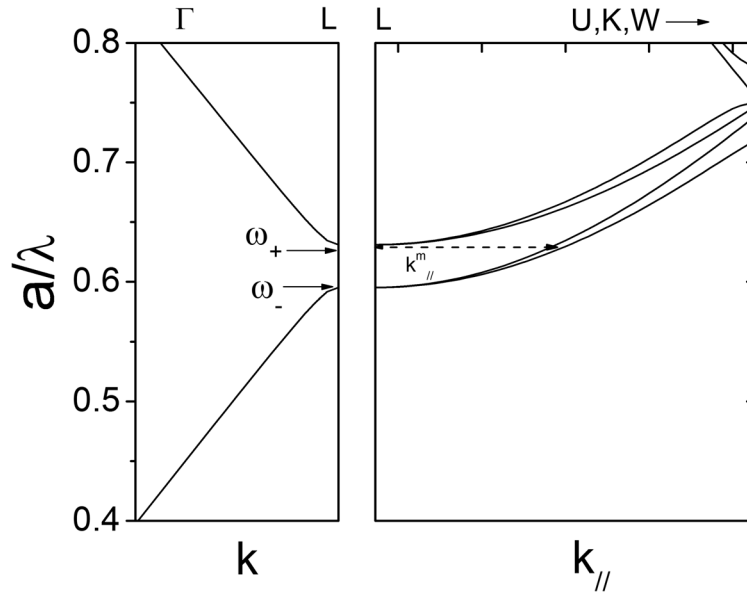


Figure 6: Band structure calculated for a wave vector parallel to the  $\Gamma L$  direction in reciprocal space (left panel) and for a set of adjacent wave vectors with their tip in the hexagonal facet of the Brillouin zone (right panel).

Plotted in figure 6 are the bands for a wave vector  $k$  parallel to the  $\Gamma L$  direction (left panel) and for a set of adjacent wave vectors with their tip in the hexagonal facet of the Brillouin zone (right panel). The bands for such a set of wave vectors are identical independent of the direction in the hexagonal facet provided we are not close to the edges. As the parallel component of the incident beam increases (that is, as the angle of propagation with respect to the  $\Gamma L$  direction increases) the pseudogap shifts towards higher frequencies in accordance with Bragg's law. Therefore, for scattering events taking place for frequencies close to the low energy edge, accessible states will be available for small  $\Delta k$  and are therefore more probable. On the contrary, as we move to higher frequencies, the  $\Delta k$  needed for a scattered photon to find an allowed state is larger and the process becomes less probable. This explains that we only observe an enhancement of diffuse intensity for the low frequency edge of the pseudogap, and that the minimum happening inside it is markedly asymmetric.

It is interesting to explore the contributions to the total diffuse intensity in reflection and transmission. Some preliminary measurements were carried out with an integrating sphere (CARY 5E spectrophotometer). Diffuse reflectance measurements were readily available with the proper sphere configuration. For the diffuse transmission some modifications were needed. Since the sphere only allows for total transmission measurements, the zero order beam had to be blocked in order to obtain the diffuse contribution. A quantitative comparison between the

results obtained (represented in figure 7) and the previous ones is not feasible since the probe beam was rather large (1.5 cm), so that regions with different thicknesses (10-14 layers) were simultaneously probed.

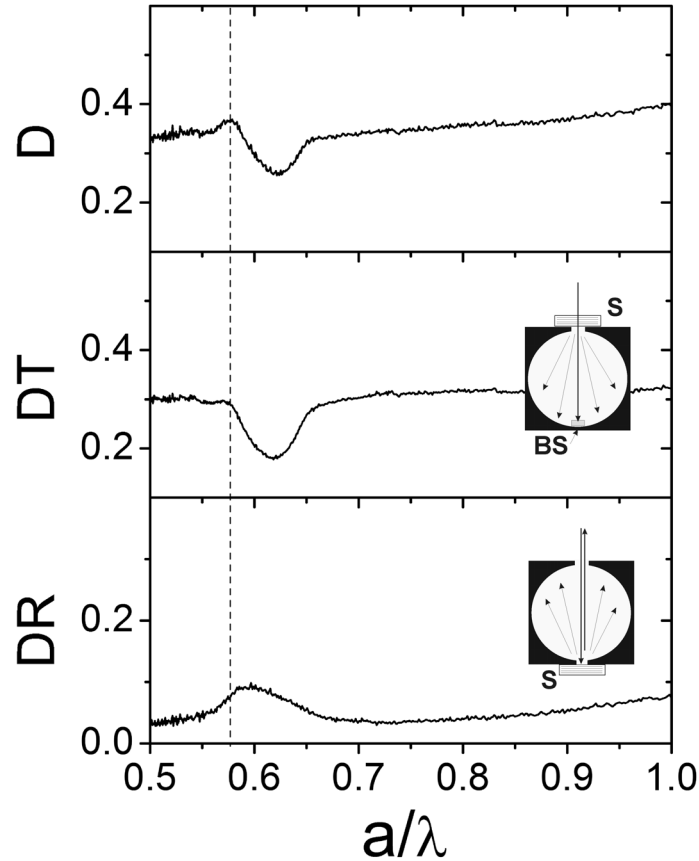


Figure 7: Total diffuse reflectance (bottom), transmittance (middle) and their sum (top) for a sample grown on a glass substrate with 10-14 layers, collected with an integrating sphere. Insets show the configuration used for each measurement. S represents the sample and BS the beam stop for the zero order transmitted beam.

Nevertheless a number of things can be noted. In the diffuse reflectance we observe a small background, over which an enhancement appears for those frequencies contained in the pseudogap. This enhancement is more pronounced towards the red edge. On the contrary, for transmission the background is higher and the pseudogap region presents a lower intensity, also larger for small frequencies. The line shape of the diffuse intensity, estimated as the sum of diffuse reflectance and transmittance, reproduces the previously mentioned behavior with an enhancement at the red edge of the Bragg peak followed by a decrease with respect to the monotonically increasing background.

A detailed analysis of the angular distribution of both, diffuse reflectance and transmittance, would be interesting as it seems that the behavior observed for the overall diffuse intensity results as a combination of the two. Recently, a study of the angular distribution of diffuse transmission was presented for strongly photonic crystals,<sup>25</sup> and successfully modeled by means of diffusion theory.

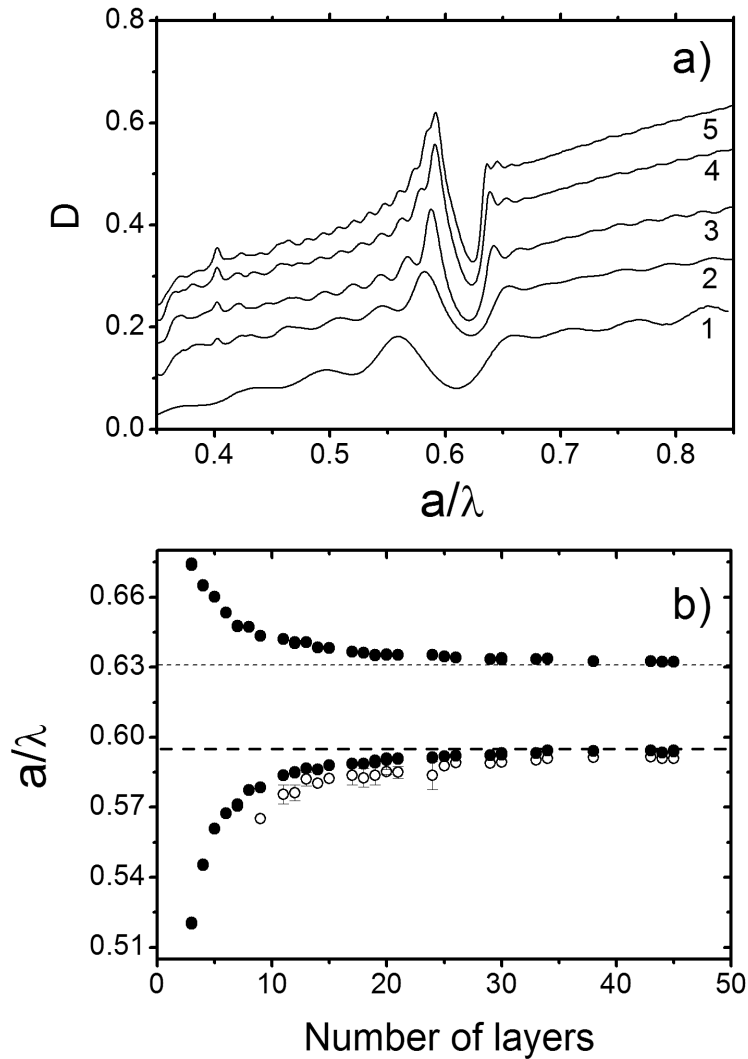


Figure 8: (a) Diffuse intensity measured as  $1-R-T$  for samples with different thickness grown on glass substrates. 1-5 correspond to samples having 10, 15, 25, 35 and 45 layers. (b) Position of the diffuse intensity enhancement (open circles) and FWHM edges (closed circles) as a function of the number of layers.

If we now represent the diffuse intensity spectra measured as  $1-R-T$  for a number of samples with increasing thickness (figure 8) we find a behavior common to all of them. The diffuse intensity enhancement present for low frequencies and

the inhibition which follows it are present in samples as thin as 10 layers. As the thickness of the crystal increases we see how the enhancement becomes more defined and shifts towards high frequencies. Also the region of inhibition narrows, and its recovery for high frequencies becomes more abrupt.

Since the existence of both enhancement and inhibition is a consequence of the band structure of the system, its existence for samples only 10 layers thick and its further evolution can be considered as a signature of the band formation. As a matter of fact, if we compare the evolution of the enhancement feature with that of the low frequency edge of the FWHM (figure 8b) we can appreciate an analogous behavior which converges with the number of layers. Since the enhancement should take place right at the red edge of the pseudogap (where penetration length is a maximum, and the cone of forbidden directions a minimum), its convergence with  $\omega_+$  would indicate the validity of this parameter to determine the pseudogap in samples with an appropriate thickness.

A similar behavior of the diffuse intensity was observed by Astratov and co-workers<sup>17</sup> for bulk artificial opals. In their work a double enhancement, with barely any inhibition in between, was observed and associated to the edges of the pseudogap. The existence of a rather large ( $\pm 5^\circ$ ) mosaic spread in their samples made an exact association between enhancement and pseudogap edges difficult. Further, no comparison with calculated bands was presented.

In order to determine the effect that scattering by defects could have on the measurements presented in figure 4, we have compared the FWHM of samples

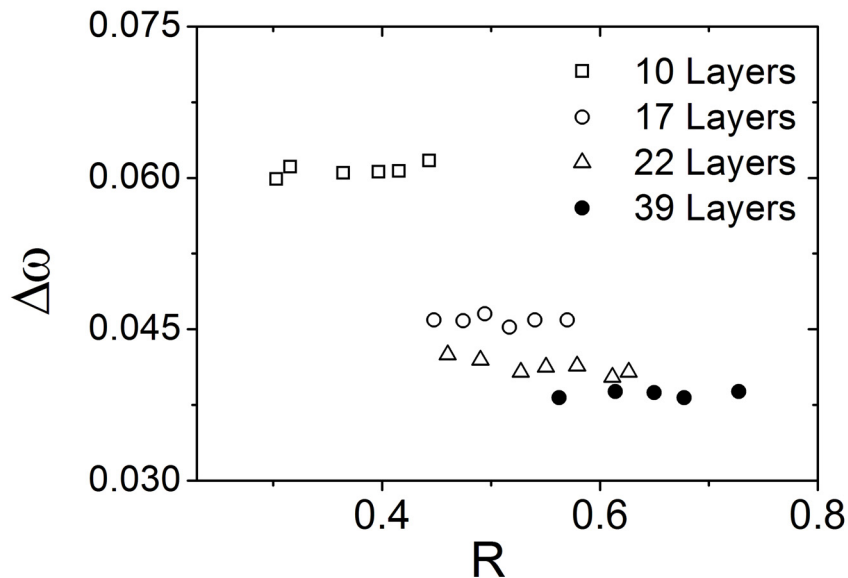


Figure 9: FWHM for samples having the same thickness (grouped by symbols) but presenting a different reflectivity.

which, having the same number of layers presented a lower reflectivity, indicating a larger effect of disorder. To carry out these measurements we employed samples grown at temperatures between 55°C and 40°C. The results are shown on figure 9. Here we can see that, for variations in reflected intensity above 15%, no noticeable changes in the FWHM are observed, or in  $\omega_0$  for that matter. Thus it seems that, although the existence of a stronger diffuse scattering for those frequencies near the stop band edges may affect the FWHM of the reflectivity peak, it is probably not significant in our case. Therefore we can consider the observed FWHM as a combination of finite size effects and photonic interaction of the system.

Although reflectance measurements are better suited for comparison with calculated bands, transmittance ones yield information on the propagation of light

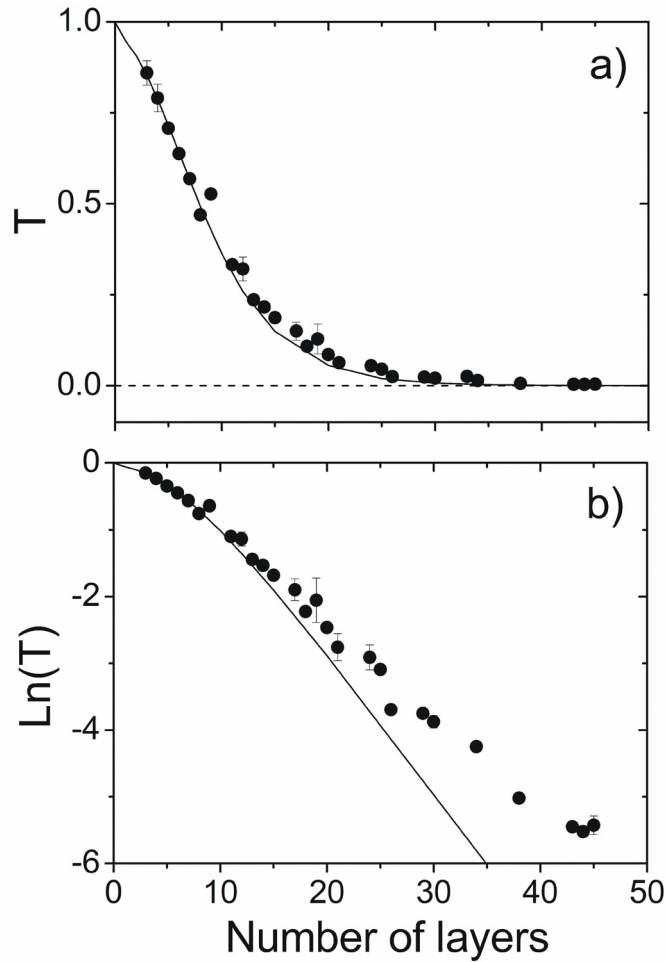


Figure 10: (a) Minimum transmittance measured as function of crystal thickness for samples grown on glass slides (circles) together with theoretical predictions from the SWA (lines). (b) Same results for the logarithm of the transmittance.

through the entire crystal thickness. From the latter one may extract the extinction length ( $l_{\text{ext}}$ ) defined as the distance light must travel inside the crystal in order to be attenuated by a factor  $e$ . In figure 10 we have plotted the maximum attenuation of the transmitted beam as a function of crystal thickness and compared it with the SWA predictions. In figure 10a  $T$  is plotted versus the number of layers and an excellent agreement is observed for experiment and theoretical predictions.

In order to estimate  $l_{\text{ext}}$  we plot  $\text{Ln}T$  versus thickness, as in figure 10b. It can be seen how experiment and theory present an excellent agreement for samples up to 10 layers thick, where the linear behavior has not been achieved yet. This behavior appears for thicker crystals, and it is evident that experimental results and theoretical predictions present a different slope, and therefore a different extinction length. Here we have estimated an  $l_{\text{ext}}=8.5$  {111} planes from the experiment, versus the 5 planes predicted by the SWA. The fact that experimental  $l_{\text{ext}}$  exceeds the theoretical one has been reported previously for artificial opals<sup>15,20</sup>. While for ideal crystals described in theory the attenuation at gaps is entirely due to Bragg diffraction (we may refer to a Bragg attenuation length,  $l_{\text{B}}$ ), in real crystals presenting disorder  $l_{\text{ext}}$  is a combined effect of Bragg attenuation and scattering by defects causing  $l_{\text{ext}} > l_{\text{B}}$ . Numerical simulations performed for 2D crystals<sup>26</sup> also reproduce this trend,  $l_{\text{ext}}$  increasing with the amount of structural disorder.

To the present date, there has been no satisfactory relationship between a quantification of structural disorder, experimentally observed  $l_{\text{ext}}$  and the theoretically predicted  $l_{\text{B}}$ . Although initially it was suggested<sup>14</sup> that the experimentally measured  $l_{\text{ext}}$  would be just the addition of extinction associated to disorder and Bragg diffraction, the above results would indicate that it is likely a combination of both effects.

## 4. Angle resolved measurements

Once the threshold thickness for which the optical response of our samples at normal incidence in the spectral region of the pseudogap reaches a stationary behaviour (comparable to the infinite crystal behavior predicted by the bands), we proceed to study the optical properties for adjacent wave vectors whose parallel component is directed towards high symmetry points in the first Brillouin zone.

Experimental measurements were carried out in reflectance using a non-polarized white light beam extracted from a tungsten lamp. The beam had an angular aperture of 3° full angle and a diameter of 1mm. The angular range covered in the experiments was restricted to  $20^\circ < \theta < 75^\circ$  ( $\theta$  being the angle between the incident beam and the sample normal) due to limitations imposed by the experimental set-up, represented in figure 11.

In angle resolved specular reflectance measurements, the geometry of the experiment is such that the incident and reflected beam, as well as the normal to the sample, are all contained in a plane, known as the diffraction plane (see figure 12). In order to orient the diffraction plane with respect to the Brillouin zone, and carry

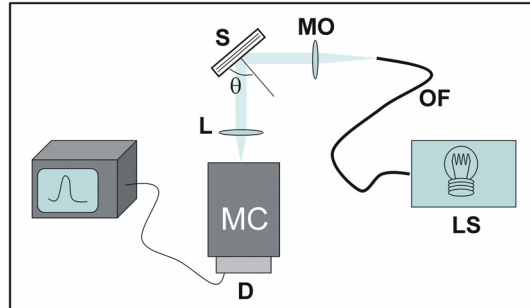


Figure 11: Experimental set-up. White light from a tungsten lamp (LS) is coupled to an optical fibre (OF) at the end of which an inverted microscope objective (MO) is placed which collimates the beam. This impinges on the sample (S), which is mounted on a goniometer, with an angle  $\theta$ . The specularly reflected beam is focused on the entrance slit of a monochromator (MC) and is then collected by a germanium detector (D).

a subsequent comparison with calculated bands, the optical diffraction patterns discussed in chapter 2 were used. As it was mentioned, the hexagonal diffraction patterns may be associated with points of the 2D reciprocal lattice present at the sample surface and therefore can be used to determine its Brillouin zone. Since the surface Brillouin zone is just an image of the hexagonal facet of the 3D one with identical orientation<sup>27</sup>, the diffraction pattern may be used to orient the 3D crystal. According to this, if the sample is rotated around an axis parallel to the growth direction (figure 12a) the diffraction plane coincides with the plane containing the points  $\Gamma$ , L and U (K) in the Brillouin zone. If the rotation axis is now perpendicular to the growth direction, the diffraction plane contains the  $\Gamma$ , L and W points (figure 12b). When orienting the sample in this way no distinction can be made between the U and K points, since both are located at the centre of identical sides of the hexagonal facet. For our purposes this does not represent an inconvenience since bands calculated along the LU and LK trajectories are identical for artificial opals.<sup>28</sup>

Before carrying out the angle resolved measurements the probed region was carefully selected in order to make sure that both, its thickness and orientation are well known. This is necessary if one wants a comparison with energy bands to be reliable. As the angle of incidence increases the spot size on the sample will increase from a circle with a 1mm diameter for normal incidence to an ellipse with a  $\sim 2.5$  mm long axis along the diffraction plane. Therefore sample regions with these dimensions were sought for.

The probed region was restricted to the central part of the sample in order to avoid the edges (where crystal orientation deviates due to meniscus shape) and the top (where crystal thickness varies abruptly and regions with  $\{200\}$  orientation

may appear). Crystal orientation was checked with optical diffraction, and thickness homogeneity with normal incidence reflectance measurements.

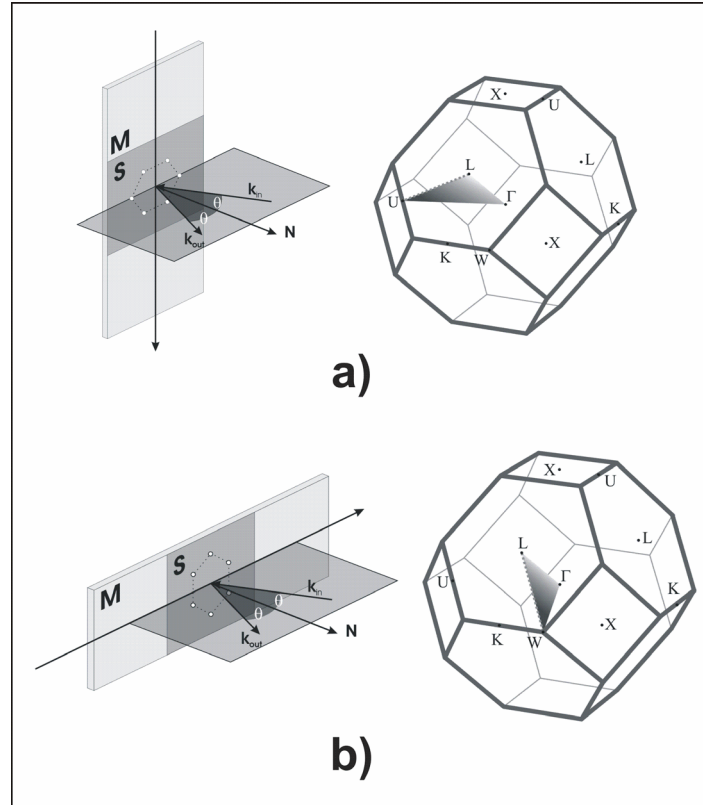


Figure 12: Geometry of angle resolved reflectance measurements. The sample (S) appears as dark grey on the substrate (M). The incident ( $\mathbf{k}_{in}$ ) and reflected ( $\mathbf{k}_{out}$ ) wave vectors define the diffraction plane together with the sample normal (N). The growth direction is indicated by an arrow. If the sample is rotated around a vertical axis parallel to this direction (a) the diffraction plane contains the  $\Gamma$ , L and U (K) points. If the rotation axis is now perpendicular to the growth direction, it is the plane containing the  $\Gamma$ , L and W points that we must consider.

Figure 13 shows reflectance measurements for different angles of incidence on a sample 34 layers thick grown on a glass substrate. There are two sets of measurements corresponding to two equivalent orientations of the sample. In figure 13a the rotation axis is parallel to the growth direction, as sketched in figure 12a. In figure 13b the sample has been rotated  $60^\circ$  around its surface normal. According to the above discussion in both situations the incident and reflected wave vectors are contained in the plane defined by the  $\Gamma$ , L and U (K) points, so that bands calculated along those directions were used for comparison (figure 13c).

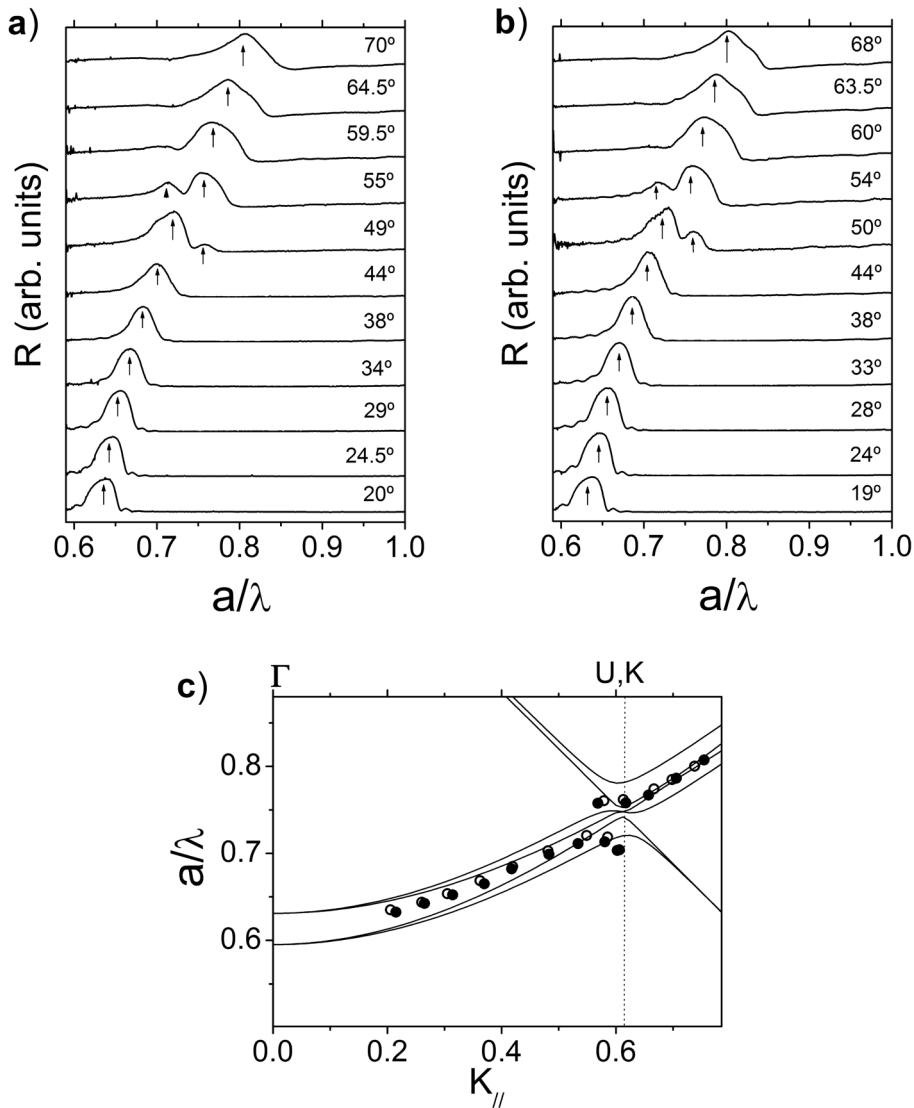


Figure 13 (a) Reflectance spectra (sample 34 layers thick grown on a glass substrate) for different angles of incidence as the sample is rotated around an axis parallel to the growth direction. (b) Similar measurements after rotating the sample  $60^\circ$  around its normal. (c) Calculated bands along the LU direction (lines) and experimental results for the situations a) and b) (filled and empty circles). The vertical line indicates the boundary of the Brillouin zone at the U/K point.

Figure 13c shows a comparison between experimental results and calculated bands. To represent the peaks, its central frequency was chosen. It can be seen that for small angles of incidence the reflectance peak follows the energy bands which, in that spectral region, reproduce Bragg's law for the  $\{111\}$  family of planes. As the

angle of incidence increases, a new reflectance peak appears at higher energies ( $\theta \sim 50^\circ$ ). For even larger angles, the Bragg peak disappears while the high frequency peak becomes more intense and prevails. This behavior is reproduced by the bands which undergo an anticrossing in this frequency range. A similar behavior was observed for inverse<sup>29</sup> and direct opals<sup>30</sup> and explained in terms of strong coupling between waves simultaneously Bragg diffracted by the  $\{111\}$  and  $\{200\}$  families of planes at the U point in reciprocal space. The situation is sketched in figure 14, where the section of the Brillouin zone passing through the  $\Gamma$ , X, L and U points is represented (corresponding to figure 12a). For normal incidence, a wave vector  $\mathbf{k}_{in}$  with its tip at the L point is Bragg diffracted by the  $\{111\}$  planes so that  $\mathbf{k}_{in} = \mathbf{k}_r + \mathbf{G}_{111}$ , where  $\mathbf{G}_{111}$  is the reciprocal lattice vector associated with that family of planes and  $\mathbf{k}_r$  the wave vector of the diffracted beam. This situation holds as the incident wave vector sweeps the Bragg plane defined by the LU segment with its tip (figure 14b). But as  $\mathbf{k}_{in}$  reaches the U point, the Bragg condition is simultaneously satisfied for the  $\{111\}$  and  $\{200\}$  families of planes. Therefore the incident wave vector leads to two diffracted ones  $\mathbf{k}_r$  and  $\mathbf{k}'_r$ , which are coupled to  $\mathbf{k}_{in}$  by reciprocal lattice vectors  $\mathbf{G}_{111}$  and  $\mathbf{G}_{200}$ . In our case this situation may be caused by simultaneous Bragg diffraction by  $\{111\}$  and  $\{200\}$  planes (U point) or by  $\{111\}$  and  $\{-111\}$  planes (K point). It can be seen that this anticrossing appears for  $a/\lambda \sim 0.74$  and  $k_{||} \sim 0.6$ , which coincides with calculated bands. As can be seen in figure 13c, the two sets of experimental data coincide, as expected both being equivalent orientations.

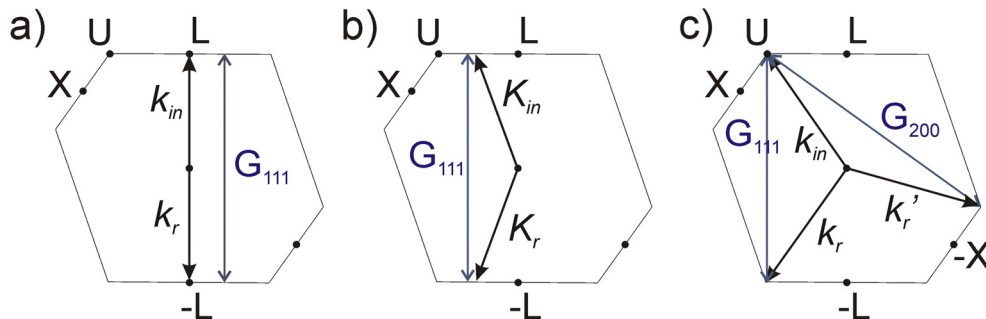


Figure 14: Geometry of the avoided crossing. Normal (a) and oblique (b) incidence when only diffraction by the  $\{111\}$  planes is excited. (c) Oblique incidence where simultaneous excitation of Bragg diffraction by the  $\{111\}$  and  $\{200\}$  planes take place.

Figure 15 represents similar measurements when the sample is oriented such that the parallel component of the incident wave vector points along the LW line. Reasoning as before, this situation is achieved when the sample is rotated around an axis contained in its surface and, either perpendicular or at  $30^\circ$  with respect to the growth direction (see figure 12b). Figures 15a and 15b represent reflectance

spectra as a function of incident angle for both cases. Now the situation is more complex than in the previous case since, when the incident wave vector points along the  $\Gamma W$  direction, the Bragg condition is simultaneously satisfied for three

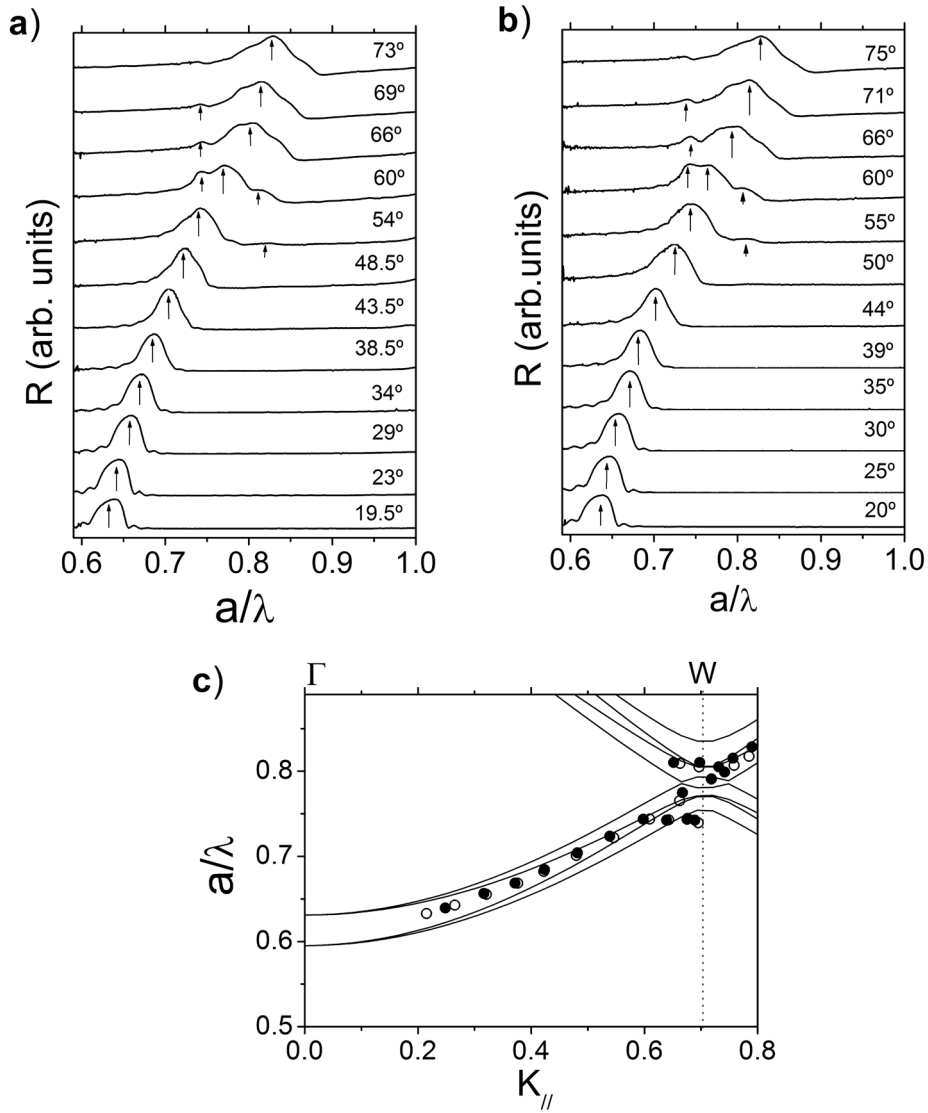


Figure 15 (a) Reflectance spectra for different angles of incidence as the sample is rotated around an axis perpendicular to the growth direction. (b) Similar measurements after rotating the sample  $60^\circ$  around an axis parallel to its normal. (c) Calculated bands along the  $LW$  direction (lines) and experimental results for the situations a) and b) (filled and empty circles). The vertical line indicates the boundary of the Brillouin zone at the  $W$  point.

families of planes:  $\{111\}$ ,  $\{200\}$  and  $\{-111\}$ . Now we must consider a situation similar to that represented in figure 14c only that there exist two diffracted wave vectors non coplanar with the diffraction plane defined by  $\Gamma$ , L and W, the latter being a point common to two hexagonal facets and a square one of the Brillouin zone.

In figure 15 we can see that, as predicted by the bands, the reflectance peak which appears at normal incidence increases its frequency for small angles. It is not until reaching  $\theta \sim 55^\circ$  that a second peak appears for higher frequencies. This is to be expected since the W point is the one lying furthest from the centre of the Brillouin zone, at the  $\Gamma$  point, and furthest from L in the hexagonal facet. At  $60^\circ$  we see how the Bragg peak branches, a new reflectivity peak appearing at lower frequencies, while the high frequency peak observed for  $54^\circ$  becomes more intense and moves to a lower frequency, as predicted by the calculated bands. For larger angles, the low frequency peak decreases in intensity and frequency, while the high frequency peak that appeared at  $54^\circ$  merges with the Bragg peak, which presents a complicated shape with two shoulders. The overall behavior of reflectivity peaks is well accounted for by the exact PWEM calculation.

Opposite to the situation at the U point where a clear anticrossing was evident in the optical response, at the W point we observe that the main reflectivity peak does not vanish at any stage. A possible reason for this behavior could be the existence of stacking faults which, although not having any effect on the optical response for normal incidence measurements in this energy range, are known to introduce additional reflectivity peaks for directions other than the incident<sup>16</sup>. This has been attributed to the presence of different periodicities in those directions as a consequence of the stacking disorder. But since the families of planes which intervene separately at the U and K points (i.e.  $\{-111\}$  and  $\{200\}$ ) are the same as those doing so together at the W point, any peak doubling effect would also be expected on the graphs shown in figure 13a and 13b. This not being the case, we expect the effects of stacking disorder, if present, not to affect the results presented in figures 15a and 15b. The situation at the W point being much more complicated, with Bragg diffraction bringing light along three non coplanar directions, makes a direct interpretation of the experimental results a challenging task. Nevertheless, the agreement with the calculated bands along that direction is satisfactory.

The occurrence of multiple diffractions flattens the bands and spans forbidden regions for large angular ranges.<sup>29</sup> The extent of these ranges will be determined by the refractive index contrast present in the material which, if sufficient, will lead to the appearance of a PBG. Although the contrast in our samples is below that of reference 24, where band flattening was much more pronounced, this is the first time in which this behavior is found for all the high symmetry directions in the hexagonal facet of the Brillouin zone.

## 5. Conclusions and future work

In this chapter we have presented an in-depth study of the finite size effects on the optical properties of thin film opals. The evolution of several parameters commonly used to associate the Bragg peak in reflectance with band structure calculations has been examined evidencing the need for a similar study prior to considering comparison with energy bands. Predictions extracted from the SWA prove this approach to qualitatively reproduce experimental results. The effect of finiteness on the Bragg peak is seen to disappear for this particular system (artificial opals made out of polystyrene spheres) for samples 35 layers thick.

A logical extension of this work would be towards systems with a refractive index contrast high enough as to present a full PBG. In that case, not only the evolution of the pseudogap but also of the PBG would be of interest.

Further, a detailed study on the influence of finite size effects on the dynamics of light inside a PC would be of great interest, since it is directly applicable to future devices. Similar studies have been performed in 1D systems<sup>31</sup> but a study for 3D crystals working in the visible range is lacking.

The effect of disorder on the optical properties of the samples has also been studied. It has been shown that the diffuse intensity generated as a beam passes through the crystal in presence of disorder is strongly frequency dependent and may only be explained taking into account the band structure of the system. In fact, the diffuse intensity may also be used to determine the red edge of the pseudogap for sufficiently thick samples (>35 layers). This diffuse intensity is responsible for the asymmetry present in the reflectance peak, and may affect its FWHM for sufficiently disordered samples. We believe this is not the case for our samples.

By means of angle resolved reflectivity we have studied the optical properties of the samples along high symmetry directions in the Brillouin zone. Experimental results are in good agreement with calculated bands and allow identifying band anticrossings at high symmetry points, characteristic of strong interaction between incident light and the crystal. Again, extending these measurements towards crystals with a high refractive contrast (ideally sufficient to open up a PBG) would yield valuable information on the formation of a PBG.

## 6. References

- <sup>1</sup> Richel, A., Johnson, N. P. and McComb, D. W. “*Observation of Bragg reflection in photonic crystals synthesized from air spheres in a titania matrix.*” Applied Physics Letters **76**, 1816-1818 (2000).
- <sup>2</sup> Blanco, A., *et al.* “*Large-scale synthesis of a silicon photonic crystal with a complete three-dimensional bandgap near 1.5 micrometres.*” Nature **405**, 437-440 (2000).
- <sup>3</sup> Allard, M., Sargent, E. H., Kumacheva, E. and Kalinina, O. “*Characterization of internal order of colloidal crystals by optical diffraction.*” Optical and Quantum Electronics **34**, 27-36 (2002).
- <sup>4</sup> Wijnhoven, J. and Vos, W. L. “*Preparation of photonic crystals made of air spheres in titania.*” Science **281**, 802-804 (1998).
- <sup>5</sup> Miguez, H., *et al.* “*Bragg diffraction from indium phosphide infilled fcc silica colloidal crystals.*” Physical Review B **59**, 1563-1566 (1999).
- <sup>6</sup> Juarez, B. H., Ibisate, M., Palacios, J. M. and Lopez, C. “*High-energy photonic bandgap in Sb<sub>2</sub>S<sub>3</sub> inverse opals by sulfidation processing.*” Advanced Materials **15**, 319-323 (2003).
- <sup>7</sup> Garcia-Santamaria, F., *et al.* “*Photonic band engineering in opals by growth of Si/Ge multilayer shells.*” Advanced Materials **15**, 788-790 (2003).
- <sup>8</sup> Miguez, H., *et al.* “*Control of the photonic crystal properties of fcc-packed submicrometer SiO<sub>2</sub> spheres by sintering.*” Advanced Materials **10**, 480-483 (1998).
- <sup>9</sup> Sumioka, K., Kayashima, H. and Tsutsui, T. “*Tuning the optical properties of inverse opal photonic crystals by deformation.*” Advanced Materials **14**, 1284-1287 (2002).
- <sup>10</sup> Shung, K. W. K. and Tsai, Y. C. “*Surface Effects and Band Measurements in Photonic Crystals.*” Physical Review B **48**, 11265-11269 (1993).
- <sup>11</sup> Thijssen, M. S., *et al.* “*Inhibited light propagation and broadband reflection in photonic air-sphere crystals.*” Physical Review Letters **83**, 2730-2733 (1999).
- <sup>12</sup> Lopez, J. F. and Vos, W. L. “*Angle-resolved reflectivity of single-domain photonic crystals: Effects of disorder.*” Physical Review E **66** (2002).
- <sup>13</sup> Vlasov, Y. A., Deutsch, M. and Norris, D. J. “*Single-domain spectroscopy of self-assembled photonic crystals.*” Applied Physics Letters **76**, 1627-1629 (2000).
- <sup>14</sup> Vlasov, Y. A., *et al.* “*Existence of a photonic pseudogap for visible light in synthetic opals.*” Physical Review B **55**, 13357-13360 (1997).
- <sup>15</sup> Vlasov, Y. A., Kaliteevski, M. A. and Nikolaev, V. V. “*Different regimes of light localization in a disordered photonic crystal.*” Physical Review B **60**, 1555-1562 (1999).
- <sup>16</sup> Vlasov, Y. A., *et al.* “*Manifestation of intrinsic defects in optical properties of self-organized opal photonic crystals.*” Physical Review E **61**, 5784-5793 (2000).
- <sup>17</sup> Astratov, V. N., *et al.* “*Interplay of order and disorder in the optical properties of opal photonic crystals.*” Physical Review B **66** (2002).

- <sup>18</sup> Photonic band structures were calculated with the “M.I.T. Photonic Bands” (MPB) package available at: <http://ab-initio.mit.edu/mpb/>.
- <sup>19</sup> Datta, S., Chan, C. T., Ho, K. M. and Soukoulis, C. M. “*Effective Dielectric-Constant of Periodic Composite Structures.*” *Physical Review B* **48**, 14936-14943 (1993).
- <sup>20</sup> Bertone, J. F., *et al.* “*Thickness dependence of the optical properties of ordered silica-air and air-polymer photonic crystals.*” *Physical Review Letters* **83**, 300-303 (1999).
- <sup>21</sup> Yannopoulos, V., Stefanou, N. and Modinos, A. “*Effect of stacking faults on the optical properties of inverted opals.*” *Physical Review Letters* **86**, 4811-4814 (2001).
- <sup>22</sup> Wang, Z. L., *et al.* “*Optical properties of inverted opal photonic band gap crystals with stacking disorder.*” *Physical Review E* **67** (2003).
- <sup>23</sup> Inagaki, T., Arakawa, E. T., Hamm, R. N. and Williams, M. W. “*Optical-Properties of Polystyrene from near-Infrared to X-Ray Region and Convergence of Optical Sum-Rules.*” *Physical Review B* **15**, 3243-3253 (1977).
- <sup>24</sup> Kaliteevski, M. A., Martinez, J. M., Cassagne, D. and Albert, J. P. “*Disorder-induced modification of the transmission of light in a two-dimensional photonic crystal.*” *Physical Review B* **66**, art. No.-113101 (2002).
- <sup>25</sup> Koenderink, A. F. and Vos, W. L. “*Light exiting from real photonic band gap crystals is diffuse and strongly directional.*” *Physical Review Letters* **91**, art. No.-213902 (2003).
- <sup>26</sup> Kaliteevski, M. A., Martinez, J. M., Cassagne, D. and Albert, J. P. “*Disorder-induced modification of the attenuation of light in a two-dimensional photonic crystal with complete band gap.*” *Physica Status Solidi a-Applied Research* **195**, 612-617 (2003).
- <sup>27</sup> Lüth, H. “*Solid surfaces, interfaces and thin films*”, Springer-Verlag, Berlin (2001).
- <sup>28</sup> Galisteo-Lopez, J. F., *et al.* “*Experimental evidence of polarization dependence in the optical response of opal-based photonic crystals.*” *Applied Physics Letters* **82**, 4068-4070 (2003).
- <sup>29</sup> van Driel, H. M. and Vos, W. L. “*Multiple Bragg wave coupling in photonic band-gap crystals.*” *Physical Review B* **62**, 9872-9875 (2000).
- <sup>30</sup> Romanov, S. G., *et al.* “*Diffraction of light from thin-film polymethylmethacrylate opaline photonic crystals.*” *Physical Review E* **6305**, art. no.-056603 (2001).
- <sup>31</sup> Galli, M., *et al.* “*Photonic bands and group-velocity dispersion in Si/SiO<sub>2</sub> photonic crystals from white-light interferometry.*” *Physical Review B* **69**, art. no.-115107 (2004).

## CHAPTER 4

---

# Optical properties of artificial opals in the high energy regime

### 1. Introduction

Although artificial opals and related systems have been extensively studied as photonic crystals for nearly a decade now, most experimental studies of their optical response have concentrated on the behavior of the low energy region of the band structure ( $a/\lambda \sim 0.5$ , where  $a$  is the lattice parameter and  $\lambda$  is the wavelength of light in vacuum). In this spectral region the crystal presents a stop band due to Bragg diffraction by the  $\{111\}$  planes and may be treated as a homogeneous medium for the surrounding frequencies (see chapter 3). For energies above this stop band, although some results have been presented for opal based photonic crystals<sup>1-7</sup> most of them have been concerned with identifying the reflectivity peak through which the photonic band gap (PBG) should manifest<sup>1,3-5</sup> in inverse opals with a sufficiently high refractive index contrast. For titania inverse opals<sup>2</sup>, a number of features were observed in reflectivity spectra and successfully accounted for by theoretical calculations, identifying forbidden regions to be the precursor for a PBG. But the interest in this spectral region does not just lie in the existence of stop bands. Spectacular phenomena such as the super prism effect<sup>8</sup> may be observed in artificial opals<sup>9</sup> in frequency intervals where many energy bands overlap and their behavior is radically different from the linear one observed in the surroundings of the L-pseudogap. It is of capital importance then to identify the effect of these bands on the optical response of artificial opals, and investigate whether information about the former may be obtained from the latter. To date, the only results reported on this energy range for artificial opals are those of references 4 (where transmission spectra of silica thin film opals was compared with numerical simulations and with the corresponding band structure of the system, although no interpretation was presented), 6 (transmission spectra were presented for polystyrene (PS) opals, although without comparison with energy bands or any interpretation) and 7 (where reflection and transmission spectra for similar systems were presented and compared with bands in a narrow spectral range, presenting an interpretation which, as will be shown below, was incomplete).

In this chapter we present a detailed study of the optical response of artificial opals along the  $\Gamma L$  direction in reciprocal space for reduced frequencies between  $a/\lambda = 0.9$  and  $a/\lambda = 1.8$ . In this region one would expect the second and third order Bragg diffraction associated with the  $\{111\}$  planes if these were the only to interact with the incident light. As will be seen, the situation is more complex.

Initial optical characterization is performed by means of normal incidence reflection and transmission spectroscopy. In order to ensure that the experimental features we observe come solely from the interaction of electromagnetic radiation with the energy bands of the crystal, a number of issues are taken into account such as dispersion in the refractive index of the spheres, scalability of the features and finite size effects.

Prior to carrying a comparison between the observed features and calculated bands, we investigate on the physical origin of these bands. To do so, the band structure of a crystal possessing a very small refractive index contrast is considered.

Next we take into account the phenomenon of optical diffraction in photonic crystals, taking the description presented in chapter 2 one step further, and unveiling the relation between diffraction and high energy bands.

Finally, making use of all of the above, we are in the situation of interpreting the optical properties which were presented at the beginning of the chapter, in terms of the energy bands of the crystal. We reverse the path followed in section 2, and we vary the optical properties of the samples in order to approach the free photon limit.

## 2. Optical properties: scalability and finite size effects

The main problems encountered when probing the optical properties of artificial opals in the high energy range above the L-pseudogap are related to disorder and multiple Bragg diffraction. In this energy range, the wavelength of the probing light is smaller than the sphere diameter. Therefore the probe beam is likely to be scattered by imperfections in the unit cell which would hardly affect the measurements in the lower energy region. Thus, high quality samples are needed in order to minimize these effects. Also, the band structure for such high frequencies becomes complicated. In the low energy region, for  $a/\lambda < 1$ , the band structure consists of two sets of degenerate bands having a constant slope and being a reminiscence of the effective medium dispersion relation. At the edge of the Brillouin zone a breaking up of the vacuum-like dispersion relation occurs leading to the opening of the L-pseudogap due to Bragg diffraction by  $\{111\}$  planes parallel to the surface. But for higher frequencies the situation becomes more complex. The appearance of bands arising from wave-vectors originally not parallel to the  $\Gamma L$  direction but folded back into it by translational symmetry introduces anticrossings between bands of same energy and symmetry.<sup>10</sup> Also, higher order Bragg diffractions by the  $\{111\}$  planes parallel to the surface are

expected. This complicates the band structure making the comparison between experimental spectra and calculated bands a difficult task. The above can be appreciated in figure 1, where transmission and reflection spectra (collected in the same way as spectra presented in chapter 3) at normal incidence are plotted together with the calculated band structure. For reduced frequencies  $a/\lambda < 1$ , the experimental spectra present a well known behavior consisting of a reflection peak accompanied by a dip in transmission, corresponding to those frequencies contained in the stop band. Out of these frequencies, where the dispersion relation can be approximated to a linear regime, transparency windows in reflection and transmission are found. For the latter, a monotonic decrease in intensity can be appreciated, the origin of which is usually attributed to scattering by several sources of disorder present in the crystal.<sup>11</sup> In the high energy region, for  $a/\lambda > 1$ , a different behavior can be appreciated with a strong decrease in transmission and a number of features both, in transmission and reflection. This new regime coincides with a dramatic change in the band structure of the system, which presents a complicated intermixture of energy bands.

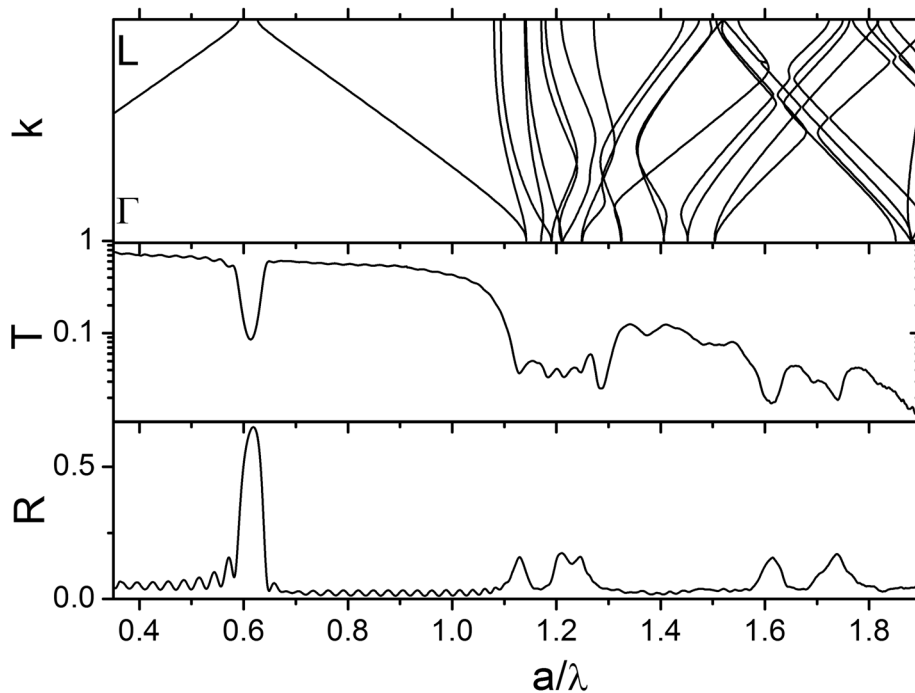


*Figure 1: Band structure calculated along the  $\Gamma L$  direction in reciprocal space for an artificial opal consisting of polystyrene spheres (top). Transmission in a logarithmic scale for an artificial opal 21 layers thick made of spheres 705 nm in diameter (middle). Reflection in a linear scale collected at the same point as transmission (bottom).*

That the above mentioned features originate in the photonic band structure was confirmed by comparing experimental spectra for samples having different sphere

diameters (505, 705 and 1090nm) with the same number of layers and confirming the scalability of the features. Figure 2 shows reflectivity spectra in the high energy region for samples having 505, 705 and 1090 nm diameter spheres. It can be seen that all spectra present identical features, although a small red-shift is present in the spectrum corresponding to the smaller spheres, which increases towards higher energies. This shift can be explained in terms of the PS refractive index dispersion. Bulk PS presents a normal dispersion in this frequency range (400 - 2800 nm),<sup>12</sup> so it can be expected that, as we move towards higher energies, its refractive index will increase more dramatically. It is reasonable then that as the diameter of the spheres decreases, the high energy features will move towards the highly dispersive spectral region, thus presenting an increasing redshift with respect to the ones obtained from larger spheres. Therefore, if we take into account this dispersion in the dielectric constant, together with the fact that PS does not absorb for these frequencies<sup>13</sup> we may conclude that the observed features are caused by interaction of incident light with photonic bands. In order to compare experimental spectra with calculated bands we will use the largest spheres, as the variation in refractive

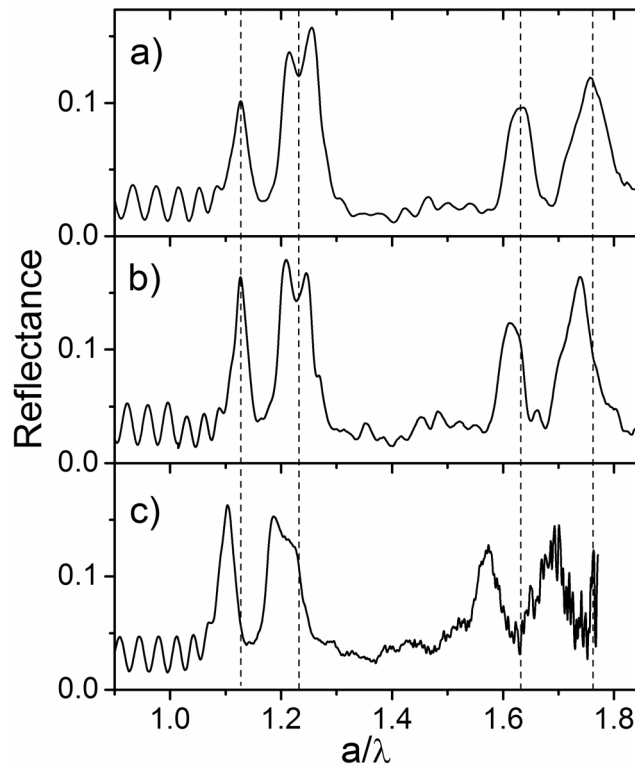


Figure 2: Reflection spectra in the high energy region for samples ~20 layers thick consisting of 1090 (a), 705 (b) and 505 nm (c) spheres. Dashed vertical lines indicate the position of the main optical features of the 1090 nm sample.

index is smallest. If we assume the refractive index of our spheres to be that of bulk PS, in the spectral region where the high energy features are found (between 0.85 and 1.4  $\mu\text{m}$ ) it will vary between 1.569 and 1.576. Since the numeric algorithm employed to calculate energy bands does not allow the introduction of dispersion in the refractive index of the constituent materials, we have chosen a mean value of 1.572.

We have performed a study of the behavior of the optical response of our samples as a function of the number of layers in order to avoid spurious effects associated with the finite size of the samples in subsequent analysis. Figure 3 shows reflectivity spectra for samples fabricated with the 705 nm diameter spheres, for increasing number of layers. For samples 4 layers thick the reflectivity spectra presents a fringe-like pattern similar to that of transparent homogeneous thin films. As the thickness increases to 7 layers and beyond, some optical features are reinforced at the expense of others (Fabry-Perot fringes) and remain for thicker samples: two reflectivity peaks centered around  $a/\lambda = 1.13$  and 1.23, the latter

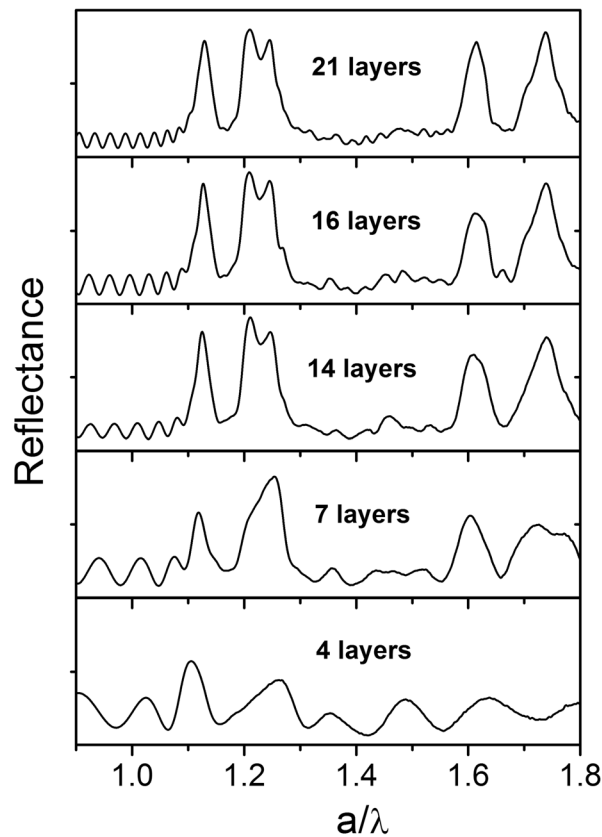


Figure 3: Reflection spectra for samples having an increasing number of layers. Bottom to top: 4, 7, 14, 16 ad 21. Reflection goes from 0 to 20% in all graphs.

presenting two-shoulders, a low reflection region between  $a/\lambda = 1.3$  and  $1.58$ , and two more peaks centered around  $a/\lambda = 1.6$  and  $1.75$ . For samples 14 layers thick, the above mentioned peaks have reached a stationary line shape and spectral position, as well as a reflectance (of about 15%), which will not change for samples as thick as 40 layers (not shown). It is worth noticing that, for an identical system, but in the low energy region, structures consisting of 35 layers were needed to reach this infinite-crystal stationary behavior, avoiding finite size effects (i.e. see chapter 3).

It is also interesting to note that in the low reflection region between the two groups of peaks ( $a/\lambda = 1.3$  and  $1.58$ ) a number of oscillations are present which seem to increase in number and become spectrally narrower and closer. This behavior is what one would expect from a homogeneous transparent material. This issue will be further discussed when a comparison with calculated bands is performed.

### 3. Physical origin of the bands

We now investigate how light interacts with the different bands present in the dispersion relation of the artificial opal. In order to do so, we begin by considering a simple ideal model; that of the photonic crystal with negligible refractive index contrast. We take an FCC arrangement of dielectric spheres with a refractive index  $n_1 = 1.408$ , in a background with  $n_2 = 1.4081$ . The choice for this particular refractive index is justified because it corresponds to the  $n_{eff}$  which may be extracted in the long wave limit for artificial opals consisting of PS spheres (see chapter 3). The band structure for this system, which may be seen as the photonic analogue to the free electron situation in solid states physics,<sup>14</sup> is represented in figure 4. Only the  $\Gamma L$  direction in reciprocal space is shown as it is the one of interest for our particular problem.

Due to the low refractive index contrast we expect this band-structure to be similar to the dispersion relation of a homogeneous medium with refractive index  $n_{eff}$  folded back into the first Brillouin zone due to translational symmetry<sup>10</sup>. We now consider the plane going through the XULK points in reciprocal space as representative for our problem. Figure 5 shows this section of the Brillouin zone in a repeated zone scheme.

Let's consider now an incident beam with a certain frequency  $\omega$  propagating along the  $\Gamma L \Gamma_1$  line in reciprocal space (see figure 5a). If we think of the crystal as a homogeneous medium with refractive index  $n = 1.408$  (which, given the low refractive index contrast of the system should not be such a bad approximation), the dispersion relation for this frequency is given by:

$$\omega = \frac{c}{n} k_i \quad (1)$$

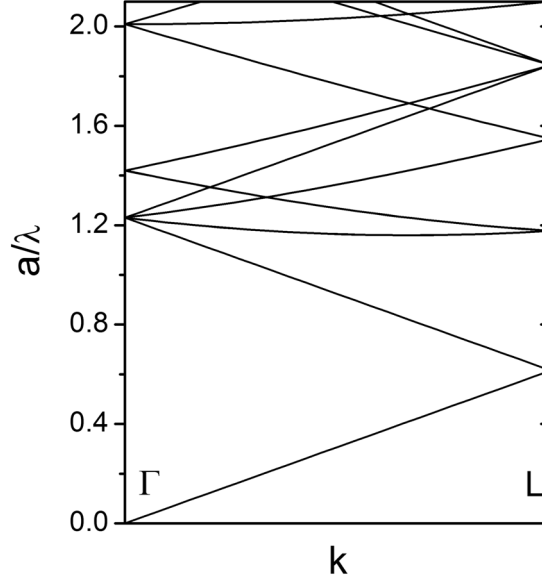


Figure 4: Band-structure for an artificial opal made out of spheres with  $n_1=1.408$  in a background of  $n_2=1.4081$  along the  $\Gamma L$  direction in reciprocal space.

According to Bloch's theorem, applicable to the present problem in virtue of the periodic distribution of the refractive index,<sup>10</sup> we may restrict  $k_i$  to the first Brillouin zone, that is we can fold the dispersion relation given by (1) into this zone:

$$0 \leq k_i \leq \frac{G_{111}}{2} = \frac{\sqrt{3}}{2} \frac{2\pi}{a} \quad (2)$$

We now express (1) in reduced frequency units in order to compare the dispersion relation with the band structure. We do this by dividing both sides by

$$G_{111} = \sqrt{3} \frac{2\pi}{a} :$$

$$\frac{a}{\lambda} = \frac{\sqrt{3}}{n} k_i, \quad 0 \leq k_i \leq 0.5 \quad (3)$$

If we represent (3) together with the band structure depicted in figure 4, we can see (figure 6) how it reproduces some of the bands, namely those consisting of a straight line folded back into the Brillouin zone. These bands can then be taken as the dispersion relation for a wave propagating in a homogeneous medium.

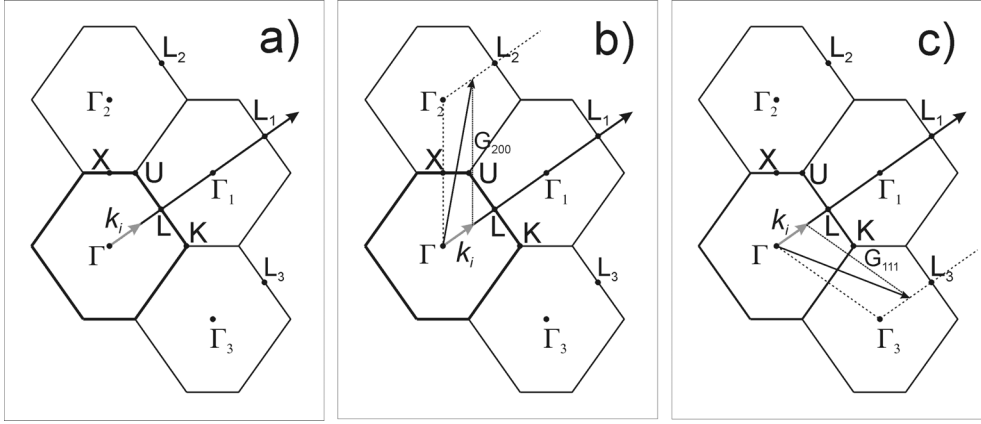


Figure 5: Extended zone scheme along a representative plane of the reciprocal space. (a) Incident wave vector along the  $\Gamma L$  direction. Two wave vectors which are originally not parallel to the  $\Gamma L$  direction, but may be folded back into it through translational symmetry, by subtraction of either a  $G_{111}$  or a  $G_{200}$  reciprocal lattice vector are indicated in (b) and (c).

We must not restrict ourselves to wave vectors  $\mathbf{k}_i$  along the  $\Gamma L$  direction, but also to those which, although originally not parallel to the incident direction considered, may be folded back into it through the translational symmetry of the lattice. We do this for a wave-vector  $\mathbf{k}_i' = \mathbf{k}_i + \mathbf{G}_{200}$ , which can be folded back into the first Brillouin zone by the subtraction of a reciprocal lattice vector  $\mathbf{G}_{200}$  (see figure 5b). The dispersion relation for this wave-vector is given by:

$$\frac{a}{\lambda} = \frac{\sqrt{3}}{n} \left| \sqrt{k_i^2 + \frac{4}{3} + 2 \cos \theta \cdot k_i \frac{2}{\sqrt{3}}} \right|, \quad 0 \leq k_i \leq 0.5 \quad (4)$$

where  $\theta$  is the angle between the  $\Gamma X$  and  $\Gamma L$  directions. We have already expressed it in reduced frequency units in order to compare it with the bands.

We next consider a wave vector  $\mathbf{k}_i'' = \mathbf{k}_i + \mathbf{G}_{111}$  (see figure 5c). In analogy with the previous case, we may express the corresponding dispersion relation as:

$$\frac{a}{\lambda} = \frac{\sqrt{3}}{n} \left| \sqrt{k_i^2 + 1 + 2 \cos \theta \cdot k_i} \right|, \quad 0 \leq k_i \leq 0.5 \quad (5)$$

where  $\theta$  is now the angle between two  $\Gamma L$  segments.

Due to the threefold symmetry of the  $\Gamma L$  direction, identical dispersion relations may be found if one considers the other two equivalent planes. If we now take into account the plane going through the  $\Gamma L W$  points (not shown), it can be demonstrated in an identical manner that another dispersion relation can be drawn for wave vectors which are folded back into the  $\Gamma L$  direction by subtraction of a  $\mathbf{G}_{220}$  vector:

$$\frac{a}{\lambda} = \frac{\sqrt{3}}{n} \left| \sqrt{k_i^2 + \frac{8}{3} + 2 \cos \theta \cdot k_i \sqrt{\frac{8}{3}}} \right|, \quad 0 \leq k_i \leq 0.5 \quad (6)$$

We can now plot those dispersion relations associated with (3)-(6) together with the band structure and find that they totally reproduce it. This is shown in figure 6b.

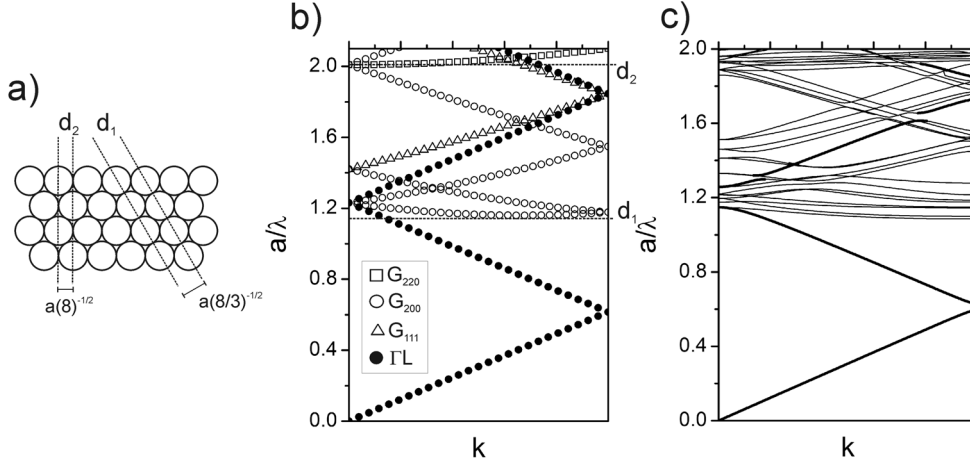


Figure 6: (a) Longest grating periods in the  $\{111\}$  plane of the opal. (b) Band structure for a photonic crystal consisting of spheres with  $n=1.408$  in a dielectric medium with  $n=1.4081$  (lines). Symbols represent dispersion relations for a wave vector parallel to the  $\Gamma L$  direction (filled circles), and wave vectors not parallel to that direction but folded back into it by subtraction of reciprocal lattice vectors  $G_{111}$  (empty triangles),  $G_{200}$  (empty circles) and  $G_{220}$  (empty squares). (c) Band structure for a PS opal. Thick lines represent linear bands.

While the dispersion relation of the wave vector propagating along the  $\Gamma L \Gamma_1$  direction was interpreted as that of a homogenous medium, with refractive index  $n_{eff}$ , it is not clear how we should consider the relation extracted from the situations (4), (5) and (6). To understand the physical origin of these bands we focus on another phenomenon which should be present in our structure due to the existence of a 2D periodicity in each plane of spheres: diffraction. Each of the hexagonal planes stacked along the (111) direction may be viewed as a 2D grating, which will diffract light in directions away from the incident one according to the grating equation:

$$\sin \theta + \sin(\theta_0) = \frac{m \cdot \lambda}{\Lambda \cdot n_{eff}} \quad (7)$$

where  $\theta_0$  and  $\theta$  are the angles of the incident and diffracted beams,  $\lambda$  is the incident wavelength in vacuum,  $\Lambda$  is the grating period,  $m$  is the order of diffraction and  $n_{eff}$  is the effective refractive index. For incidence normal on a plane of spheres, the

lowest frequency for which diffraction will be observed corresponds to the situation in which the diffracted beams are normal to the incident direction:

$$\Lambda \cdot n_{eff} = m \cdot \lambda \quad (8)$$

and to the longest periods present in the grating. From figure 6a, we can see that the two periods we must consider are those denoted as  $d_1$  and  $d_2$ . If we estimate for which frequency (in reduced units) the first order diffraction will take place at each of these gratings, we find the values 1.159 and 2.01 respectively. These values (indicated by horizontal dashed lines in figure 6b) correspond to the lowest frequency for which the higher order bands appear. The behavior of these bands can be further described from the grating equation, so that they account for the dispersion relation of gratings associated to the  $\{111\}$  planes.

It seems then, that photonic bands which are of interest to our situation can be divided into two groups. On the one hand those which can be considered as reminiscent of the effective medium, that is, those associated with a homogeneous medium with a given refractive index (*linear bands* in what follows, indicated by filled circles in figure 6b). On the other, we have those bands which are responsible for diffraction by the stacked hexagonal planes (*diffraction bands* in what follows, indicated by empty symbols in figure 6b). The latter may be considered as the reminiscence of the dispersion relation of the 2D hexagonal grating present at each plane. The overall dispersion relation for this ideal photonic crystal may be then viewed as a superposition of the dispersion relation of a homogeneous medium together with that of a 2D grating.

If we now increase the refractive index contrast present in the photonic crystal we see how the band structure undergoes a number of changes with respect to the situation of null refractive index contrast. This can be seen in figure 6c, where the band structure for an artificial opal of PS spheres is shown. First, one can see that the dispersion relation of linear bands (marked as thick lines in figure 6c) splits at the edges and centre of the Brillouin zone as a consequence of Bragg diffraction by the  $\{111\}$  family of planes. These bands also split as a consequence of anticrossings with the diffraction bands, for which degeneracies are lifted.

#### 4. Diffraction in photonic crystals

We now proceed to study the propagation of light through the crystal as we approach the high energy region. We do this by visual inspection of monochromatic light transmitted and reflected at normal incidence by our samples. The light sources were a tunable nanosecond Optical Parametric Oscillator whose emission could be tuned within 450 and 670 nm, and an argon laser. Samples made of 505 and 705 nm PS spheres and 335 nm poly(methyl methacrylate) (PMMA)<sup>15</sup> spheres were used, to place their high energy bands in this spectral region. Sample thickness was in the 20-30 layers range. Figure 8 shows photographs of the samples under illumination. The experimental configuration is different from that

used for optical diffraction experiments in chapter 2. Now the beam passes through a perforated screen, impinges on the glass substrate and then hits the sample at normal incidence. The photograph is taken in transmission (see figure 7a).

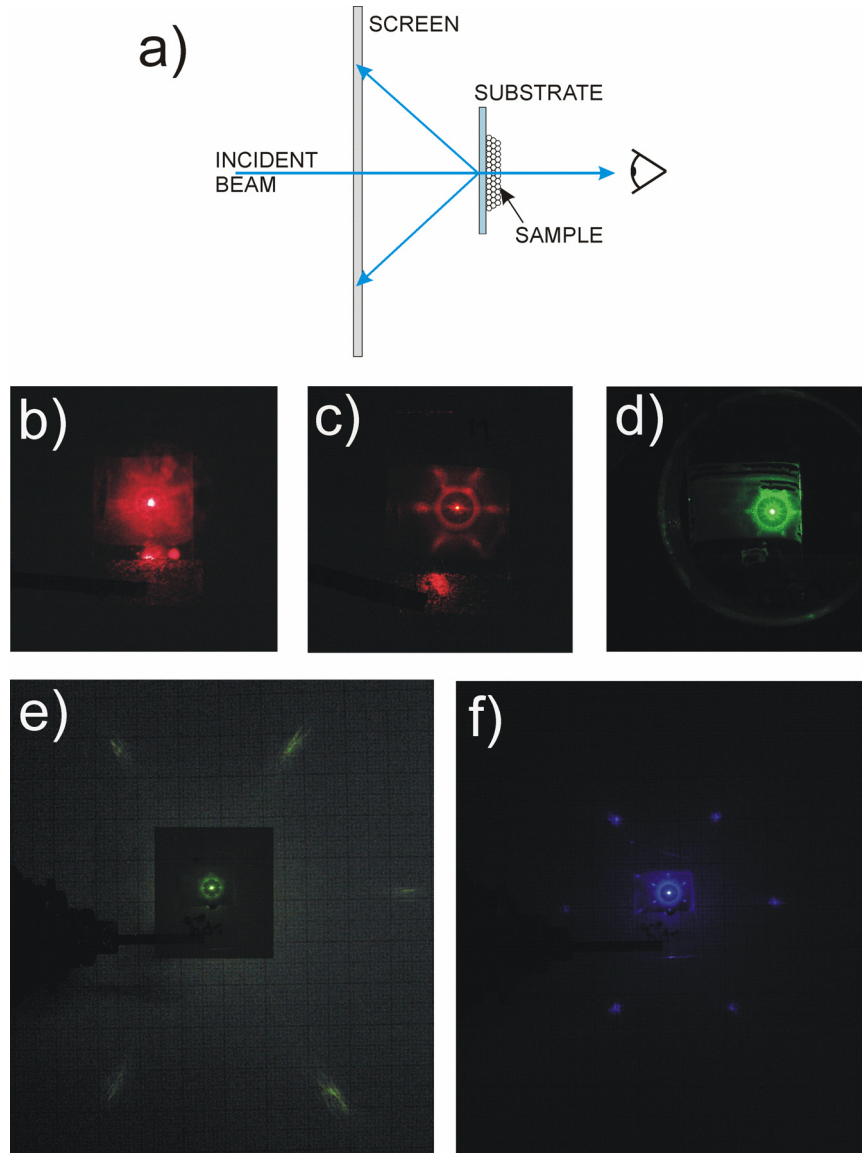


Figure 7: Diagram of the diffraction set-up (a). Photographs taken in transmission for samples consisting of 505 nm spheres with  $\lambda = 670$  nm ( $a/\lambda = 1.07$ ),  $\lambda = 650$  nm ( $a/\lambda = 1.1$ ) and  $\lambda = 560$  nm ( $a/\lambda = 1.28$ ) (b-d respectively). Photographs for samples of 705 nm spheres with  $\lambda = 570$  nm ( $a/\lambda = 1.75$ ) and  $\lambda = 470$  nm ( $a/\lambda = 2.1$ ) (e-f respectively).

For samples of 505 nm PS spheres and reduced frequencies  $a/\lambda < 1.085$ , we observe that the transmitted light consists of a beam parallel to the incident one surrounded by a diffuse halo (figure 7b). In this spectral range light can only couple to linear bands and therefore propagates in the forward direction. Part of the diffuse light generated as a consequence of structural disorder exits the substrate, and part suffers total internal reflection (TIR) at the substrate-air interface and is projected back on the sample which acts as a screen, a halo forming on it.

As we reach  $a/\lambda \sim 1.09$ , a hexagonal diffraction pattern appears projected onto the sample (figure 7c). The diffracted beams exit the sample in directions other than the incident one and are internally reflected at the substrate-air interface. The diffraction spots appear far from the incident beam, which corresponds to propagation at nearly grazing angle. This phenomenon coincides with the sixth band which spans the frequency region  $1.085 < a/\lambda < 1.18$  for these samples, and is a diffraction band as mentioned in the previous section. The fifth band is not considered as it can not be coupled to by the incident beam due to symmetry reasons.<sup>16</sup>

As the frequency is increased, the diffraction pattern closes itself towards the incident beam in agreement with the behavior of the diffracted beam from a grating (figure 7d). As we reach  $a/\lambda \sim 1.6$  the diffracted beams exit the diffuse halo and leave the glass, being projected onto the screen placed before it (figure 7f). An identical pattern is projected in transmission (not shown).

For a sufficiently high energy ( $a/\lambda \sim 1.9$ ) the former diffraction pattern is still projected onto the screen and a new one, rotated  $30^\circ$  with respect to it, is projected onto the sample as a consequence of TIR at the glass-air interface (figure 7g) as assumed with the former one. This coincides with the energy range where the bands reminiscent of the second family of grating bands appear. That is, those bands arising from the folding of wave vectors by subtraction of  $\mathbf{G}_{220}$  vectors.

The condition for observing diffraction patterns is therefore twofold<sup>17</sup>. On the one hand, there must be a diffraction band to which incident light may couple. On the other hand, the external medium must allow for the conservation of the parallel component of the diffracted wave vector. This can be understood as follows; according to figure 5, the component parallel to the crystal surface of any of the two diffracted wave vectors is  $(k_{//})^d = G_{hkl} \sin \theta$ , where  $G_{hkl}$  is the modulus of the reciprocal lattice vector added, and  $\theta$  is the angle between the incident beam (that is the  $\Gamma L$  direction) and  $G_{hkl}$ . For both situations in figures 5b and 5c, it can be shown that:

$$(k_{//})^d = \frac{2\pi}{a} \sqrt{\frac{8}{3}} \quad (9)$$

According to figure 8, the diffracted beam will only be observed if the following condition is satisfied:

$$\frac{2\pi}{\lambda} n_0 \geq (k_{//})^d \rightarrow \frac{a}{\lambda} \geq \sqrt{\frac{8}{3}} \frac{1}{n_0} \quad (10)$$

(where  $n_0$  is the refractive index of the external medium) and the external angle of the diffracted wave vector is given by:

$$\frac{2\pi}{\lambda} n_0 \sin \theta = (k_{\parallel})^d \rightarrow \frac{a}{\lambda} \sin \theta = \sqrt{\frac{8}{3}} \frac{1}{n_0} \quad (11)$$

that is, the one predicted by the grating equation as previously reported.<sup>18-20</sup> In our system, condition (10) is reduced to  $a/\lambda \geq 1.633/n_0$  which explains why the first set of diffraction spots is first projected on the sample itself, since it first exits into the glass ( $n_0 = 1.51$ ) for  $a/\lambda \geq 1.08$ , and suffers TIR at the glass-air interface. Then it is projected on the screen for  $a/\lambda \geq 1.633$ . For this reduced frequency TIR is overcome at the glass-air interface and the parallel component of the wave vector is conserved at the sample-air interface.

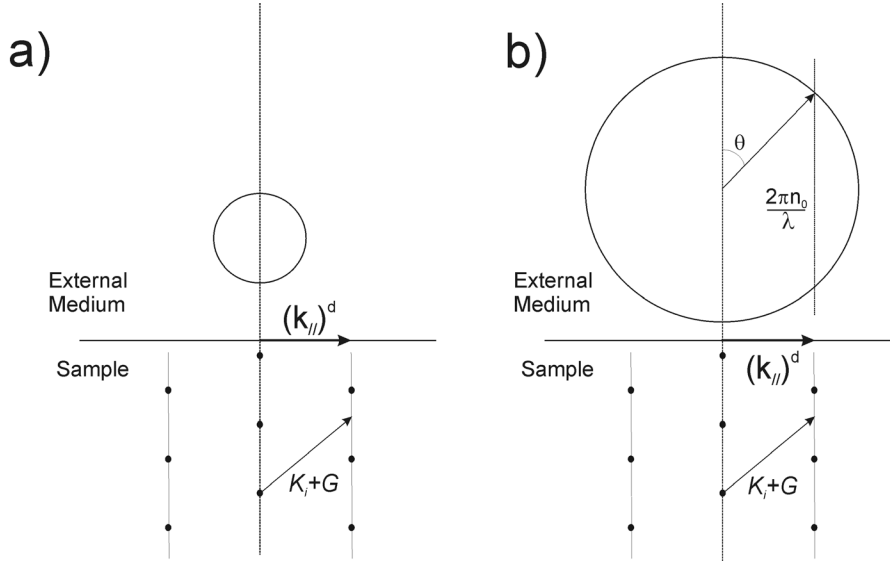


Figure 8: Conservation of the component of the diffracted wave vector parallel to the sample surface;  $(k_{\parallel})^d$ . The circumference indicates the allowed wave vectors in the external medium and has a radius  $k_{out} = 2\pi n_0/\lambda$ . (a) Refractive index of external medium is too small to allow for the conservation. (b) Refractive index of external medium is large enough.

But it may happen that bands determining the onset of diffraction for a certain direction have not absolute minima but saddle points along the  $\Gamma L$  direction.<sup>17</sup> In that case, the condition for the onset of diffraction may have to be looked for elsewhere, and diffraction patterns may appear for lower energies if we deviate from that direction. This is what happens for the  $\Gamma L$  direction of an FCC lattice. We demonstrate this by using an opal of PMMA spheres, for which the first diffraction band appears at  $a/\lambda = 1.14$  for normal incidence. If we illuminate it with  $\lambda = 476$  nm ( $a/\lambda = 1$ ) we find that no diffraction pattern may be observed at normal incidence. As we tilt the sample so that its normal makes an angle of  $\sim 10^\circ$  with respect to the incident beam, a pattern appears projected onto the sample. Figures

9a and 9b show the diffraction patterns observed as we tilt the sample  $30^\circ$  along the LU(K) and LW directions in reciprocal space.<sup>21</sup> Figure 9c shows the minimum of the first diffraction band as a function of the external angle of incidence, extracted from the band structure. This is calculated for the above mentioned directions in reciprocal space. Together, as a dashed line, appears the grating equation for the same angular range, indicating the condition for the conservation of the parallel component of the wave vector.<sup>22</sup>

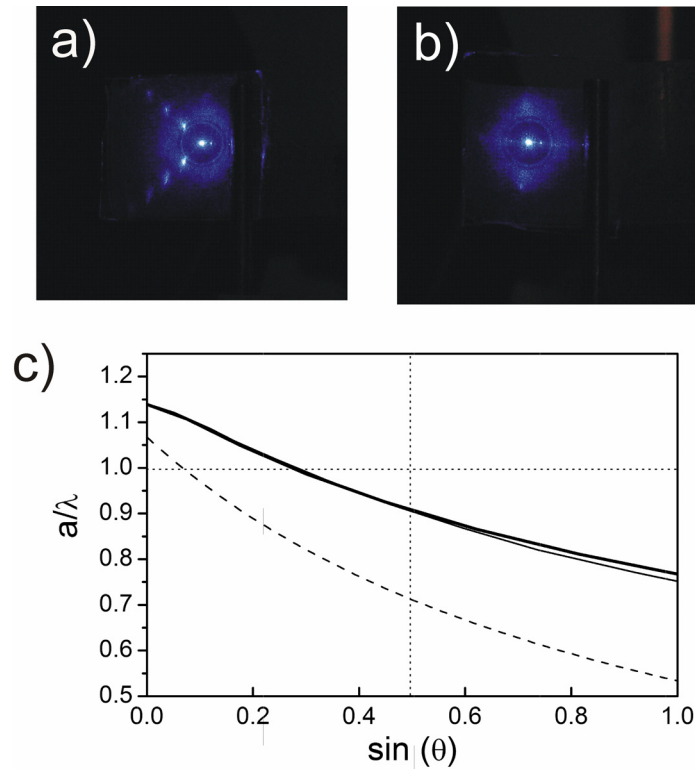


Figure 9: Diffraction pattern projected on a PMMA sample for a reduced frequency  $a/\lambda=1$  as the sample is tilted  $30^\circ$  along the LW (a) and LU/K (b) directions. Minimum of the first diffraction band along the LW (thick line) and LU/K (thin line) directions, together with the condition given by the grating equation (dashed line) are represented in (c).

## 5. Comparison with band structure

We next proceed to interpret the optical response of the samples. In order to do so we first use a 50 layer thick sample made of the largest spheres (1090 nm) and compare its reflection and transmission spectra with calculated bands. For these samples, the high energy features fall in the spectral range 1400-850 nm. If we assume the refractive index of bulk PS for the spheres, we must consider the

interval  $1.569 < n < 1.576$ . For comparison we employ an average value of 1.572. This comparison is shown in figure 10, where the linear bands are represented as thick lines, and the diffraction bands as thin ones.

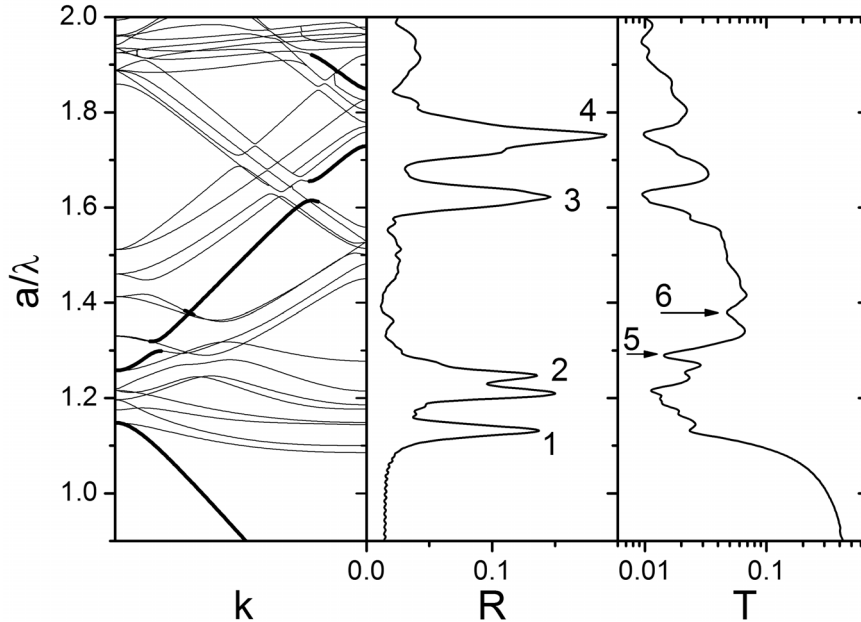
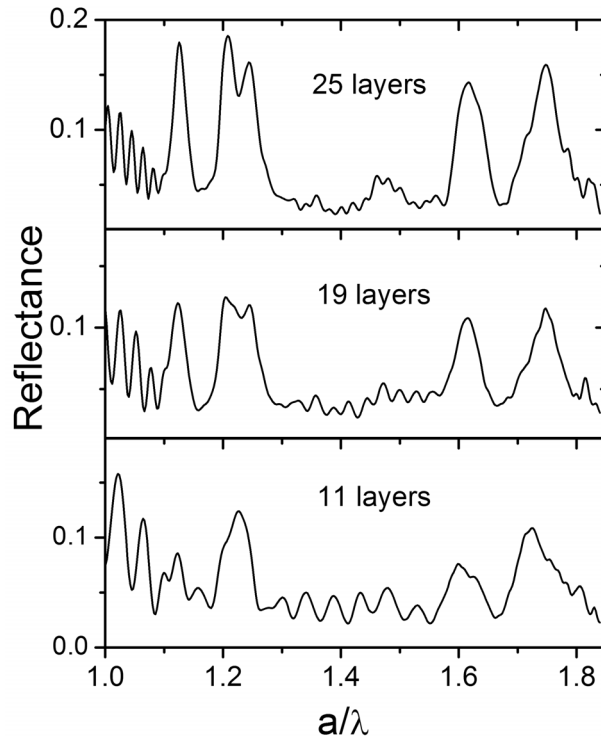


Figure 10: (a) Band structure along the  $\Gamma L$  direction in reciprocal space for an artificial opal made of PS spheres ( $n=1.572$ ). Linear bands are indicated as thick lines. (b) Reflectance and (c) transmittance for a 50 layers thick sample.

The transmitted intensity presents an abrupt decrease in the spectral range for which the first diffraction band appears. This is to be expected, since part of the incident intensity is diffracted and cannot be collected. The shape of this decrease is clearly different from that associated with disorder, as can be seen in figure 1. We see how the reflectivity peaks at  $a/\lambda = 1.13$  and  $1.23$  (peaks 1 and 2 hereafter) are accompanied by a region of low transmission. Peak 1 appears in a region where the low energy linear bands coexist with diffraction bands presenting a very small slope. The nature of this peak is clearly different from that of the Bragg peak ( $a/\lambda = 0.61$ ) since in the latter, no states were available at the corresponding frequency. The effect of uncoupled modes, which cannot be excited by external light for symmetry reasons, can also be ruled out since, for these frequencies, uncoupled modes always coexist with allowed ones.<sup>16</sup> A plausible explanation for this behavior could be the coupling of light to diffraction bands presenting a low dispersion.<sup>7</sup> It has been predicted<sup>10</sup> that in the frequency region where such flat bands are found, the PC behaves (in terms of its normal incidence optical response) as an effective medium with a large refractive index, and correspondingly presents a high/low reflectance/transmittance. Peak 2, which presents two shoulders, corresponds to the region of the band structure where the  $\Gamma L$  bands split at the

center of the Brillouin zone at frequencies where the second order Bragg diffraction would be expected to take place. Contrary to the splitting caused by the first order Bragg diffraction, here the gap is filled with photonic states. As for peak 1, these states correspond to flat diffraction bands, and therefore the origin of the reflection/transmission could be due to an effective medium behavior with a large refractive index.



*Figure 11: Reflectance spectra of samples consisting of 1090 nm spheres having different thickness. Top to bottom: 11, 19 and 25 layers.*

In the frequency window between  $a/\lambda = 1.3$  and  $1.58$ , the low reflectance is accompanied by a recovery of the transmission. If we observe this region as a function of the number of layers in figure 3, we can appreciate that reflectivity spectra appear as a set of fringes whose number increases with the thickness of the sample, indicating an effective refractive index medium behavior. This frequency interval corresponds to a region where linear bands coexist with a number of diffraction bands having a different slope. This behavior can be better appreciated if we consider samples grown on silicon substrates where secondary oscillations are more pronounced due to the high reflectance of the substrate itself. Figure 11 shows reflectivity spectra for samples made of 1090 nm spheres and having different thickness. Secondary oscillations appear evenly spaced, and an effective refractive index may be extracted from them. We calculate the number of layers from the secondary oscillations in the low energy region below the pseudogap and

then we extract an effective refractive index  $n_{eff}$  from the high energy region oscillations. For a number of samples having different thickness (between 10 and 30) we obtain  $n_{eff} = 1.68 \pm 0.05$ . We can now calculate an effective refractive index from the linear bands in that spectral region. We use bands calculated for dielectric spheres of  $n = 1.572$ , which is the refractive index of bulk polystyrene in the spectral region where these oscillations appear for 1090 nm spheres. We obtain  $n_{eff} = 1.64$ , higher than the value obtained from the low energy bands (1.41), and in accordance with the experimental result.

The two reflectivity peaks appearing at higher frequencies for  $a/\lambda = 1.62$  and 1.75, (peaks 3 and 4 hereafter), find corresponding transmission dips in a spectral region where the linear bands undergo an anticrossing and a splitting at the edge of the Brillouin zone respectively. The experimental features seem to be slightly redshifted with respect to the calculated ones, which are centered at  $a/\lambda = 1.63$  and 1.78. The effect of band anticrossing on the optical properties of opal-based photonic crystals has been previously reported.<sup>23-25</sup> However, these studies were performed in a spectral region where few bands were present and the band repulsion involved the existence of stop bands. In the present case the situation is more complicated as the anticrossing region is filled with states distributed over several bands. A similar situation is found in the region with the splitting, which takes place for frequencies where the third order Bragg diffraction by the {111} planes would be expected. Therefore the incident light may only couple to diffraction bands. It is likely then that if not all light couples to these bands, reflectance and transmittance peaks are expected. In order to account for the exact line shapes, spectral position and intensities of these features, one would require knowing the exact coupling strength between the incident light and each band,<sup>9</sup> a task demanding a vast amount of calculation time. A similar analysis would be required for peaks 1 and 2.

Turning to transmission spectra, we point out the existence of two dips appearing at  $a/\lambda = 1.29$  and 1.38, less intense than the previous ones, and which cannot be appreciated in the reflection spectra. They are pointed out by arrows in figure 10. Again, these dips are found in a spectral region where two anticrossings take place at  $a/\lambda = 1.31$  and 1.38 in the calculated linear bands. The attenuation of the former dip is larger than that of the latter, which agrees with the width of the corresponding anticrossings. These two dips will be referred to as peak 5 and 6 in subsequent analysis.

A gradual transformation of the system towards a homogeneous material that allowed comparing it with a free photon model would lend itself useful in gaining further understanding of the above features. In order to tune the optical response in a continuous fashion we had recourse to gradually infiltrating the structures with silica. This changes the average refractive index and, which is more important, it reduces the refractive index contrast approaching the composite to a nearly homogeneous medium, providing a number of different topographies and band structures for comparison. Since the refractive index of silica is lower than that of polystyrene the index matching condition is not fully met. The infiltration process<sup>26</sup>

(see appendix 2) takes place at room temperature so that the polystyrene skeleton is not perturbed. Further, the silica growth takes place in a laminar way around the spheres, yielding samples whose band structure may be easily modeled provided the refractive index of both constituents is known.<sup>b</sup> In this way we have filled samples 50 layers thick with pore fillings varying between 4% and 70% (close to the theoretical maximum filling of 86%<sup>23</sup>). The filling fraction was controlled through the comparison of the spectral position of the centre of the Bragg peak with the centre of the L-gap in the calculated band structure, the former being the parameter less affected by finite size effects, which are expected to become more pronounced as we decrease the refractive index contrast. The infiltration, performed for the samples made of 1090 nm spheres, could not be carried further due to the fact that the Bragg peak for this sphere diameter falls close ( $\lambda = 2.5 \mu\text{m}$ ) to the spectral region where the first silanol absorption band appears ( $\lambda = 2.67 \mu\text{m}$ ).<sup>27</sup> Infiltrations performed on samples with smaller spheres showed that the observed tendency in this spectral range continues up to fillings of 80%.<sup>28</sup>

Figure 12 shows the evolution of the optical response in reflection of our system as we increase the pore filling fraction, reducing the contrast and increasing the

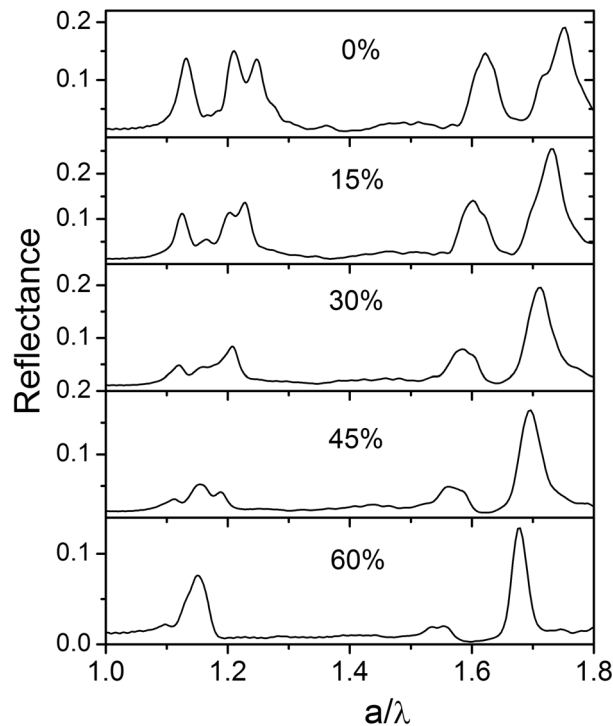


Figure 12: Reflectance spectra of samples consisting of 1090 nm spheres having an increasing fraction of its pores filled with  $\text{SiO}_2$ .

<sup>b</sup> The refractive index of the grown silica was measured by means of variable angle spectroscopic ellipsometry and found to be  $1.442 < n < 1.447$  in the spectral range of interest.

average refractive index. All peaks shift to lower frequencies, owing to an increase in the average refractive index of the structure and, in general, present a decrease in intensity and spectral width due to the reduction of contrast. In the spectral region where peaks 1 and 2 are located, for low filling fractions (<25%) we observe how four peaks instead of three become visible. As the filling is increased, these peaks become closer and merge until reaching a situation where only two peaks may be observed (60% filling). In this range, as already mentioned, the band structure presents four flat dispersion bands which become closer and even degenerate for high fillings, as seen in the band structures of figure 13. In this figure it can be appreciated that this behavior finds correspondence in transmission. Peaks 3 and 4 also become spectrally narrower and less intense, the former presenting a more pronounced decrease in intensity. Transmission dips also reproduce this evolution (see figure 13).

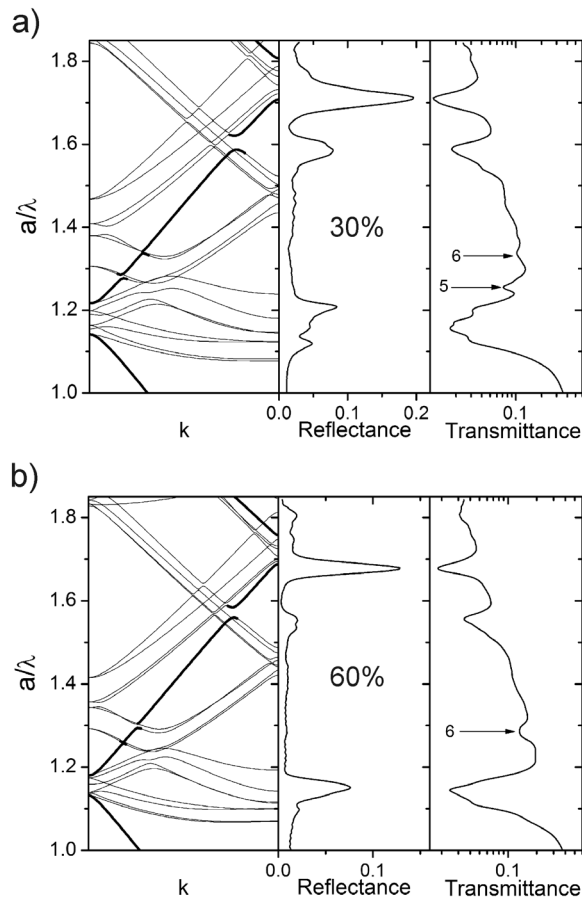


Figure 13: Calculated band structure (left), experimental reflectance (middle) and transmittance (right) for two samples having 30% (a) and 60% (b) of the pore filled with  $\text{SiO}_2$ . Peaks are labeled according to the text.

In transmission spectra we can also observe the two dips (5 and 6 in figure 10) associated with the anticrossings taking place in the calculated bands near the centre of the Brillouin zone for  $a/\lambda = 1.29$  and  $1.38$  in the case of the bare opal. The strength of the interaction leading to the avoided crossing is determined by the scattering strength (refractive index contrast) narrowing and almost closing some of these gaps for high infiltration degrees. For a pore filling of 30% both of them are still present, but for 60% only the high energy one is sizable enough to produce an attenuation band. The lower energy one, narrower due to weakly interacting bands disappears as soon as the contrast is reduced. The anticrossing occurring close to the edge of the Brillouin zone at  $a/\lambda = 1.62$  for bare opals (peak 3) remains even for the highest degrees of infiltration evincing strongly interacting bands.

Finally we compare the evolution of the experimental features with the calculated ones as the pore filling fraction is increased (figure 14). For peaks 3 and 4, which we associate to splitting and anticrossings of the linear bands we have considered the center frequency as representative. For peaks 1 and 2, appearing where flat diffraction bands are in the band structure, we have considered the reduced frequency for which a maximum in intensity takes place, as the merging of the peaks hampers defining a central frequency. From the band structure we have extracted the high and low edges of splitting and anticrossings of linear bands (defining grey bands in figure 14), as well as the frequency for which the first diffraction band becomes dispersionless close to the edge of the Brillouin zone (grey line in figure 14). We can see how experimental results follow the same trend

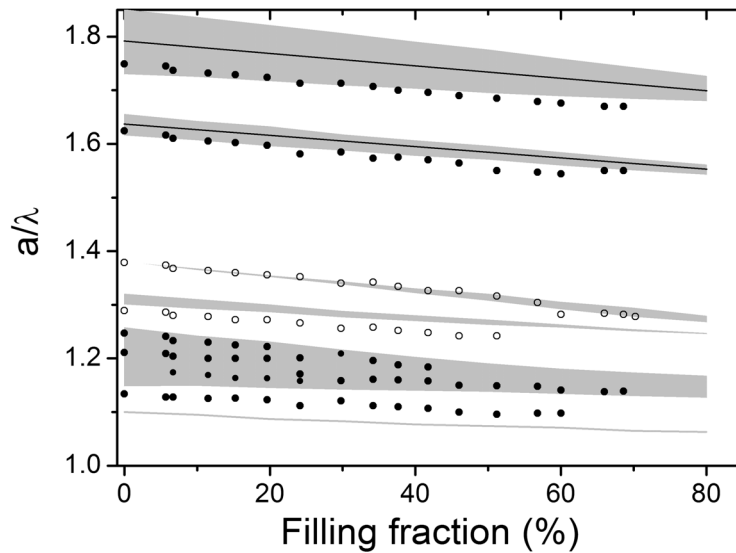


Figure 14: Evolution of the spectral position of band anticrossing, splitting at the edges and centre of the Brillouin zone and dispersionless bands. Open/closed symbols correspond to experimental data taken from transmission/reflection spectra. Lines/grey bands correspond to center/width of gaps and anticrossings extracted from theory.

as calculated ones for an increasing pore filling fraction. For peaks 3-6 this includes a redshift together with a spectral narrowing of the experimental features. The coincidence is satisfactory for all features although it can be appreciated that for those appearing at higher frequencies a marked redshift is still present in the experimental values.

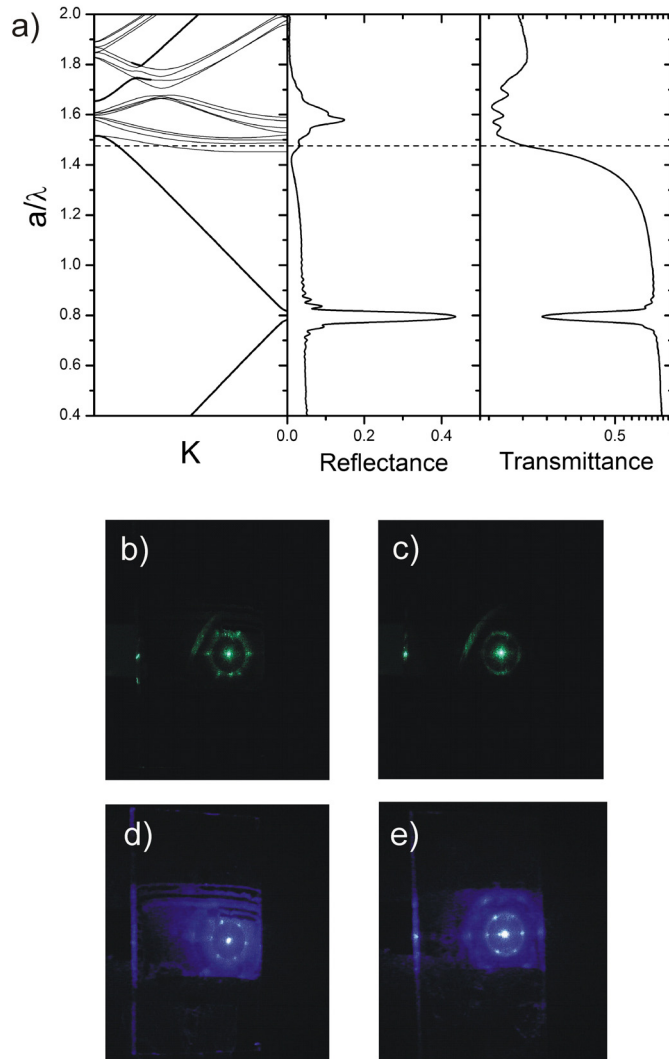


Figure 15: Calculated band structure (left), reflectance (middle) and transmittance (right) for a  $\text{SiO}_2$  inverse opal with 70% of the pore filled (a). Diffraction patterns projected on the opal and its  $\text{SiO}_2$  replica (70% filling fraction) for reduced frequencies  $a/\lambda = 1.42$  (b, c) and  $a/\lambda = 1.56$  (d, e).

Although only hexagonal diffraction patterns were reported in section 4, triangular ones were observed for the composite systems. This fact is in agreement with observations of thin samples and thick samples filled with ethanol (see chapter 2 and reference 19) and agrees with predictions of a single scattering model (SSM) for FCC crystals.<sup>18</sup> The reason why a transition from C6 to C3 symmetry patterns is observed as we lower the refractive index contrast remains a challenging question at this point. Since SSM predictions are expected to break down for systems with a high refractive index contrast such as bare opals, such a study may require the calculation of the coupling coefficients for bands responsible for diffraction along with its mode structure.

We can take the study one step further by eliminating the PS skeleton, leaving a SiO<sub>2</sub> inverse replica of the original structure. This was performed by means of calcination at 450° C.<sup>29</sup> By doing this we lower the average refractive index of the structure, but increase its contrast with respect to the composite system. The optical response and the band structure blue shift accordingly, as can be appreciated in figure 15a, where the optical response for a sample made out of 505 nm spheres with 70% of its pore filled is shown. Here it can be seen that the abrupt drop in transmittance blue shifts with the first set of diffraction bands. In the same spectral region we observe peaks in reflection, reminiscent of peaks 1 and 2 in the bare opal, which present a complicated line shape if compared with the two peaks seen in the composite system.

By doing this we also shift to higher energies the onset of diffraction. Figures 15b and 15c show that for a reduced frequency  $a/\lambda = 1.42$ , where Bloch modes associated with diffraction are only available in the bare opal system, diffraction patterns may only be observed in that system. As we raise the frequency to  $a/\lambda \sim 1.49$ , we are in a situation where diffraction bands are available for both systems and diffraction patterns may be observed. Figures 15d and 15e show diffraction patterns projected on the sample itself for direct and inverse structures and a reduced frequency of  $a/\lambda = 1.56$ .

## 6. Conclusions and future work

In this chapter a first approach to understand the effect of high energy bands on the optical response of artificial opals has been presented. Experimental features in reflectance and transmittance spectra, which are demonstrated to be scalable with sphere size and independent of sample thickness, have been compared with calculated bands.

The relationship between bands originated by folding of wave vectors originally not parallel to the incident direction and diffraction patterns has been established. Further, the effect of these patterns on the transmission spectra has been identified with an abrupt decrease in intensity which was not understood. The remaining features in transmission and reflection spectra are likely a combination of gaps and anticrossings present in linear bands, associated with wave vectors

parallel to the incident direction, and diffraction bands. To properly understand the intensities and line shapes of the observed features, a detailed study of the coupling coefficients of the incident beam with available bands (along with its mode structure) for each fixed frequency is required. By doing this, a better insight could be gained into the transition from C6 to C3 symmetry patterns observed as we lower the refractive index contrast of the samples.

In order to extract more detailed information on the effect of individual bands it would be desirable to isolate them from each other. Recent developments in band engineering by means of infiltration with high refractive index semiconductors such as silicon or germanium may be a useful tool.<sup>30</sup> A major drawback of the present system (i.e. PS artificial opals) is its low resistance to the high temperatures needed to infiltrate them with these semiconductors by means of chemical vapor deposition (CVD). This technique is ideal for a controlled infiltration, and the morphology of the samples may be modeled with available calculation methods. Therefore further developments in the growth of similar samples with silica spheres are needed.

## 7. References

---

- <sup>1</sup> Blanco, A., *et al.* "Large-scale synthesis of a silicon photonic crystal with a complete three-dimensional bandgap near 1.5 micrometres." *Nature* **405**, 437-440 (2000).
- <sup>2</sup> Vos, W. L. and van Driel, H. M. "Higher order Bragg diffraction by strongly photonic fcc crystals: onset of a photonic bandgap." *Physics Letters A* **272**, 101-106 (2000).
- <sup>3</sup> Miguez, H., *et al.* "Germanium FCC structure from a colloidal crystal template." *Langmuir* **16**, 4405-4408 (2000).
- <sup>4</sup> Vlasov, Y. A., Bo, X. Z., Sturm, J. C. and Norris, D. J. "On-chip natural assembly of silicon photonic bandgap crystals." *Nature* **414**, 289-293 (2001).
- <sup>5</sup> Juarez, B. H., Ibisate, M., Palacios, J. M. and Lopez, C. "High-energy photonic bandgap in  $Sb_2S_3$  inverse opals by sulfidation processing." *Advanced Materials* **15**, 319-323 (2003).
- <sup>6</sup> Wostyn, K., *et al.* "Optical properties and orientation of arrays of polystyrene spheres deposited using convective self-assembly." *Journal of Chemical Physics* **118**, 10752-10757 (2003).
- <sup>7</sup> Miguez, H., Kitaev, V. and Ozin, G. A. "Band spectroscopy of colloidal photonic crystal films." *Applied Physics Letters* **84**, 1239-1241 (2004).
- <sup>8</sup> Kosaka, H., *et al.* "Superprism phenomena in photonic crystals." *Physical Review B* **58**, 10096-10099 (1998).
- <sup>9</sup> Ochiai, T. and Sanchez-Dehesa, J. "Superprism effect in opal-based photonic crystals." *Physical Review B* **64**, art. no.-245113 (2001).
- <sup>10</sup> Sakoda, K. "Optical properties of photonic crystals", Springer-Verlag, Berlin (2001).
- <sup>11</sup> Vlasov, Y. A., *et al.* "Existence of a photonic pseudogap for visible light in synthetic opals." *Physical Review B* **55**, 13357-13360 (1997).
- <sup>12</sup> Sultanova, N. G., Nikolov, I. D. and Ivanov, C. D. "Measuring the refractometric characteristics of optical plastics." *Optical and Quantum Electronics* **35**, 21-34 (2003).
- <sup>13</sup> Inagaki, T., Arakawa, E. T., Hamm, R. N. and Williams, M. W. "Optical-Properties of Polystyrene from near-Infrared to X-Ray Region and Convergence of Optical Sum-Rules." *Physical Review B* **15**, 3243-3253 (1977).
- <sup>14</sup> Ashcroft, N. W. and Mermim, N. D. "Solid State Physics", Saunders College Publishing, Philadelphia (1976).
- <sup>15</sup> PMMA samples were grown by Dr. D. Golmayo in similar conditions to the polystyrene ones presented in chapter 2. They have a similar band structure to that of polystyrene ones since their refractive index in this spectral region is close: 1.51.
- <sup>16</sup> Lopez-Tejeira, F., Ochiai, T., Sakoda, K. and Sanchez-Dehesa, J. "Symmetry characterization of eigenstates in opal-based photonic crystals." *Physical Review B* **65**, art. no.-195110 (2002).

## References

---

- <sup>17</sup> García-Santamaría, F., Galisteo-López, J. F., Braun, P. V., and López C., “*Optical diffraction and high-energy features in 3D photonic crystals*” *Physical Review B* (in press) (2005)
- <sup>18</sup> Amos, R. M., *et al.* “*Fabrication of large-area face-centered-cubic hard-sphere colloidal crystals by shear alignment.*” *Physical Review E* **61**, 2929-2935 (2000).
- <sup>19</sup> Goldenberg, L. M., *et al.* “*Optical properties of ordered arrays of large latex particles.*” *Physica E-Low-Dimensional Systems & Nanostructures* **17**, 433-435 (2003).
- <sup>20</sup> Kanai, T., Sawada, T. and Kitamura, K. “*Optical determination of the lattice constants of colloidal crystals without use of the refractive index.*” *Langmuir* **19**, 1984-1986 (2003).
- <sup>21</sup> The orientation of the sample was performed according to the discussion of chapter 3.
- <sup>22</sup> This data was extracted by Dr. F. García-Santamaría from band structure calculations.
- <sup>23</sup> van Driel, H. M. and Vos, W. L. “*Multiple Bragg wave coupling in photonic band-gap crystals.*” *Physical Review B* **62**, 9872-9875 (2000).
- <sup>24</sup> Romanov, S. G., *et al.* “*Diffraction of light from thin-film polymethylmethacrylate opaline photonic crystals.*” *Physical Review E* **6305**, art. no.-056603 (2001).
- <sup>25</sup> Galisteo-Lopez, J. F., Palacios-Lidon, E., Castillo-Martinez, E. and Lopez, C. “*Optical study of the pseudogap in thickness and orientation controlled artificial opals.*” *Physical Review B* **68**, art. no.-115109 (2003).
- <sup>26</sup> Miguez, H., *et al.* “*Mechanical stability enhancement by pore size and connectivity control in colloidal crystals by layer-by-layer growth of oxide.*” *Chemical Communications*, 2736-2737 (2002).
- <sup>27</sup> Miguez, H. “*Los ópalos artificiales como cristales fotónicos*”, PhD Thesis, Universidad Autónoma de Madrid (2000).
- <sup>28</sup> Galisteo-Lopez, J. F. and Lopez, C. “*High-energy optical response of artificial opals.*” *Physical Review B* **70**, art. no.-035108 (2004).
- <sup>29</sup> Palacios-Lidon, E., Galisteo-Lopez, J. F., Juarez, B. H. and Lopez, C. “*Engineered planar defects embedded in opals.*” *Advanced Materials* **16**, 341-345 (2004).
- <sup>30</sup> Garcia-Santamaria, F., *et al.* “*Photonic band engineering in opals by growth of Si/Ge multilayer shells.*” *Advanced Materials* **15**, 788-790 (2003).



## CHAPTER 5

---

# White light interferometry of thin film opals

### 1. Introduction

Reflection and transmission spectroscopy are nowadays the most widespread techniques for the optical characterization of three dimensional (3D) photonic crystals. They are usually employed to detect the existence of forbidden spectral intervals. These appear as regions of low (high) transmission (reflection), indicating the exponential attenuation of electromagnetic radiation as it propagates through the crystal (see chapter 3). A comparison with calculated bands is mandatory when employing these techniques in order to avoid the effects of uncoupled modes.<sup>1</sup> One major drawback of these techniques is that they usually fail to provide information on the dispersion of the bands and knowledge is gained only on the existence of energy gaps. Vlasov and co-workers<sup>2</sup> reported on spectroscopic reflection measurements on artificial opals with reduced refractive index contrast through which information on the shape of energy bands in the surroundings of the L-pseudogap was collected. Such information was obtained from Fabry-Perot oscillations originated from the interference between light reflected at the front and rear facets of the sample. This method is, however, limited by sample quality. As the thickness of the crystal increases, the contribution from the rear end of the crystal decreases as a consequence of light being scattered by defects and Fabry-Perot oscillations become less defined.

In order to explore the dispersive properties of 3D photonic crystals, phase sensitive techniques have been employed that have allowed the determination of the band structure in the surroundings of stop bands. Yablonovitch and Gmitter<sup>3</sup> extracted the band structure of a Yablonovite structure in the microwave regime for every direction within the first Brillouin zone. Later on, Watson and co-workers<sup>4,5</sup> used a modified Mach-Zehnder interferometer (MZI) to measure the phase delay introduced by colloidal crystals in the vicinity of the L-pseudogap. Another method for determining the band structure of a 3D crystal, not based on a phase sensitive technique, is that introduced in reference 6. In this approach, studying light

refraction of monochromatic beams propagating through the system allowed obtaining equi-frequency surfaces from which the band structure was reconstructed.

The above mentioned techniques also fail to provide information on the dynamics of light propagating through the crystal. In this case time resolved experiments have proven a valuable tool. The main interest in 3D photonic crystals has been placed on the spectral region close to the pseudogap edges, where energy bands bend near the edge of the Brillouin zone. This band bending implies a reduction in group velocity which increases the interaction time of electromagnetic radiation with the crystal. Also in a narrow spectral range around the pseudogap, time resolved experiments were performed using ultra-short pulses and a group velocity reduction was measured near the gap edges.<sup>7,8</sup> In the case of reference 8, the group velocity dispersion was also measured. Recently, white light interferometry was used to obtain the group velocity and its dispersion for thin film photonic crystals in a broad spectral range around the L pseudogap.<sup>9</sup>

In this chapter phase sensitive measurements are presented on artificial opals with an increasing number of layers. Employing white-light interferometry in the time domain the phase delay introduced by the samples is measured, which allows for the determination of the dispersion relation in a large spectral range. The probed frequencies span the interval which goes from below the red edge of the pseudogap to the high energy region of the band structure (see chapter 4). By derivation of the measured phase we may obtain the group velocity which provides information on the dynamics of light in the crystal.

For frequencies in the surroundings of the L-pseudogap, an effective refractive index is extracted from the measured phase delay which presents a region of anomalous dispersion across the pseudogap. The group velocity for frequencies close to the pseudogap edges presents a decrease which agrees with previous time resolved measurements with ultra short pulses and white light interferometry. The evolution of these features with the number of layers is discussed. Finally, some preliminary results are presented for the frequency range where higher order diffractions both by {111} planes and other families of planes take place.

## 2. Experimental

The experimental set-up<sup>3</sup> employed in the present measurements is that used in references 10 and 11 for probing the dispersive properties of silica substrates and dielectric mirrors respectively. It consists of a modified Mach-Zehnder interferometer (MZI) coupled to a commercial closed scanning Michelson interferometer (SMI). A diagram of the set-up is shown in figure 1a. Light from a quartz-tungsten halogen lamp enters the MZI and is split into the two arms of the

---

<sup>3</sup> Experiments were performed in the laboratories of the group of Prof. L. C. Andreani at the Dipartimento di Fisica "A. Volta", University of Pavia (Italy).

interferometer, one of which contains the sample and the other remains empty. The electric field as a function of time at the exit of the MZI may be expressed as the superposition of the one in the *reference* arm  $E_1(t)$  (without the sample) and the one in the *sample* arm  $E_2(t)$  (with the sample inserted):

$$E(t) = E_1(t) + E_2(t) = \int_{-\infty}^{+\infty} A(\omega)e^{i\omega t} d\omega + \int_{-\infty}^{+\infty} H(\omega)A(\omega)e^{i\omega(t+\frac{\Delta L}{c})} d\omega \quad (1)$$

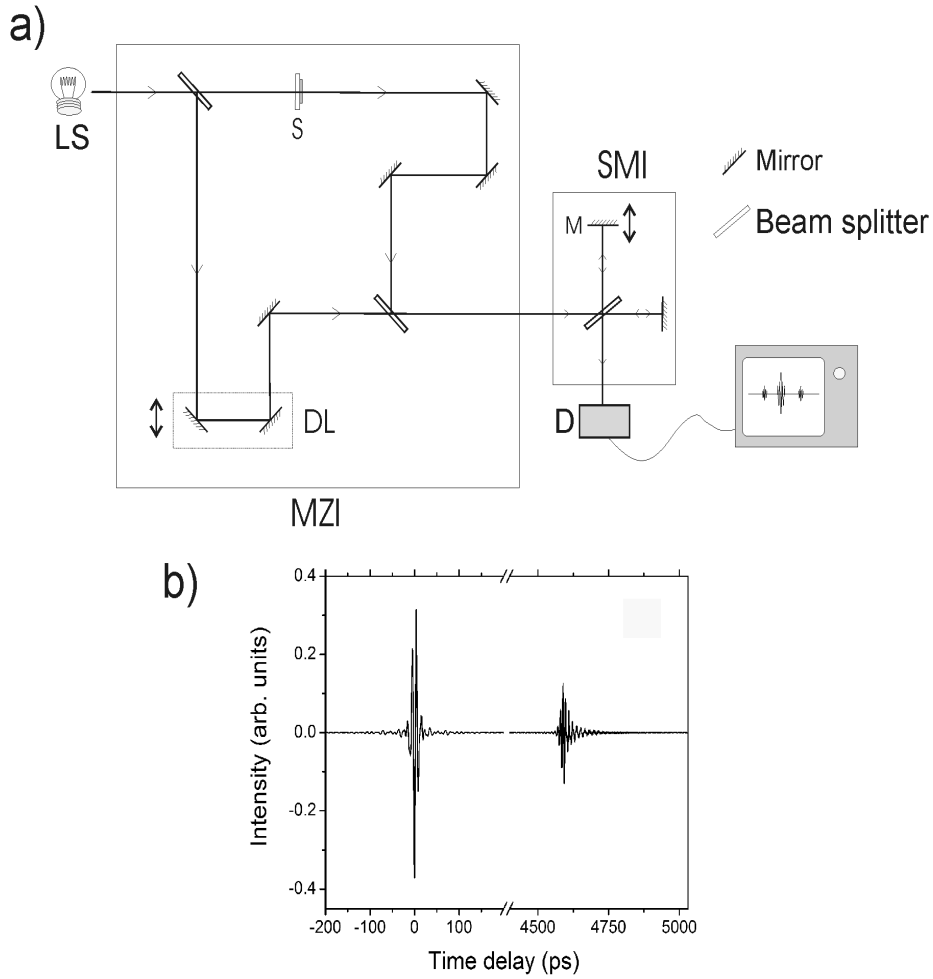


Figure 1: (a) Diagram of experimental set-up. Mach-Zehnder interferometer (MZI) containing a delay line (DL) is coupled to a scanning Michelson interferometer (SMI). Output beam is collected at the detector (D). Sample and light source are denoted by S and LS respectively. (b) Measured interferogram.

where  $A(\omega)$  is the spectral amplitude of the reference beam,  $H(\omega) = h(\omega)e^{i\theta(\omega)}$  the transfer function describing the sample response and  $\Delta L$  the optical path difference between the two arms of the MZI, which may be controlled with the delay line.

The exiting beam is then fed into the SMI. The signal collected by the detector in the SMI as a function of the scanning time of its movable mirror is the interferogram (figure 1b), which is the autocorrelation function of the two overlapped beams:<sup>12</sup>

$$\begin{aligned}
 I(\tau) &= \int_{-\infty}^{+\infty} E(t) \cdot E^*(t - \tau) dt \\
 &= \int_{-\infty}^{+\infty} H(\omega) |A(\omega)|^2 e^{i\omega(\tau - \frac{\Delta L}{c})} d\omega + \int_{-\infty}^{+\infty} \left[ |A(\omega)|^2 + |H(\omega)A(\omega)|^2 \right] e^{i\omega\tau} d\omega \\
 &\quad + \int_{-\infty}^{+\infty} H(\omega)^* |A(\omega)|^2 e^{i\omega(\tau + \frac{\Delta L}{c})} d\omega
 \end{aligned} \tag{2}$$

where the asterisk stands for the complex conjugate.

A typical interferogram is shown in figure 1b. The central symmetric lobe is the autocorrelation of the two signals and corresponds to the second integral in (2). Two side lobes, one being the mirror image of the other about the origin, appear. They are the cross-correlation, corresponding to the first and third integrals. These side-lobes present a strong asymmetry caused by the phase delay introduced by the sample. In figure 1b only one of them is shown as the other is its mirror image. The separation between the central and the side lobes is just the time delay between the two arms of the MZI  $\Delta t = \Delta L/c$ , which can be adjusted by means of the delay line.

The spectral dependence of the phase difference between the two beams  $\Delta\varphi(\omega)$  may be obtained from the Fourier transform of either of the cross-correlation functions:

$$\begin{aligned}
 \bar{I}(\omega) &= h(\omega) |A(\omega)|^2 e^{i\Delta\varphi(\omega)} \\
 \Delta\varphi(\omega) &= \text{Im}[\ln \bar{I}(\omega)] = \theta(\omega) + \omega \frac{\Delta L}{c}
 \end{aligned} \tag{3}$$

Therefore to extract the phase delay introduced by the sample alone one has only to subtract the phase difference obtained with the sample in the sample arm, that is (3), and with the sample arm empty:

$$\Delta\varphi(\omega)_r = \omega \frac{\Delta L}{c} - \frac{\omega D}{c} \tag{4}$$

and then add  $\omega D/c$ , where  $D$  is the sample thickness. Since the sample is standing on a glass substrate, the reference measurement is made only with the substrate. In order to assure that the phase introduced by the substrate is properly

subtracted, its thickness should be the same in both the sample and reference measurements. The substrate thickness was observed to remain constant (within 100 nm) over distances of 2 mm across the substrate. This was done by translating the substrate across the probe beam and observing the separation between the auto and the cross-correlation lobes in the interferogram, and assuming a refractive index provided by the substrate manufacturers (Menzel-Glaser) of 1.51. The sample areas to be probed ( $\sim 125 \mu\text{m}$ ) were chosen so that an exposed substrate region was available within 2 mm.

The set-up allowed for measuring transmission at the exact place where phase measurements were performed. This was done by just blocking the reference arm of the MZI. In this way the measurement is identical to the ones introduced in chapter 3. By doing so the sample thickness could be estimated from Fabry-Perot fringes (see chapter 3). Samples with thickness varying between 5 and 40 layers were employed in the present measurements. The use of a tungsten-halogen lamp together with silicon and indium antimonide detectors permitted measuring the phase delay over a wide spectral range (400 - 3000 nm). Employing samples made of spheres with diameters of 505 and 705 nm the frequency interval  $0.4 < a/\lambda < 2$  in reduced frequency units, previously explored in chapters 3 and 4 by means of reflection and transmission spectroscopy, could be probed. This represents a clear improvement from previous phase sensitive measurements in colloidal crystals ( $0.59 < a/\lambda < 0.68$ )<sup>4,5</sup> and thin film opals ( $0.43 < a/\lambda < 1.15$ ).<sup>9</sup> Besides the advantages concerning the spectral range covered in the measurements, the present technique allows for a time resolution of  $10^{-2}$  fs, which translates into a resolution of  $10^{-2}$  radians (for a wavelength of 1 micron) when obtaining the phase.

### 3. Low energy spectral region

We first study the phase delay introduced by our samples in the spectral region  $0.4 < a/\lambda < 0.9$ , corresponding to the L-pseudogap and its surroundings. Figure 2 shows the evolution of the phase delay as the number of layers is increased. For a small number of layers it is just a straight line, resembling the behavior of a transparent homogeneous material. As the thickness of the crystal increases, the slope of the phase delay decreases as would be expected for an increasing optical path. Further, a phase jump develops for those frequencies contained within the L-pseudogap, indicated by dashed horizontal lines in the figure. A similar jump is known to take place across the forbidden intervals of 1D photonic crystals with a sufficient number of layers,<sup>11</sup> and to be a signature of anomalous dispersion due to Bragg diffraction. In the present case we would expect a similar behavior as these systems may be regarded as 1D systems for this particular energy range and orientation. At variance with previous determinations of phase delays for similar systems,<sup>4,5</sup> here the thickness of the samples is such that enough signal is collected for frequencies within the pseudogap.

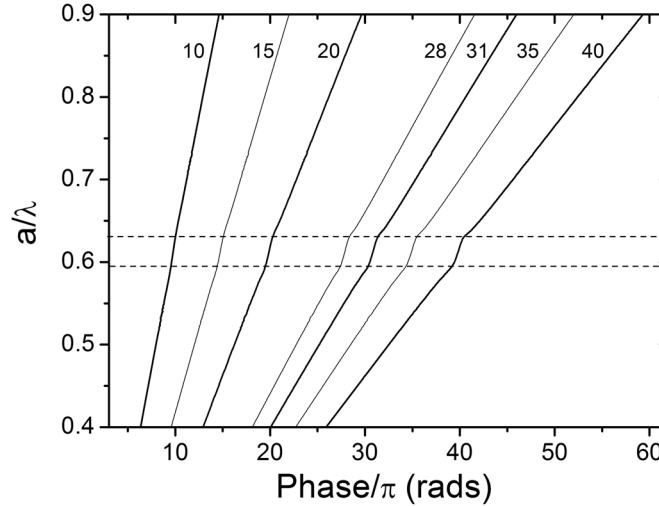


Figure 2: Phase delay for samples having an increasing number of layers. Left to right: 10, 15, 20, 28, 31, 35 and 40 layers.

Once the phase delay is known we can extract from it an effective refractive index  $n_{eff}$  for our crystals assuming an effective medium behavior. The concept of such  $n_{eff}$  has been extensively explored for 1D photonic crystals.<sup>13</sup> It has proven to correctly describe the dispersive properties of such structures, especially in terms of the possibility of obtaining phase matching conditions for second harmonic generation.<sup>14</sup> This  $n_{eff}$  has also been used to successfully account for the observation of third harmonic generation in samples similar to the ones used in these measurements,<sup>15</sup> and second harmonic generation in dye doped colloidal crystals.<sup>16</sup> The crystal is considered a homogeneous medium with refractive index  $n_{eff}$  and thickness  $D = d_{111}N$ , where  $d_{111} = a/(3)^{1/2}$  is the interplanar distance for the  $\{111\}$  planes parallel to the surface and  $N$  the number of sphere planes. Under this assumption, the measured phase delay  $\theta(\omega)$  may be expressed as:

$$\theta(\omega) = \frac{2\pi}{\lambda} n_{eff} D \quad (5)$$

In this way we have extracted  $n_{eff}$  for samples with an increasing number of layers. The results are plotted in figure 3. As the thickness of the sample increases a region of anomalous dispersion becomes apparent for frequencies around  $a/\lambda \sim 0.61$  where the pseudogap is located. In homogeneous materials anomalous dispersion is associated with spectral regions where absorption or gain takes place. In the present situation the origin of this anomalous dispersion is related to extinction by Bragg diffraction as in the 1D case.<sup>13</sup> In order to assure that this is the situation, the scalability of the experimental results was checked. In figure 3d identical measurements for samples with 10 layers made of spheres having diameters of 505 and 705 nm are shown. The coincidence is excellent and therefore the anomalous

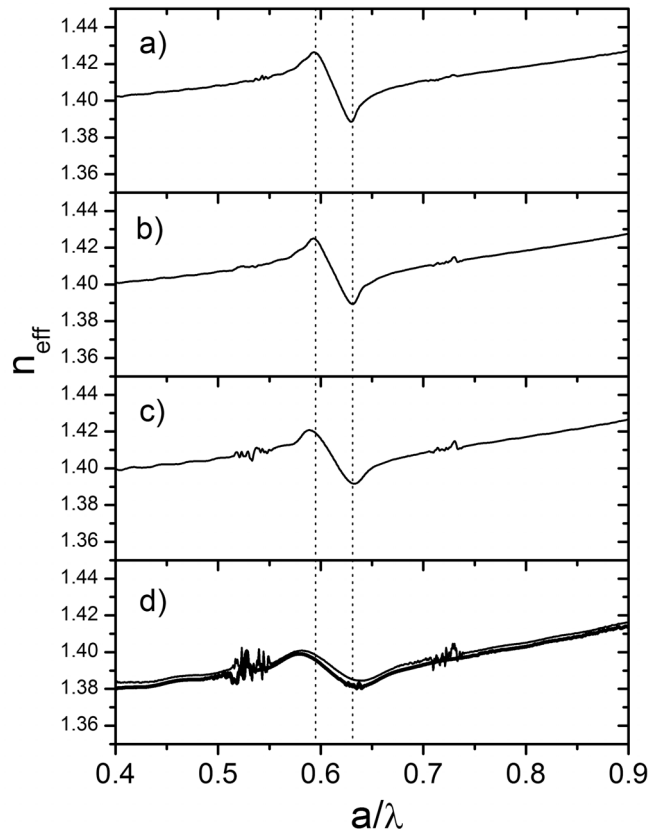


Figure 3: Effective refractive index extracted from the phase delay measurements for samples having different number of layers: 40 (a), 31 (b), 20 (c) and 10 (d). Vertical dashed lines indicate the edges of the L-pseudogap as extracted from band calculations. All samples made of spheres with 705 nm diameter except from thick line in figure (c), made out of 505 nm spheres.

dispersion may be associated with Bragg diffraction due to the periodicity of the structure and not to absorption of the materials comprising the crystal. Regions of anomalous dispersion due to water vapour absorption may be seen at both sides of the main feature discussed.

In the low energy region the refractive index presents a normal dispersion. For  $a/\lambda=0.4$ , the refractive index extracted from the phase delay takes on a value which monotonically increases from 1.385 (for 10 layers samples) to 1.405 (for 40 layers samples), a value close to the 1.41 predicted by the slope of the bands in the low frequency limit. The fact that the measured  $n_{eff}$  increases with sample thickness is probably a consequence of the fact that the approximation of the crystal as a homogenous medium becomes more realistic as we increase the number of layers. As the crystal thickness increases the region of anomalous dispersion becomes spectrally narrower. This evolution coincides with that of the reflectivity peak (see chapter 3) as would be expected, both features being associated with extinction due

to Bragg diffraction. Also the maximum and minimum values of  $n_{eff}$  at the edges of the anomalous dispersion region, as compared to the low frequency value, increase as a function of crystal thickness. This corresponds to the fact that Bragg diffraction (and therefore extinction responsible for the anomalous dispersion) becomes more efficient with the number of planes. This shows that if second or third harmonic generation is to be observed in such systems, as in references 15 and 16, the size of the crystal will be determinant in achieving the phase matching condition.

These results represent a clear improvement with respect to previous phase delay data measured in colloidal crystals.<sup>4,5</sup> On the one hand, the good quality and reduced thickness of the samples allow for measuring the phase delay for frequencies within the pseudogap, not observed previously due to the lack of signal as a consequence of the crystal size. These data then represent the first observation of anomalous dispersion in refractive index across the pseudogap of a 3D photonic crystal. Further, the increased refractive index contrast of our samples with respect to the above mentioned colloidal crystals allow for the observation of variations of the effective refractive index of up to 0.015 between the long wavelength limit and those frequencies close to the pseudogap. This value is an order magnitude larger than the one obtained with colloidal crystals having 1000 planes.

Once the phase delay is measured, the effective dispersion relation of the sample can be obtained in a straightforward manner as  $k(\omega)=\theta(\omega)/D$ . Then one may obtain the group velocity  $v_g$  associated with propagation along the  $\Gamma L$  direction which is just the derivative of the dispersion relation with respect to the frequency. In our case it is the inverse group velocity times the speed of light in vacuum that we calculate;

$$\frac{c}{v_g} = \frac{c}{D} \frac{dk}{d\omega} \quad (6)$$

The group velocity can be defined as the velocity at which the peak amplitude of a pulse traverses a medium. Therefore it provides information on the dynamics of light propagation through that medium. For an infinite photonic crystal, the  $v_g$  at a certain frequency may be calculated as the slope of the corresponding band at that frequency.  $v_g$  equals the energy velocity, that is the speed at which electromagnetic energy propagates.<sup>13</sup> In the absence of available states neither of them is defined as no energy can propagate through the medium. But for a finite crystal the situation is different. Here, for frequencies located within a forbidden interval, light will be exponentially attenuated but it may still be transmitted through the crystal. In the presence of extinction,  $v_g$  does not equal the energy velocity<sup>17</sup> and care must be taken when interpreting experimental results.

In figure 4 the evolution of  $c/v_g$  extracted from (6) is plotted for samples having an increasing number of layers. Some interesting points must be noted in this graph. For samples just 10 layers thick  $c/v_g$  is basically constant with frequency. Noisy regions appear which correspond to the anomalous dispersion associated with water vapour absorption observed in the results for  $n_{eff}$ . As the thickness

increases, two peaks of low  $v_g$  develop at frequencies close to the pseudogap edges (indicated by dotted vertical lines), and a region of high  $v_g$  appears in between them. For increasing number of layers the two peaks become more pronounced and shift closer to the position of the pseudogap edges. Far from these frequencies the  $v_g$  presents oscillations around a constant value. Such oscillations coincide with Fabry-Perot resonances observed in reflectance and transmittance,<sup>9,11</sup> and are a result of the finite size of the sample.

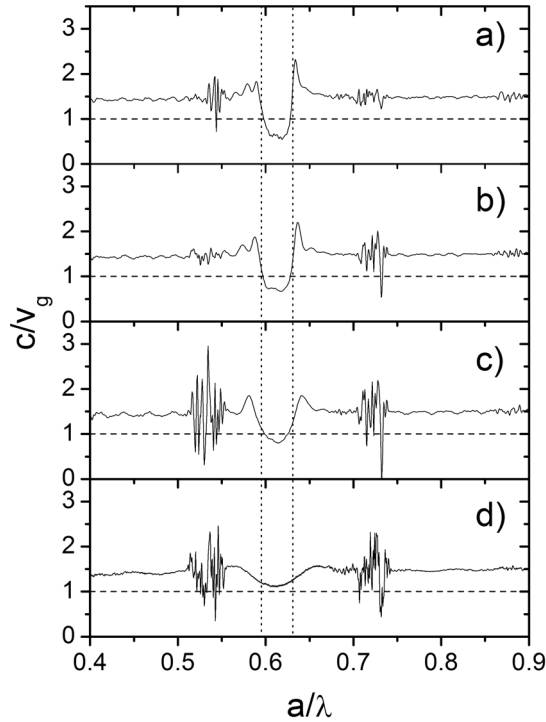


*Figure 4: Inverse group velocity for samples with increasing number of layers. Top to bottom: 40, 31, 20 and 10 layers. Horizontal dashed lines indicate the limit of superluminal velocity  $v_g=c$ . Vertical dotted lines indicate the pseudogap edges predicted by calculated bands.*

Near the edges of the pseudogap, energy bands separate from the low energy linear behaviour and become flat. Thus, the  $v_g$  associated with the frequencies near the edges becomes extremely low. For an ideal infinite crystal the modes with these frequencies become standing waves. For real finite crystals these “heavy” photons with such frequencies experience a very long optical path inside the structure, and their interaction time with the crystal is enhanced.<sup>18</sup> By introducing non linear optical materials in 1D photonic crystals this effect may lead to optical limiting and switching,<sup>19</sup> and enhanced second harmonic generation by adequately tailoring the dispersion relation of the crystal.<sup>14</sup> If active media are introduced instead, enhanced gain could be achieved.<sup>18,20</sup> In the results presented in figure 4 the two peaks of low  $v_g$  correspond to the spectral interval where anomalous dispersion was observed

and may then be identified with the appearance of Bragg diffraction by the  $\{111\}$  planes parallel to the sample surface. This evolution can then be considered as a signature of the formation of the energy bands in this spectral region of the band structure, where the decrease in  $v_g$  can be associated with the bending of the energy bands near the pseudogap. For the sample 40 layers thick the trend followed by  $v_g$  coincides with theoretical predictions extracted from the bands as can be seen in figure 5. Near the pseudogap edges, experimental values are below theoretical ones. This is probably due to finite size effects, as more layers will be needed in order to achieve a more pronounced slowing. The observed reduction in  $v_g$  reaches a maximum of 40% at the high energy edge of the pseudogap. This is larger than previous  $v_g$  reductions observed in colloidal crystals with  $\sim 1400$  planes,<sup>8</sup> and thin film opals with fewer layers ( $\sim 20\%$ ).<sup>9</sup> As in the variations regarding the effective refractive index, increasing the photonic strength of our system by augmenting the refractive index contrast allows the observation of phenomena related to band edge bending with thinner samples, which show a sufficiently large signal within the pseudogap.

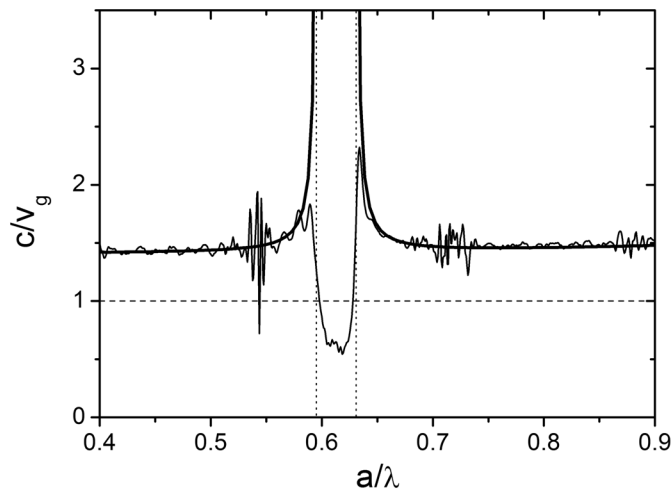


Figure 5: Inverse group velocity as a function of frequency for a sample 40 layers thick (thin line). Theoretical predictions extracted from the bands appear as thick solid line. Vertical dotted lines correspond to pseudogap edges. Horizontal dashed line represents the limit of superluminal propagation ( $c=v_g$ ).

For frequencies within the pseudogap, the group velocity is observed to take on values above the long wavelength limit, reaching a superluminal behaviour ( $v_g > c$ ) for samples only 15 layers thick. Superluminal group velocities have been experimentally observed with pulses propagating through 1D photonic crystals<sup>21,22</sup> and also extracted from phase delay measurements.<sup>9,11</sup> Such results, although striking, are known not to be at odds with causality. For a finite system the group and energy velocities are not the same at those regions for which strong extinction

takes place (i.e. inside the pseudogap), and the energy velocity remains below  $c$  for all frequencies.<sup>17</sup>

But slowing at frequencies close to the pseudogap edges is not only related to gain or SHG enhancement. The fact that photons experience a longer optical path for these frequencies implies that they are more likely to be scattered by defects in the lattice. This was already observed in chapter 3 as an enhancement of the diffuse intensity generated inside the crystal. One may compare the frequency dependence of the optical response of the 40 layers thick sample with the group velocity, as in figure 6. Here it is clearly seen that pulse slowing is related to an enhancement in diffuse intensity. Taking a close inspection at the figure, there is an evident asymmetry between the group velocity and the diffuse intensity. In the low energy edge there is a clear enhancement of diffuse intensity which coincides with a smaller group velocity, as compared to the high energy edge (where no enhancement of diffuse intensity is present). It seems that the generation of diffuse intensity counteracts the effect of sample thickness in the evolution of the  $v_g$ , which is expected to decrease with the number of layers.

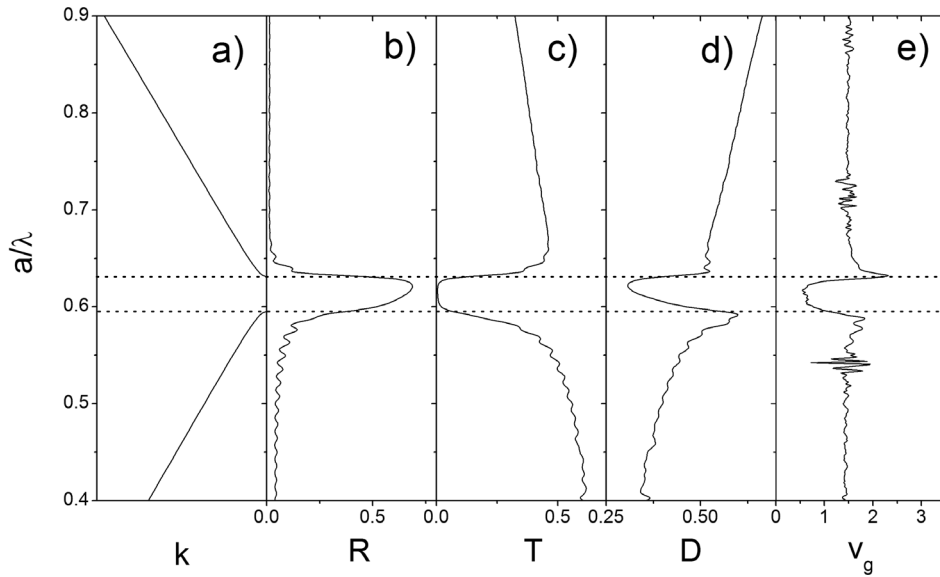


Figure 6: (a) Band structure for a polystyrene opal along the  $\Gamma L$  direction. (b) Reflectance, (c) transmittance and (d) diffuse intensity for a 42 layers thick sample. (e) Inverse group velocity for a 40 layers thick sample.

#### 4. High energy spectral region

We next consider the evolution of the phase as a function of the number of layers in the high energy spectral region where second and third order Bragg

diffraction by the  $\{111\}$  planes parallel to the surface are expected together with the onset of diffraction. This is shown in figure 7 for samples with variable thickness and sphere diameters. The thickest samples considered have 28 layers. This limitation was imposed by the low transmission present in this frequency range (see chapter 4). At variance with the results for the low energy range where a single feature (namely a phase jump) was observed in the measured phase delay, here a number of features are present in the reduced frequency window  $1.1 < a/\lambda < 1.3$ , the most pronounced being the one taking place at  $a/\lambda \sim 1.1$  where the onset of diffraction is expected. This is in agreement with the complicated reflectance and transmittance spectra previously obtained in this frequency interval. For reduced frequencies  $a/\lambda > 1.3$ , the phase delay presents a linear behavior, expected for a homogeneous medium. This is also in agreement with transparency regions observed in reflection and transmission spectra.

With increasing sample thickness the phase jumps become more defined, eventually present a flip in their sign and loose definition again. In particular we shall focus on the behavior of the first and most pronounced jump taking place for a frequency  $a/\lambda \sim 1.1$ . In figure 7a results for samples grown from spheres of 705 nm are presented. The thickness for which the sign flip takes place for the first jump is 12-13 layers. For spheres 505nm in diameter results are only shown for a number

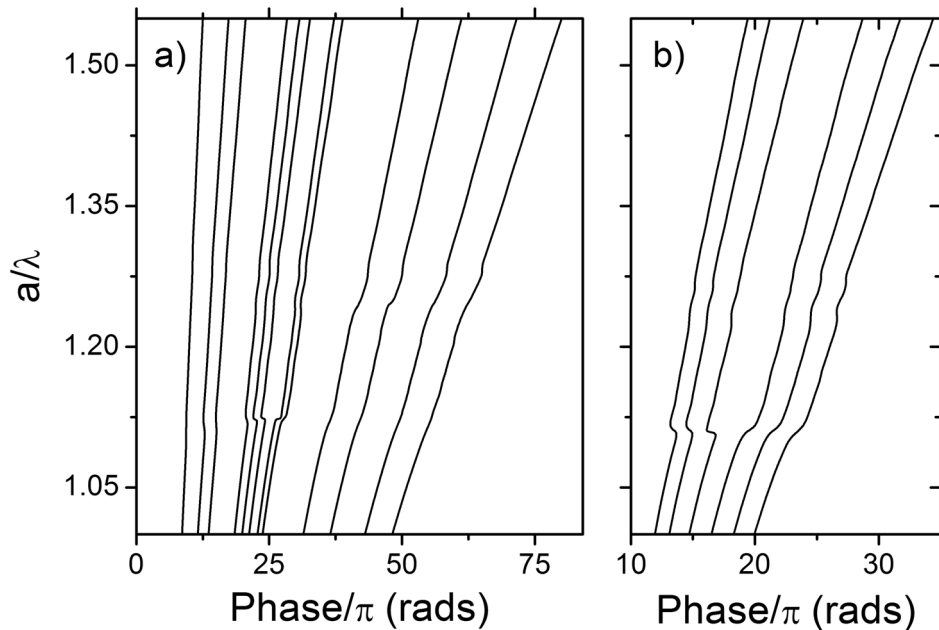


Figure 7: Phase delay introduced by samples with an increasing number of layers. (a) 705 nm spheres samples having, left to right; 4, 6, 7, 10-14, 18, 21, 25 and 28 layers. (b) 505 nm spheres samples having, left to right; 7-12 layers.

of layers around the critical thickness, which for this sphere diameter turns to be 9-10 layers (see figure 7b). Here it must be noted that the spectral position of the jumps is scalable with sphere size so that one expects them to have their origin in the band structure. The fact that the sample thickness for which the sign flip takes place for each sphere diameter is different is not understood at this point. More results on different samples and also for spheres with different diameters are needed in order to further explore this behavior. Nevertheless, the fact that it takes place at the spectral region where the onset of diffraction is expected makes us think that it is related to the presence of diffraction bands.

Contrary to the situation in the low energy region described in the preceding section, where the phase jump could be associated with Bragg diffraction by the  $\{111\}$  planes parallel to the surface alone, here the coexistence of linear and diffraction bands complicates an interpretation. In the former situation, incident light could only couple to a set of degenerate bands and the contribution to the phase delay could be clearly identified. Now light may couple to a number of bands, the information contained in the phase delay is due to all of them, and extracting single contributions is challenging at this point.

The next step is to extract the group velocity by deriving the phase delay according to (5). Results are plotted in figure 8 for samples with different thickness. Results are smoothed by averaging over 4 adjacent points. Raw data is also shown in grey in order to verify that none of the main features are lost. As one

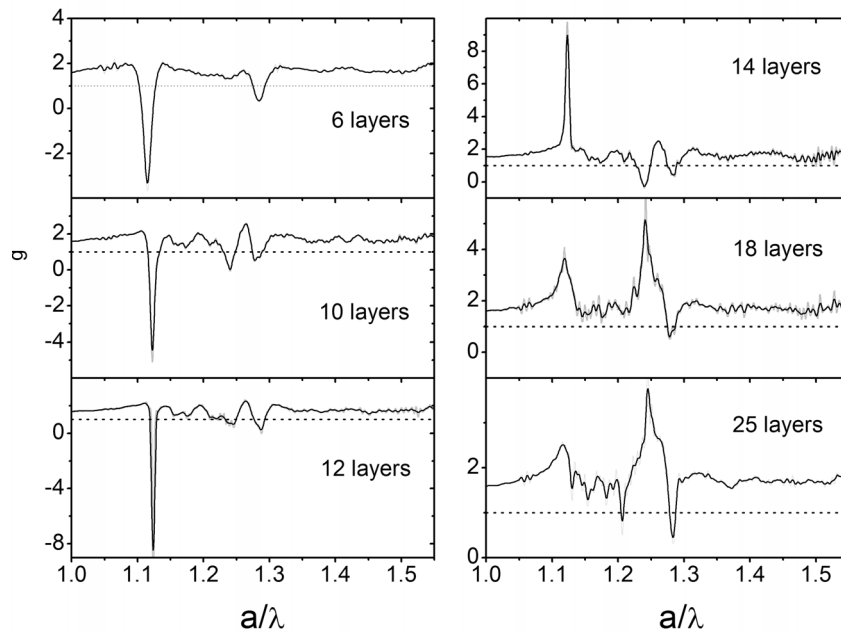


Figure 8:  $c/v_g$  determined from the phase delay measurements for samples having different thickness. Black lines are smoothed data and grey lines are raw data.

would expect, the presence and evolution of the features observed for the phase delay has a correspondence in the group velocity. In the spectral region  $1.1 < a/\lambda < 1.3$  a number of peaks of low and high group velocity are found. Here “slow” photons, superluminal and even negative group velocities are observed. The flip in the sign of the phase jumps translates into abrupt changes of the sign of the features in the group velocity. In this sense, increasing the number of layers by one may yield a transition from negative group velocities to extremely low ones (a factor of 6 slower than the constant value obtained in the low energy region). The existence of a negative value is a rather shocking result, as it implies that the peak of a pulse propagating with its central frequency centered in that spectral region would leave the sample before entering it.<sup>23</sup> Negative group velocities have been previously observed in the optical regime for transparent anomalous dispersive media<sup>24</sup> and 2D periodic arrays of sub-wavelength apertures in metallic films.<sup>25</sup> In both cases such values for  $v_g$  were explained in terms of classical interference of light which traverses an anomalously dispersive medium.<sup>23</sup> In both situations it was pointed out that the results were not at odds with causality.

The present measurements are not an experimental artifact due to the derivation process. At the spectral regions where unusual values for  $v_g$  are found the phase does not present an abrupt jump but is rather a smoothly varying function (with over 20 measured points in the sharpest features). If such values were a consequence of the fact that the phase is lost, a random behavior would be expected which is not the case. Instead, an evolution with the number of layers is observed which is reproduced with sphere size (although a change in the critical thickness appears which is not understood).

For samples having 18 layers, the group velocity seems to reach a stationary behavior. Increasing the number of layers (up to 28 in the present measurements) does not introduce further changes in the sign of the observed features. The only change is that they seem to become less defined. Therefore it seems adequate to choose samples with thickness above 18 layers to compare them with calculated bands. This has been done in figure 9, where reflectance and transmittance measurements for a sample 25 layers thick are compared with calculated bands and the inverse group velocity. It can be seen that features in the group velocity correspond to features in reflectance and transmittance in the spectral region where flat diffraction bands appear in the band structure. As in the case of spectroscopic measurements, assigning features to certain bands is not trivial. In this frequency interval light may couple to several bands for a given frequency so that information from all of them will be contained in the phase measurements. For reduced frequencies  $a/\lambda > 1.3$ , we find that  $v_g$  does not present any more abrupt peaks. This coincides with the fact that the samples present a transparency region for those frequencies where Fabry-Perot oscillations may be observed (see chapter 4).

Our situation would be closer to that of the periodic array in reference 25. For that system it was observed that  $v_g$  presented a strong spectral modulation (going from negative to positive –but low– values) associated with a modulation in the transmitted intensity. In our case, the spectral region where  $v_g$  undergoes a strong

modulation coincides with the region where the optical response presents marked features. Further, in reference 25 they observed that the largest negative value for  $v_g$  is at the frequency where the Wood anomaly takes place, where light is diffracted at grazing angle and is resonantly transferred to surface wave modes. In our case the largest (negative) value for  $v_g$  occurs for thin samples at the frequency where the onset of diffraction takes place. As the sample thickness increases the situation becomes more complicated and an analogy with a simple 2D grating does not seem realistic, the band structure being a more reliable tool for interpretation.

To obtain more detailed information from energy bands at this stage is a difficult task. As mentioned in chapter 4, knowing the coupling strength of the incident frequency to each band would be useful in determining their contribution to the measured phase delay. Nevertheless, these results are relevant on its own as they represent the first phase sensitive measurements in this spectral region.

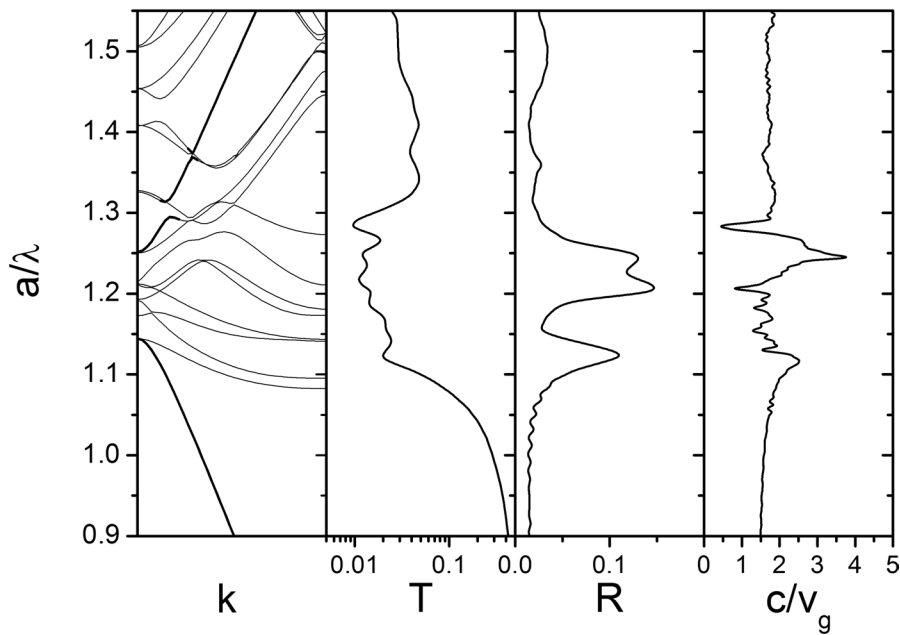


Figure 9: (a) Band structure for an artificial opal made out of polystyrene spheres. Thick lines represent linear bands (as defined in chapter 4). (b) Transmission for a sample 25 layers thick. (c) Reflection for a sample of the same thickness. (d) Inverse group velocity extracted from phase delay measurements for a sample with the same thickness.

## 5. Conclusions and future work

In this chapter phase sensitive measurements obtained using white-light interferometry in the time domain have been presented for samples with variable thickness and sphere size. The spectral range covered in the present experiments spans the low energy region around the L-pseudogap and the high energy region where the onset of diffraction takes place. They complement previous optical characterization by means of reflectance and transmittance spectroscopy presented in chapters 3 and 4.

In the low energy region, the phase delay is seen to develop a phase jump as a consequence of Bragg diffraction by the  $\{111\}$  planes parallel to the surface. Assuming an effective medium behavior we have extracted an effective refractive index  $n_{eff}$  for the crystal which presents a region of anomalous dispersion corresponding to those frequencies where the phase jump was present. The variation observed in the  $n_{eff}$  as a function of sample thickness indicates caution must be taken if similar systems are to be used for obtaining phase matching scenarios. Deriving the phase delay we have been able to extract the group velocity  $v_g$ , which presents low values close to the pseudogap edges where energy bands flatten, and high (even superluminal) values for frequencies within.

The phase delay in the high energy region presents a complicated behavior with the appearance of a number of features in the same spectral position as those observed in reflectance and transmittance spectroscopy. When extracting the group velocity in this frequency interval we have observed situations in which superluminal and even negative group velocities are present. Such values appear for frequencies corresponding to dispersionless bands. The evolution of the phase delay with the sample thickness in this spectral region is not well understood at present and deserves further attention.

## 6. References

- <sup>1</sup> Sakoda, K. “*Optical properties of photonic crystals*”, Springer-Verlag, Berlin (2001).
- <sup>2</sup> Vlasov, Y. A., Deutsch, M. and Norris, D. J. “*Single-domain spectroscopy of self-assembled photonic crystals.*” *Applied Physics Letters* **76**, 1627-1629 (2000).
- <sup>3</sup> Yablonovitch, E. and Gmitter, T. J. “*Photonic Band-Structure - the Face-Centered-Cubic Case.*” *Physical Review Letters* **63**, 1950-1953 (1989).
- <sup>4</sup> Tarhan, II, Zinkin, M. P. and Watson, G. H. “*Interferometric-Technique for the Measurement of Photonic Band-Structure in Colloidal Crystals.*” *Optics Letters* **20**, 1571-1573 (1995).
- <sup>5</sup> Rosner, B. T., Schneider, G. J. and Watson, G. H. “*Interferometric investigation of photonic band-structure effects in pure and doped colloidal crystals.*” *Journal of the Optical Society of America B-Optical Physics* **15**, 2654-2659 (1998).
- <sup>6</sup> Notomi, M., *et al.* “*Direct visualization of photonic band structure for three-dimensional photonic crystals.*” *Physical Review B* **61**, 7165-7168 (2000).
- <sup>7</sup> Vlasov, Y. A., *et al.* “*Femtosecond measurements of the time of flight of photons in a three-dimensional photonic crystal.*” *Physical Review E* **60**, 1030-1035 (1999).
- <sup>8</sup> Imhof, A., Vos, W. L., Sprik, R. and Lagendijk, A. “*Large dispersive effects near the band edges of photonic crystals.*” *Physical Review Letters* **83**, 2942-2945 (1999).
- <sup>9</sup> von Freymann, G., *et al.* “*Measurement of group velocity dispersion for finite size three-dimensional photonic crystals in the near-infrared spectral region.*” *Applied Physics Letters* **86**, art. no.-053108 (2005).
- <sup>10</sup> M. Galli, F. Marabelli, and G. Guizzetti, *Appl. Opt.* **42**, 3910 (2003).
- <sup>11</sup> Galli, M., *et al.* “*Photonic bands and group-velocity dispersion in Si/SiO<sub>2</sub> photonic crystals from white-light interferometry.*” *Physical Review B* **69**, art. no.-115107 (2004).
- <sup>12</sup> Bell, R. J. “*Introductory Fourier transform spectroscopy*”, Academic Press, New York (1972).
- <sup>13</sup> Yariv, A. and Yeh, P. “*Electromagnetic propagation in periodic stratified media. II. Birefringence, phase matching and x-ray lasers.*” *Journal of the Optical Society of America* **67**, 438-448 (1977).
- <sup>14</sup> Centini, M., *et al.* “*Dispersive properties of finite, one-dimensional photonic band gap structures: Applications to nonlinear quadratic interactions.*” *Physical Review E* **60**, 4891-4898 (1999).
- <sup>15</sup> Markowicz, P. P., *et al.* “*Dramatic enhancement of third-harmonic generation in three-dimensional photonic crystals.*” *Physical Review Letters* **92** (2004).
- <sup>16</sup> Martorell, J., Vilaseca, R. and Corbalan, R. “*Second harmonic generation in a photonic crystal.*” *Applied Physics Letters* **70**, 702-704 (1997).
- <sup>17</sup> D'Aguzzo, G., *et al.* “*Group velocity, energy velocity, and superluminal propagation in finite photonic band-gap structures.*” *Physical Review E* **6303**, art. no.-036610 (2001).

- <sup>18</sup> Dowling, J. P., Scalora, M., Bloemer, M. J. and Bowden, C. M. “*The Photonic Band-Edge Laser - a New Approach to Gain Enhancement.*” *Journal of Applied Physics* **75**, 1896-1899 (1994).
- <sup>19</sup> Scalora, M., Dowling, J. P., Bowden, C. M. and Bloemer, M. J. “*Optical Limiting and Switching of Ultrashort Pulses in Nonlinear Photonic Band-Gap Materials.*” *Physical Review Letters* **73**, 1368-1371 (1994).
- <sup>20</sup> Vlasov, Y. A., *et al.* “*Enhancement of optical gain of semiconductors embedded in three-dimensional photonic crystals.*” *Applied Physics Letters* **71**, 1616-1618 (1997).
- <sup>21</sup> Steinberg, A. M., Kwiat, P. G. and Chiao, R. Y. “*Measurement of the Single-Photon Tunneling Time.*” *Physical Review Letters* **71**, 708-711 (1993).
- <sup>22</sup> Spielmann, C., Szepcok, R., Stingl, A. and Krausz, F. “*Tunneling of Optical Pulses through Photonic Band-Gaps.*” *Physical Review Letters* **73**, 2308-2311 (1994).
- <sup>23</sup> Dogariu, A., Kuzmich, A., Cao, H. and Wang, L. J. “*Superluminal light pulse propagation via rephasing in a transparent anomalously dispersive medium.*” *Optics Express* **8**, 344-350 (2001).
- <sup>24</sup> Wang, L. J., Kuzmich, A. and Dogariu, A. “*Gain-assisted superluminal light propagation.*” *Nature* **411**, 974-974 (2001).
- <sup>25</sup> Dogariu, A., *et al.* “*Delay in light transmission through small apertures.*” *Optics Letters* **26**, 450-452 (2001).

## CHAPTER 6

---

# Polarization dependence of the optical response of artificial opals

### 1. Introduction

The presence of “effective” pseudogaps in the optical response of photonic crystals was first pointed out in 1992 by Robertson *et al.*<sup>1</sup> As opposite to “real” pseudogaps, originated by the absence of available modes, “effective” ones are due to the existence of bands which may not be accessed by an external probe beam due to a symmetry mismatch between the external beam and the photonic mode. In that work, the way the symmetry of the incident beam affected the coupling of light to certain energy bands was observed for 2D systems. In that same year the existence of uncoupled modes, that cannot be coupled to for symmetry reasons, was also introduced for 3D systems.<sup>2</sup> Later, in 1995, Sakoda presented a rigorous description of the symmetry of the eigenmodes of a 2D photonic crystal and discussed the effect that the polarization of the incident beam would have on the optical response of a photonic crystal.<sup>3</sup>

Ever since, the effect of the polarization on the optical response of opal-based photonic crystals has been observed in a number of systems.<sup>4,5</sup> For the particular case of artificial opals made of silica spheres, a complete characterization of the eigenmodes in terms of their symmetry properties was performed by López-Tejiera *et al.* in 2002.<sup>6</sup> In that work it was predicted that the effect of uncoupled modes on the optical response of such systems could not be appreciated for normal incidence measurements on the  $\{111\}$  planes. This is due to the fact that for this direction, uncoupled modes coexist with allowed ones. But this situation changed for directions other than normal incidence, in accordance with previous results for related systems. The object of the present chapter is to present experimental evidences on how light with different polarization can only couple to certain bands in the lowest energy range of the band structure of artificial opals. In order to achieve our goal we analyze the four bands determining the first pseudogap in the vicinity of the  $L$  point of the Brillouin zone. This can be thought of as the pseudogap associated with diffraction by the  $\{111\}$  set of crystalline planes. This is

done by means of angle resolved reflectivity measurements. It is found that the polarization of the incident beam influences both, the spectral width and the intensity of the reflected beam.

## 2. Symmetry of photonic bands and incident beam

The four lowest bands in the vicinity of the L point for an opal structure are identical irrespective of the direction along the surface of the Brillouin zone for an angular range going from normal incidence to an internal angle of about 34 degrees and slightly departing from a common behavior only for higher angles. This is equivalent to saying that within a circle inscribed in the hexagonal face of the Brillouin zone the photonic bands are isotropic. So, for the sake of simplicity, we can take the  $\Gamma$ LU triangle as representative and assume incident light with its wave vector  $\mathbf{k}$  contained in that plane, the tip of  $\mathbf{k}$  lying on the LU segment (see Fig. 1). This allows classifying the bands by their behavior under mirror reflection with respect to that plane, which coincides with the diffraction plane. Both symmetric (2<sup>nd</sup> and 3<sup>rd</sup>) and anti-symmetric (1<sup>st</sup> and 4<sup>th</sup>) bands are to be found bounding the first Bragg peak.<sup>6</sup>

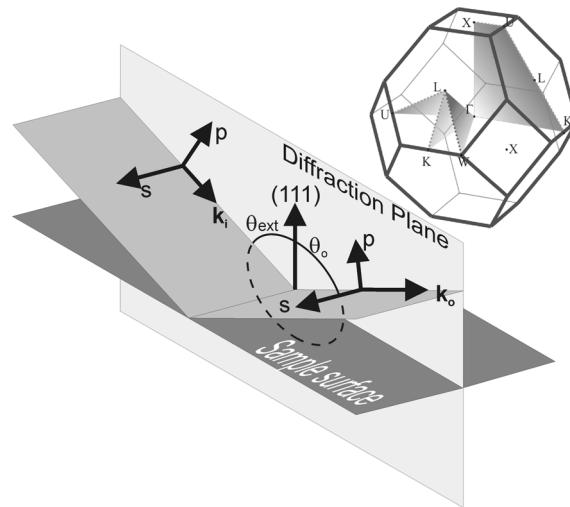


*Figure 1: Geometry of the experiment. The diffraction plane is represented in light gray. The sample surface plane is represented in dark gray. The inset shows the first Brillouin zone for a fcc structure. High symmetry points are indicated*

Let us now consider the symmetry properties of the incident field for any wave vector  $\mathbf{k}$  contained in the  $\Gamma$ LU plane. The electric field  $\mathbf{E}$  can always be written as a linear combination of two base vectors contained in a plane perpendicular to  $\mathbf{k}$ . In

particular, it is convenient to choose such vectors as parallel ( $\mathbf{e}_p$ ) and perpendicular ( $\mathbf{e}_s$ ) to the diffraction plane (see Fig. 1). Hence,  $\mathbf{E} = \alpha\mathbf{E}_s + \beta\mathbf{E}_p$  with  $\mathbf{E}_s = E_0\mathbf{e}_s$ ;  $\mathbf{E}_p = E_0\mathbf{e}_p$ ;  $\mathbf{e}_s \cdot \mathbf{e}_p = \mathbf{e}_k \cdot \mathbf{e}_p = \mathbf{e}_k \cdot \mathbf{e}_s = 0$  and  $\alpha^2 + \beta^2 = 1$  where  $\mathbf{e}_k$  is a unit vector in the direction of propagation  $\mathbf{k}$ . When light is linearly polarized perpendicular to the diffraction plane ( $\alpha = 1$  and  $\beta = 0$ ), the electric field  $\mathbf{E}$  is equal to  $\mathbf{E}_s$ . On the other hand,  $\mathbf{E} = \mathbf{E}_p$  for the case of parallel polarization ( $\alpha = 0$  and  $\beta = 1$ ). Then, in the p-polarized configuration the  $\mathbf{E}$  field is contained in the diffraction plane, and mirror reflection with respect to that plane leaves the field vector unchanged. However for s-polarization the  $\mathbf{E}$  field is perpendicular to the mirror symmetry plane so that the symmetry operation changes  $\mathbf{E}$  into  $-\mathbf{E}$ . Details on how this can be done may be found in reference 6. Thus, the symmetric ( $A'$ ) eigenstates along the LU direction can only be excited by symmetric  $p$ -polarized incident fields, whereas the s-polarized fields can only couple with the anti-symmetric ( $A''$ ) states. So, a polarization sensitivity of the first Bragg peak width for oblique incidence is expected, according to band structure calculations.<sup>6</sup>

### 3. Angle resolved reflectivity

The samples employed in the experiments are artificial opals consisting of silica spheres 297 nm in diameter according to SEM characterization. The samples were grown by S. Rubio by natural sedimentation, and consist of an ordered fcc array, with the surface parallel to the  $\{111\}$  crystallographic planes. A detailed description of the synthesis can be found elsewhere.<sup>7</sup> A typical sample presents a surface of 9 mm<sup>2</sup> and a thickness of 0.5 mm. Reflectivity measurements were carried out using a configuration identical to that described in chapter 3. Angle resolved measurements were performed with linearly polarized light with its electric field perpendicular ( $s$ -polarization) or parallel ( $p$ -polarization) to the diffraction plane, as shown in Fig. 1. Reflectivity spectra for  $s$  and  $p$  polarized light as a function of angle are presented in fig. 2. In both cases, the shape of the spectra deviate from the flat top peaks with 100% reflectivity expected for perfect infinite crystals. Extinction caused by scattering taking place at defects in the bulk and surface of the crystal is known to affect the intensity and shape of the peak rounding the edges but not affecting the full width at half maximum (FWHM).<sup>8,9</sup> In the presence of a mosaic spread, beside an additional decrease in reflected intensity due to non specular reflections, inhomogeneous broadening could take place.<sup>10</sup> Another source of peak broadening could be the finite size of crystallites in the sample.<sup>11</sup> These issues will be discussed below, as a comparison with calculated bands is carried out. When comparing the spectra from figs. 2a and 2b a difference in the behaviour of the absolute reflectivity as a function of the angle of incidence is observed. While the spectra for  $s$ -polarized light show a nearly constant reflectivity with changes below 2% over the entire angular range, the spectra associated to the  $p$ -polarized light present a stronger decrease of nearly 6% in the same range. This difference will be addressed below. Two spectra for  $s$  and  $p$  polarized light, for an external angle of incidence  $\theta_{ext}$  of 39 degrees, are presented in fig. 2c. Both spectra have been normalized in intensity for comparison. Here we

can already appreciate the difference in width between both peaks, indicating strong polarization sensitivity.

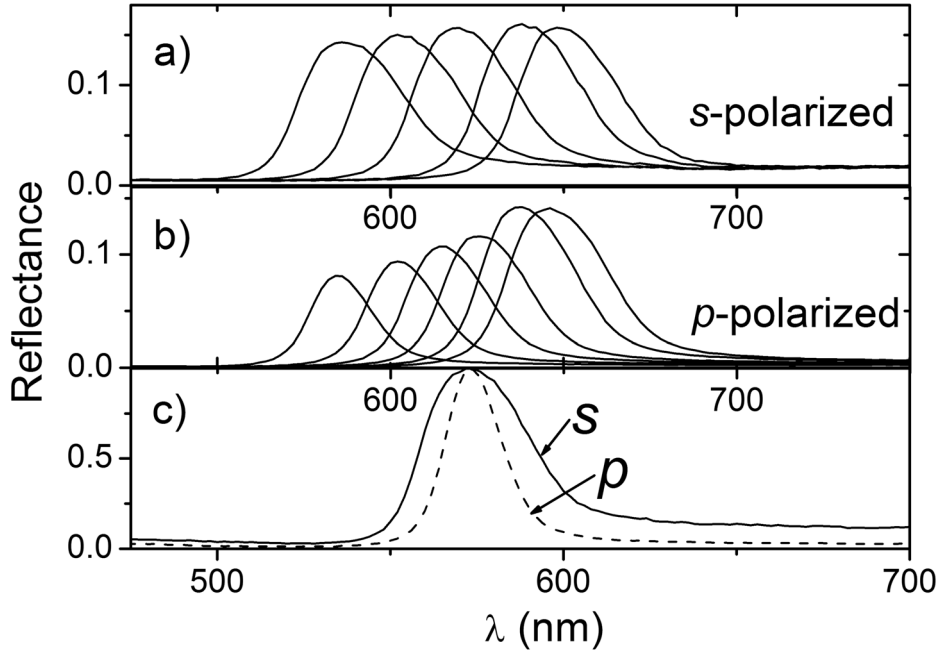


Figure 2: (a) Reflectivity spectra as a function of external angle of incidence for *s* polarized light for  $\theta_{\text{ext}} = 6^\circ, 14^\circ, 23^\circ, 29^\circ$  and  $34^\circ$ . (b) Reflectivity spectra as a function of external angle of incidence for *p* polarized light for  $\theta_{\text{ext}} = 8^\circ, 14^\circ, 21^\circ, 25^\circ, 30^\circ$  and  $35^\circ$ . (c) Normalized reflectivity spectra are shown in solid (dashed) line for *s*- (*p*-) polarized light, for an external angle of incidence of  $39^\circ$  degrees.

In order to compare our experimental results with numerical calculations,<sup>6</sup> several issues have been taken into account. Because of the geometry of the sample in our experiment we are mapping the bands for  $\mathbf{k}$  in the vicinity of the hexagonal face of the Brillouin zone (see fig. 1). As the angle of incidence increases, the wave vector  $\mathbf{k}$  will approach the boundaries of the hexagon centered in  $L$  in the direction of one of the high symmetry points located at the corners (W) and centers (U, K) of the sides of the hexagon. This will be determined by the orientation of the sample surface relative to the diffraction plane. For each possible orientation of the sample, different results are expected (see chapter 3).

Determining the orientation of the samples is not easy since they are composed by a mosaic of monodomains typically 20-50 microns in size.<sup>7</sup> While all domains show a preferential out-of-plane orientation with the surface consisting of  $\{111\}$  planes, they may present a random in-plane orientation. The size of the probe beam being larger than a typical domain will cause averaging over many domains. To avoid this uncertainty in our measurements, reflectivity spectra were collected from

normal incidence to an internal angle of 32 degrees. As pointed above, for this angular range the four lowest lying energy bands are identical irrespective of the direction of tilting. The correspondence between internal and external angles can be obtained from Snell's law using an effective refractive index  $n_{eff}$  which is calculated by fitting the experimental angle dependence to Bragg's law:

$$\lambda_{max} = 2d_{111}\sqrt{n_{eff}^2 - \sin^2\theta_{ext}},$$

where  $d_{111}$  is the interplanar distance for the (111)

family of planes (parallel to the crystal surface),  $\lambda_{max}$  is the peak center and  $\theta_{ext}$  is the angle formed by the normal to the crystal surface and the incident beam. This expression has proven valid for artificial opals<sup>12</sup> at angles below the avoided crossing region near the U, K and W points in the first Brillouin zone. The values obtained from this fit were:  $n_{eff}=1.336$  and  $d_{111}=244$  nm. If we estimate the diameter of the spheres from this value of  $d_{111}$  we obtain 299 nm, in agreement with the value obtained from SEM characterization.

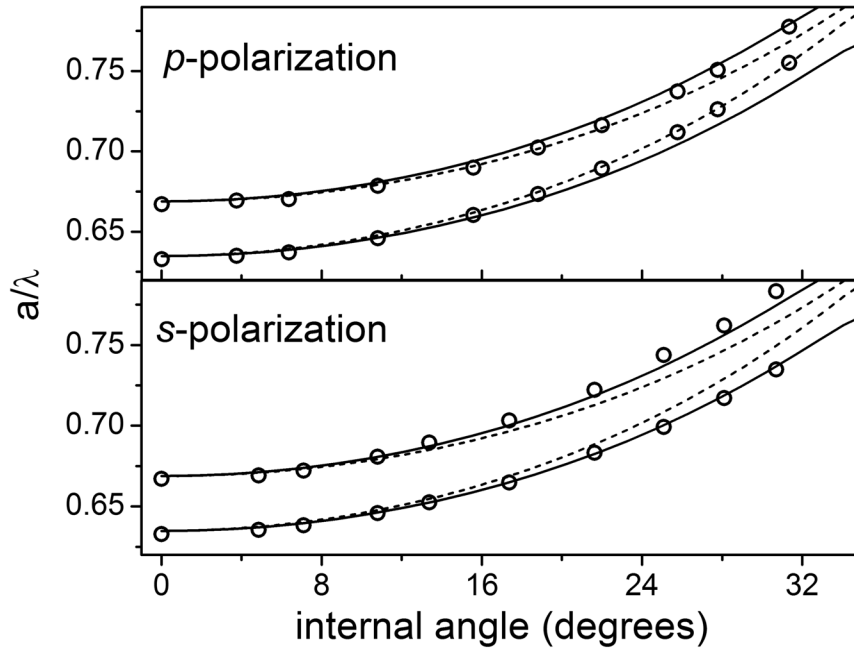


Figure 3: Calculated photonic bands (lines) and measured band edges from reflectance spectra (circles). Continuous (dashed) lines represent bands anti-symmetric (symmetric) with respect to mirror symmetry. Experimental data correspond to light plane polarized parallel (p) and perpendicular (s) to the diffraction plane.

We have assumed the widely used criterion of associating the full width at half maximum of reflectance peaks with the edges of a stop band to compare experimental reflectivity peaks with calculated bands. In the absence of finite size effects or mosaic spread, this approach would be correct as explained above. Following this criterion, fig. 3 shows the experimental results for p-polarized and s-

polarized light respectively (symbols), plotted on top of the calculated bands (lines). A fair agreement is observed in both cases. The fact that the FWHM of the peak for small angles of incidence matches with the predicted width implies that finite size effects are negligible and inhomogeneous broadening due to a mosaic spread, if present, will be small. As a matter of fact the broadening observed for large angles of incidence could be due to a mosaic spread, since its effect on the peak width would become more pronounced as the angle of incidence increases.<sup>13</sup> According to the previous analysis, the outer bands (1 and 4) couple to *s*-polarized light, while the inner bands (2 and 3), defining a narrower stop gap, couple to *p*-polarized light. This explains the difference in intensity for *s* and *p* polarized light reflectivity as a function of angle shown in fig. 2. In the case of *p*-polarized light, the stop band defined by the symmetric bands to which this polarization couples dramatically narrows as we move away from normal incidence, therefore the penetration length of the incident light into the crystal increases<sup>14</sup> and the effect of extinction by bulk defects will increase, while for *s*-polarized light the width of the stop band suffers a much smaller narrowing and therefore the change in intensity is smaller. Let us remark that in an experiment using unpolarized light, the outer bands would be probed while the inner ones would remain hidden since the broader peaks contain the narrower.

#### 4. Conclusions and future work

In this chapter we have presented angle and polarization resolved reflectivity from artificial opals, a system that, while not having a full photonic band gap, proves to be an interesting playground for studying the complex interaction of light with photonic crystals. It has been experimentally demonstrated that electromagnetic radiation with different polarization will only couple to certain energy bands depending on their symmetry character, in accordance with predictions based on group theory and previous results for related systems. From these results it is evident that the symmetry character of the photonic bands must be taken into account in order to properly interpret optical measurements.

Also for artificial opals it has been suggested<sup>15</sup> that a configuration in which to observe the effect of uncoupled modes in the optical response is to carry out normal incidence measurements for samples grown along the [220] crystallographic direction. Although artificial opals have a natural tendency to grow with the {111} planes parallel to the surface, alternative routes to obtain samples with their surface parallel to the {220} planes have been recently proposed.<sup>16,17</sup>

## 5. References

- <sup>1</sup> Robertson, W. M., *et al.* "Measurement of photonic band structure in a two-dimensional periodic dielectric array." *Physical Review Letters* **52**, 7982-7986 (1992).
- <sup>2</sup> Stefanou, N., Karathanos, V. and Modinos, A. "Scattering of Electromagnetic-Waves by Periodic Structures." *Journal of Physics-Condensed Matter* **4**, 7389-7400 (1992).
- <sup>3</sup> Sakoda, K. "Symmetry, degeneracy and uncoupled modes in two-dimensional photonic lattices." *Physical Review B* **52**, 7982-7986 (1995).
- <sup>4</sup> Tarhan, II and Watson, G. H. "Photonic band structure of fcc colloidal crystals." *Physical Review Letters* **76**, 315-318 (1996).
- <sup>5</sup> van Driel, H. M. and Vos, W. L. "Multiple Bragg wave coupling in photonic band-gap crystals." *Physical Review B* **62**, 9872-9875 (2000).
- <sup>6</sup> Lopez-Tejiera, F., Ochiai, T., Sakoda, K. and Sanchez-Dehesa, J. "Symmetry characterization of eigenstates in opal-based photonic crystals." *Physical Review B* **65**, art. no.-195110 (2002).
- <sup>7</sup> Mayoral, R., *et al.* "3D long-range ordering in an SiO<sub>2</sub> submicrometer-sphere sintered superstructure." *Advanced Materials* **9**, 257-260 (1997).
- <sup>8</sup> Thijssen, M. S., *et al.* "Inhibited light propagation and broadband reflection in photonic air-sphere crystals." *Physical Review Letters* **83**, 2730-2733 (1999).
- <sup>9</sup> van Driel, H. M. and Vos, W. L. "Multiple Bragg wave coupling in photonic band-gap crystals." *Physical Review B* **62**, 9872-9875 (2000).
- <sup>10</sup> Vlasov, Y. A., Deutsch, M. and Norris, D. J. "Single-domain spectroscopy of self-assembled photonic crystals." *Applied Physics Letters* **76**, 1627-1629 (2000).
- <sup>11</sup> Bertone, J. F., *et al.* "Thickness dependence of the optical properties of ordered silica-air and air-polymer photonic crystals." *Physical Review Letters* **83**, 300-303 (1999).
- <sup>12</sup> Miguez, H., *et al.* "Photonic crystal properties of packed submicrometric SiO<sub>2</sub> spheres." *Applied Physics Letters* **71**, 1148-1150 (1997).
- <sup>13</sup> Lopez, J. F. and Vos, W. L. "Angle-resolved reflectivity of single-domain photonic crystals: Effects of disorder." *Physical Review E* **66** (2002).
- <sup>14</sup> Y. Fink, J. N. Winn, S. Fann, C. Chen, J. Michel, J. D. Joannopoulos, and E. L. Thomas, *Science* **282**, 1679 (1998).
- <sup>15</sup> Lopez-Tejiera, F. "Una aproximación teórica a las propiedades fotónicas de los ópalos artificiales", PhD Thesis, Universidad Autónoma de Madrid (2004).
- <sup>16</sup> Palacios-Lidon, E., *et al.* "Optical study of the full photonic band gap in silicon inverse opals." *Applied Physics Letters* **81**, 4925-4927 (2002).
- <sup>17</sup> Matsuo, S., *et al.* "Formation of free-standing micropyrarnidal colloidal crystals grown on silicon substrate." *Applied Physics Letters* **82**, 4283-4285 (2003).



## CHAPTER 7

---

# Angle resolved reflectivity of single-domain photonic crystals: Effects of disorder

### 1. Introduction

When probing the optical properties of photonic crystals using coarse beams, with dimensions much larger than that of a typical domain, a comparison with theoretical predictions extracted from calculated bands may be a complex task. In the presence of a mosaic spread, each domain has  $\{111\}$  planes parallel to its surface, but its normal randomly oriented, and an inhomogeneous broadening of reflectance and transmittance peaks takes place.<sup>1,2</sup> Additional broadening may happen if different domains present different lattice parameters, its corresponding diffraction peaks being centered at different frequency. Besides this “strain”, finite size effects are also a source of broadening which may hamper comparison between experimental data and theoretical results.<sup>3,4</sup> Other forms of disorder such as grain boundaries, point defects, dislocations, etc. are likely to introduce diffuse scattering as light propagates through the crystal.

Therefore it makes sense to minimize any spectral or angular features in the reflection or transmission spectra due to disorder. In order to do so, one may want to probe only single domains. This has been demonstrated in opal based photonic crystals with a low refractive index contrast for normal incidence reflectance measurements where frequency was scanned.<sup>1</sup>

In this chapter we present angle-resolved reflectivity measurements with laser beams focused to a  $10\mu\text{m}$  spot for opal based photonic crystals consisting of air spheres in a titania ( $\text{TiO}_2$ ) backbone. As opposite to normal incidence frequency dependent measurements, which probe “vertical” slices of the band structure (fixed direction, variable frequency) the present measurements may be considered as probes of the dispersion surfaces. While on the former one may obtain information on stop bands, here information will be collected on angular and not spectral forbidden intervals. First we determine the orientation and size of crystal domains

present in the surface of the crystal which allows for assessment of mosaic spread and finite size effects on previous measurements using coarse white light beams. Then angle resolved measurements are performed and a comparison with theoretical predictions proves satisfactory. Finally the effects of diffuse scattering are modeled by a small imaginary component of the dielectric function.

## 2. Experimental

The experimental set-up used for these experiments is shown in figure 1.<sup>d</sup> Three laser beams with frequencies of 633 (He-Ne), 850 (diode) and 1064 nm (Nd:YVO<sub>4</sub>) were overlapped by a collection of beam splitters and modulated by a chopper. A telescope expands the beam which is then focused onto the sample. In order to combine a narrow focal spot of 10 $\mu$ m with a small angular aperture of 4 $^\circ$  full angle, microscope objectives were used with a focal length of 7.35 cm and a numerical aperture of 0.05 for both, focusing and detection.

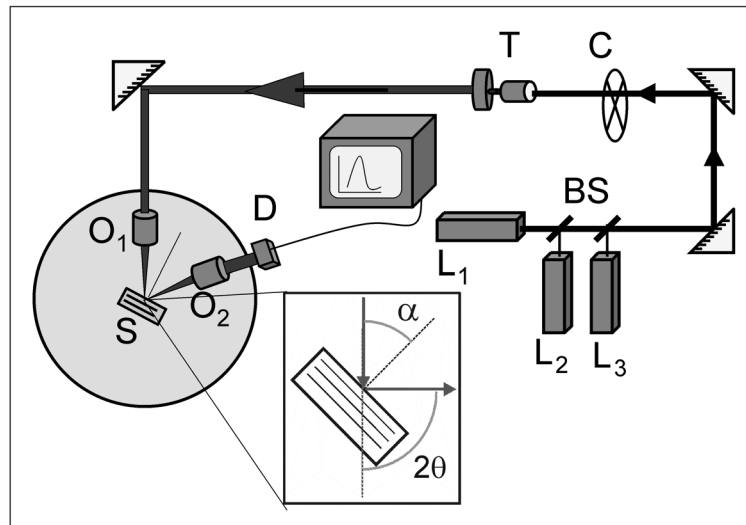


Figure 1: Scheme of experimental set-up. Beams from laser  $L_{1,2,3}$  (633, 850 and 1064 nm) are overlapped by beam splitters (BS). The resulting beam passes through a chopper (C) that is connected to a lock-in amplifier, and is expanded by a telescope (T). The microscope objective  $O_1$  focuses the beam on to the sample, and  $O_2$  collects diffracted light. In the inset,  $\alpha$  and  $2\theta$  are defined as the angles that the incident beam forms with the normal to the surface and the diffracted beam respectively.

<sup>d</sup> Experimental measurements were performed at the laboratories of the group Waves in Complex Media in the van der Waals-Zeeman Institute (University of Amsterdam, The Netherlands).

The sample lies on the  $\alpha$  rotation stage, where  $\alpha$  is the angle between the incident beam and the sample normal (figure 1). The detection system consisting of a microscope objective and a diode detector is placed on a separate  $2\theta$  stage, with the same rotation axis as  $\alpha$ ;  $2\theta$  is defined as the angle between the incident and the diffracted beams. Due to physical limitations imposed by the size of the objective holders, the angular range of collection is reduced to the interval  $20^\circ < 2\theta < 120^\circ$ . An additional beam splitter is located before the focusing objective to allow for normal incidence collection at  $2\theta = 180^\circ$ .

The samples studied consist of a FCC array of air holes in a  $\text{TiO}_2$  matrix.<sup>5,6</sup> Several are the same as those in references 7, 8 and 9. They have overall dimensions of  $1 \text{ mm}^2$  parallel to the surface, and a thickness of  $\sim 200 \text{ }\mu\text{m}$ . We have employed samples of lattice parameters  $847 \pm 5$  and  $477 \pm 14$  nm with several wavelengths in order to measure reflectivity over a wide spectral range in terms of the reduced frequency  $a/\lambda$ , where  $a$  is the lattice parameter and  $\lambda$  is the wavelength of light in vacuum. For the samples and wavelengths used, we achieved values of  $a/\lambda = 0.754 \pm 0.002$ ,  $0.796 \pm 0.005$ , and  $0.996 \pm 0.006$ . For these values, we will probe inside the stop gap associated with the (111) Bragg diffraction, centered at  $a/\lambda = 0.73$  at normal incidence, as well as below and above the centre of the avoided crossing of multiple Bragg diffraction taking place at the U-point for  $a/\lambda = 0.85$ .<sup>9</sup> For FCC photonic crystals band degeneracy can take place near the U point, narrowing the stop gap for p-polarized light.<sup>10</sup> In order to avoid this, s-polarized light has been used in all our measurements.

### 3. Determination of mosaic spread

We have measured reflectivity for different orientations  $\alpha$  of the sample while maintaining the detector at a fixed position  $2\theta$  chosen so that the wavelength used is inside the stop gap for that orientation. By doing this we obtain information about the orientation of the different domains constituting the surface. Domains with different orientations will show reflectivity maxima centered at different sample angle  $\alpha$ . We have measured reflectivity systematically in this way over the whole surface of the crystals, dividing the surface in a two dimensional grid consisting of points separated by  $200 \text{ }\mu\text{m}$ . In Fig. 2 normal incidence reflectivity results are shown for a sample with a lattice parameter  $a = 477$  nm using a wavelength  $\lambda = 633$  nm, which for this sample is contained in the L-pseudogap, that is, the stop gap for incidence normal to the  $\{111\}$  family of lattice planes. We observe three curves corresponding to measurements done on three different domains. Each curve shows an angular aperture equal to that of the reference measurement carried out with the mirror. Reflectivity as high as 94% has been found, confirming that good quality single crystals are being probed. From the position of the peaks, a mosaic spread of  $\pm 2^\circ$  can be deduced. Similar measurements were carried out for a sample with a lattice parameter of 847 nm at a wavelength of 1064 nm, only that  $\alpha$  was increased to  $30^\circ$  in order to be at the center

of the stop gap. A reflectivity up to 77% and a mosaic spread of  $\pm 3^\circ$  were recorded. For measurements performed on similar samples, but using coarse beams ( $\sim 600 \mu\text{m}$ ), reflectivities as low as 20% and 8% were reported for normal incidence and  $\alpha = 30^\circ$  respectively.<sup>7</sup> Therefore probing such small regions offers further information about crystal quality and optical performance which remains hidden when using coarse beams.

In both sets of measurements, domains as large as  $L = 200 \mu\text{m}$  were found, by selecting two points from the grid with the same orientation, repeating the measurements for intermediate points, and observing high reflectivity. A broadening of the peak due to finite size effects would then be negligible (see chapter 3). Out of these domains, regions presenting rather low reflectivity ( $\sim 10\%$ ) were found. This would explain the low signal collected in previous measurements using coarse beams.<sup>7,9</sup> A possible reason for such low reflectivity regions could be the existence of zones covered with unstructured  $\text{TiO}_2$ .<sup>5</sup>

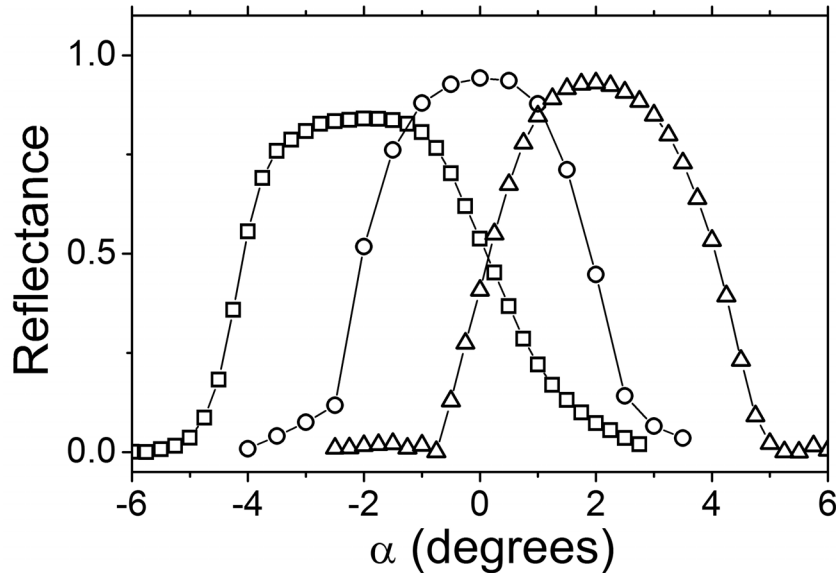


Figure 2: Reflectivity for  $a/\lambda = 0.754 \pm 0.002$  ( $a = 477 \pm 14 \text{nm}$ ,  $\lambda = 633 \text{nm}$ ), measured as a function of  $\alpha$  at different points on the sample surface. The  $2\theta$  detection stage remains fixed at normal incidence ( $2\theta = 180^\circ$ ).

In coarse beam experiments, where many domains are probed simultaneously, the inhomogeneous broadening introduced by the mosaic spread will increase with the angle of incidence due to the shape of energy bands. It can be estimated that the relative broadenings introduced due to the mosaic spread would range from 1.5% at normal incidence to 8% for an angle of incidence of  $60^\circ$ .<sup>7</sup>

#### 4. Angle resolved reflectivity

When trying to measure single-domain angle-resolved reflectivity, the beam must be carefully aligned with the rotation axis. Any misalignment will cause a translation of the region of the sample exposed to the beams, as well as bringing it out of focus as the sample is rotated. We found that the detection optics on the  $2\theta$  stage must be carefully counterweighted to avoid tilting of the rotation axis which also moves the sample out of focus. The counterweight process is done by observing the diffraction pattern of a  $10\ \mu\text{m}$  thick tungsten wire located at the sample holder as the  $2\theta$  stage is rotated. The evolution of the pattern is observed for different positions of the counterweight. An alignment is achieved such that the wire moves less than  $10\ \mu\text{m}$  from its original position over the whole angular range as is shown in Fig. 3. This result shows that it is feasible to carry out angle resolved scans on objects, including single crystals, of  $10\ \mu\text{m}$  dimensions.

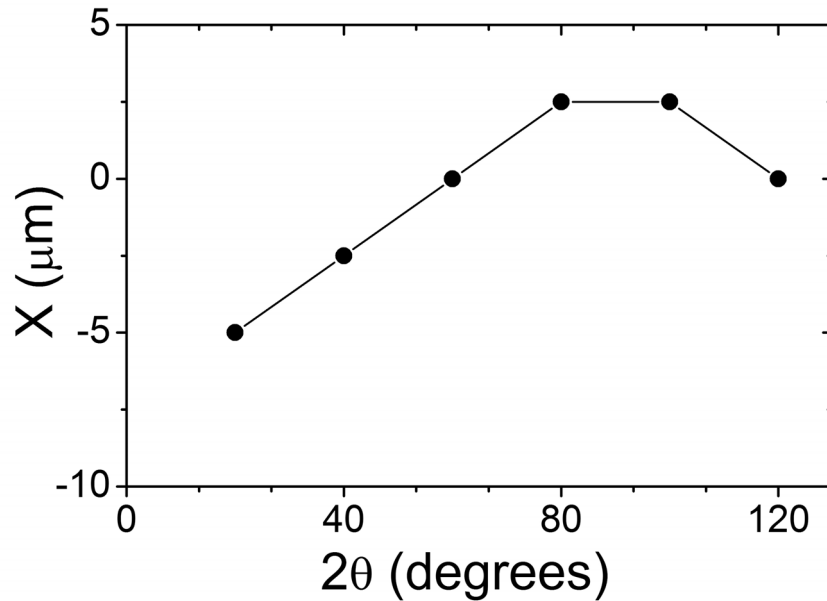


Figure 3: Measured position of the rotation center of the  $\alpha$  stage as a function of the angle rotated by the  $2\theta$  stage (circles, connected by lines). An overall change of less than  $10\ \mu\text{m}$  is observed.

For the sample with  $a = 847\ \text{nm}$ , angle resolved reflectivity measurements were carried out for the frequencies  $a/\lambda = 0.796$  and  $0.996$ . The results are shown in Fig. 4. The excluded angular range due to experimental limitations imposed by the set-up is indicated as a crossed block. We see peaks that correspond to those directions where the stop gap contains the frequencies used. For  $a/\lambda = 0.796$  we observe a peak centered at  $\alpha = 30^\circ$  and showing a half width at half maximum of  $13.2^\circ$ , and a reflectivity of 77%. The peak associated with  $a/\lambda = 0.996$  is centered at

$\alpha = 54^\circ$  and has a half width at half maximum of  $10^\circ$  and up to 39% reflectivity. The shape of the peaks deviate from the flat-top predicted for perfect crystals by the dynamical diffraction theory which models similar measurements in x-ray diffraction<sup>11</sup> and colloidal crystal research.<sup>12</sup> In this theory the rounded top shown by our peaks is associated with extinction, which in our case can only come from diffuse scattering by defects, since for the range of wavelengths that we are using  $\text{TiO}_2$  does not absorb.<sup>6</sup> We can also see that as the reflectivity peak appears at larger angles, the reflected intensity decreases. This cannot come from any misalignment of the beam with respect to the rotation centre, since in the reference measurements taken with the mirror, a signal constant within 5% was recorded at all angles. It is conceivable that diffracted energy is carried away by multiple Bragg diffraction (in directions which may not be collected with the present configuration) discussed below, which warrants further study.

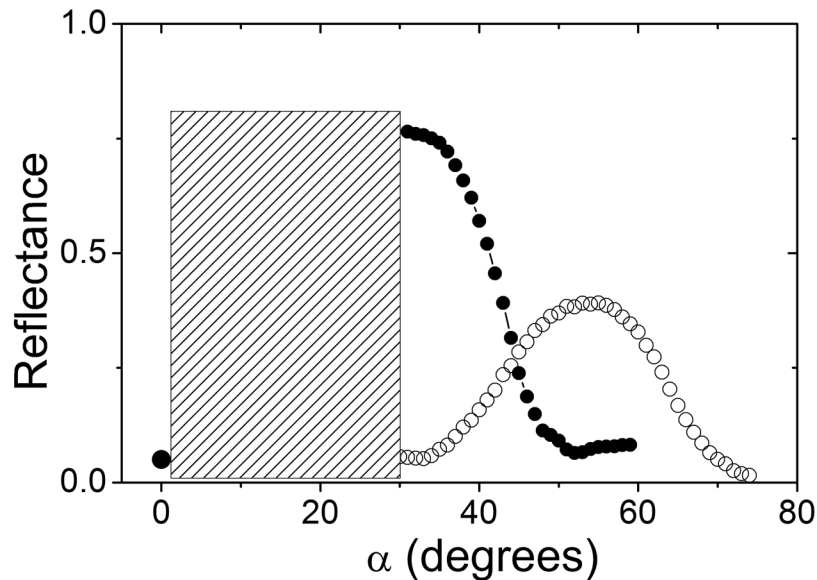


Figure 4: Angle-resolved reflectivity on the sample with  $a = 847 \text{ nm}$  for  $a/\lambda = 0.796$  (solid circles:  $\lambda=1064 \text{ nm}$ ) and  $a/\lambda = 0.996$  (open circles:  $\lambda=850 \text{ nm}$ ) as a function of  $\alpha$ . The collection is done at  $2\theta=180-2\alpha$  for every  $\alpha$ . The hatched rectangle indicates the angular range excluded due to physical limitations in the set-up.

To obtain the range where stop gaps are present, we have used the heuristic but reliable criterion (see chapter 3) that the full width at half maximum of a reflectivity peak corresponds to a stop gap. Data obtained in this way are plotted in figure 5. The single point at normal incidence corresponds to the measurements done at relative frequency  $a/\lambda = 0.754$ , see Fig. 3. The hatched line at  $a/\lambda = 0.796$  is our estimation of the fraction of the stop gap falling within the forbidden angular range. At  $a/\lambda = 0.996$  two peaks centered at different angles were obtained in separate domains. This is probably due to strain which, in this sort of crystals may

happen as an uneven shrinkage of the original opal skeleton during calcination. Mosaic spread is not likely to be the reason for these two peaks, since each domain was properly oriented with respect to the incident beam by measurements similar to those shown in Fig. 3. The peaks are plotted together with error bars indicating the uncertainty in the width.

The triangles in Fig. 5 indicate previous measurements with coarse beams.<sup>9</sup> For the relative frequency  $a/\lambda = 0.796$ , a good agreement is observed between the two measurements. At  $a/\lambda = 0.996$ , the results obtained with coarse beams show a broader stop gap than that obtained with a focused beam. A reason for this deviation could be that for measurements with focused beams, realignment is carried out for each domain as described above, in order to avoid any inhomogeneous broadening due to mosaic spread. But for the case of coarse beams many domains are probed simultaneously, making it impossible to realign each of them and therefore introducing inhomogeneous broadening, which for this angular range can reach values up to 8% in frequency as discussed above.

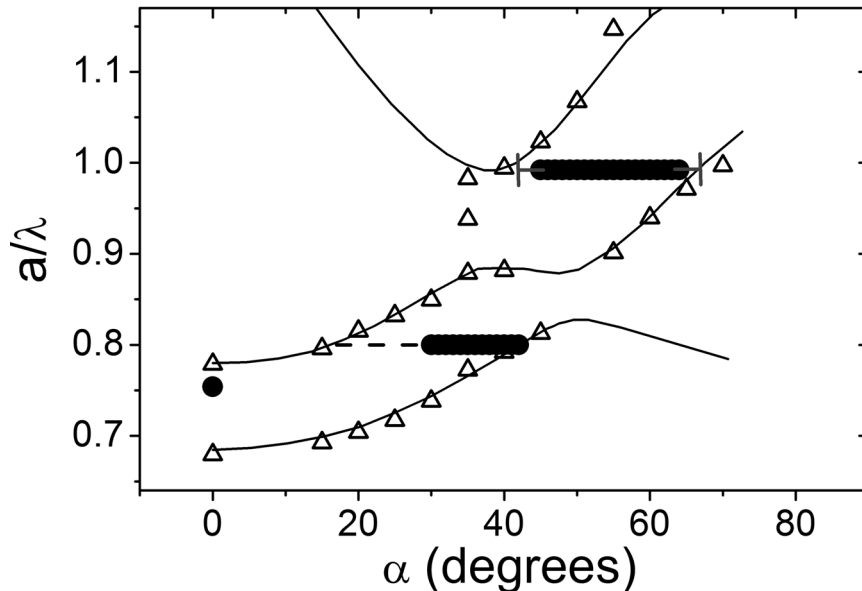


Figure 5: Comparison of present angle-resolved measurements (solid circles) with previous measurements using coarse beams (open triangles) and theoretical predictions (solid lines).

The drawn curves in Fig. 5 are photonic bands calculated with the plane wave expansion using a dielectric model described in Refs. 8 and 9. For normal incidence this model reveals diffraction by only the  $\{111\}$  family of planes taking place. As the angle of incidence increases we move along the surface of the Brillouin zone in reciprocal space. As we reach the U point,<sup>13</sup> diffraction from the  $\{111\}$  and  $\{200\}$  families of planes will take place simultaneously resulting in band repulsion of Bloch states.<sup>9</sup> The fact that many waves couple, will cause a deviation of the dispersion relation from simple Bragg behavior, thereby flattening the photonic bands, a requirement for the formation of a photonic band gap. As

shown in Fig. 5, the relative frequencies we have used in our experiments fall above and below the avoided crossing, and show good agreement with the calculated bands. Any attempt to explain similar results with a model based on simple Bragg diffraction will therefore lead to systematic errors.

## 5. Effects of disorder

To theoretically interpret our results at normal incidence, we have performed calculations using the so-called scalar wave approximation (SWA), that is, using the plane-wave expansion in the E-field formulation and retaining only two reciprocal lattice vectors.<sup>14,15</sup> We have extended the model to include extinction as a result of scattering from crystal imperfections. The two reciprocal lattice vectors correspond to the incident wave  $hkl = 000$ , and the diffracted wave  $hkl = 111$ . The Fourier components of the dielectric function are derived from the model described in Refs. 7 and 8, that accurately mimic the structure of our crystals, and whose dispersion relations agree well with reflectivity experiments. The following values were employed:  $\epsilon'_{000} = 1.643$  and  $\epsilon_{111} = -0.187961$ . We take extinction due to diffuse scattering (by for instance point defects and grain boundaries) into account by a complex component of the average dielectric constant of the crystal  $\epsilon''_{000}$ , which corresponds to a uniform extinction throughout the crystal. Note that this is different from the situation in x-ray diffraction, where absorption can only be present at the positions of atoms and the extinction is thus spatially modulated.<sup>11,16</sup>

Figure 6 (inset) shows a calculated reflectivity curve as a function of frequency. While we have not measured such a frequency dependence, we can nevertheless compare the reflectivity measured at normal incidence (see figure 2) to the maximum  $R_{max}$  of the calculated peak. The dashed curve in Fig. 6 shows  $R_{max}$  as a function of the number of lattice planes in the absence of extinction, that is, with a purely real  $\epsilon'_{000}$ . It is seen that  $R_{max}$  strongly increases before saturating at near unity for more than 20 planes. The solid curve in Fig. 6 shows  $R_{max}$  for a 40 plane crystal as a function of the extinction length expressed in the number of layers, that is, for increasing  $\epsilon'_{000}$ . It is seen that the maximum reflectivity increases with extinction length. From the difference between  $R_{max}$  versus structure thickness in otherwise perfect crystals (dashed) and  $R_{max}$  versus  $l_{ext}$  (drawn), it is obvious that reflectivity in presence of extinction *cannot* be simply regarded as reflectivity from a crystal with finite thickness. For an  $l_{ext}$  between 65 and 170 planes, we obtain a maximum reflectivity of  $94 \pm 3$  % as observed in the present experiment (Fig. 2). Such an extinction length compares favorably with mean free paths of 10 to 20  $\mu\text{m}$  or 60 layers, that were measured earlier by Koenderink *et. al.*<sup>17</sup> The extinction length corresponds to a small ratio between the imaginary and real components of the dielectric function of  $\epsilon''_{000}/\epsilon'_{000}=0.0035$ . It is interesting to consider how long an extinction length is required to obtain a maximum reflectivity of 99.99%, that is necessary for mirrors surrounding high-Q cavities. For a crystal with a thickness larger than 20 layers, the calculated  $l_{ext}$  to obtain such a reflectivity is of the order

of  $10^4$  layers, which would require considerable improvements of all current fabrication techniques.<sup>18</sup>

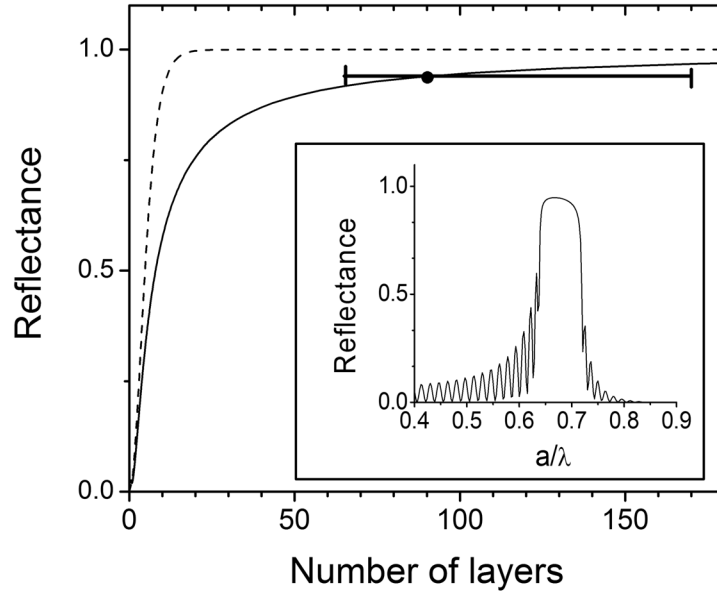


Figure 6: The dotted line shows the maximum reflected intensity  $R_{max}$  as a function of the crystal thickness. The solid line represents  $R_{max}$  as a function of the extinction length  $l_{ext}$  for a 40-layer thick crystal. Error bars indicate the  $l_{ext}$  range that accounts for the reflectivity we observe experimentally. Inset: calculated reflectivity spectrum at normal incidence for a crystal in the presence of extinction.

Although the introduction of a complex component of the dielectric constant has been used in trying to account for disorder in 3D crystals,<sup>19,20</sup> information obtained from this approach is mainly of heuristic value. In this simple model we have not taken into account many factors which have been demonstrated to influence light propagation in disordered photonic crystals such as the band structure for directions adjacent to the incident one (see chapter 3).

## 6. Conclusions and future work

We have measured angle-resolved reflectivity with laser beams focused to within single domains. Special care has been taken to assure an alignment of the waist of the beam with the axis of rotation to a precision of  $10\ \mu\text{m}$ . This technique proves valid to carry out reflectivity measurements on samples of  $10\ \mu\text{m}$  in dimensions. We have observed high reflectivities up to 94% at normal incidence, much larger than previous measurements performed on the same samples with coarse beams. This value decreases for larger angles of incidence, a behavior not

understood at this time. Evidence has been found for small inhomogeneous broadening present in previous measurements with coarse beams, due to the presence of a mosaic spread of  $\pm 3^\circ$ , and finite size effects are found to be negligible. This technique opens an exciting opportunity to study light propagation in a photonic single crystal for any direction through the determination of the group velocity and the group velocity dispersion using pulsed laser beams, which has only been done for normal incidence. With suitable tunable laser sources, this method proves ideal to fully characterize dispersion surfaces of any photonic crystal. These measurements have given us valuable *in situ* information about the structure of the surface of our crystals, which complements that obtained from optical and scanning electron microscopy.

## 7. References

---

- <sup>1</sup> Vlasov, Y. A., Deutsch, M. and Norris, D. J. “*Single-domain spectroscopy of self-assembled photonic crystals.*” *Applied Physics Letters* **76**, 1627-1629 (2000).
- <sup>2</sup> Astratov, V. N., *et al.* “*Interplay of order and disorder in the optical properties of opal photonic crystals.*” *Physical Review B* **66** (2002).
- <sup>3</sup> Bertone, J. F., *et al.* “*Thickness dependence of the optical properties of ordered silica-air and air-polymer photonic crystals.*” *Physical Review Letters* **83**, 300-303 (1999).
- <sup>4</sup> Galisteo-Lopez, J. F., Palacios-Lidon, E., Castillo-Martinez, E. and Lopez, C. “*Optical study of the pseudogap in thickness and orientation controlled artificial opals.*” *Physical Review B* **68**, art. no.-115109 (2003).
- <sup>5</sup> Wijnhoven, J. and Vos, W. L. “*Preparation of photonic crystals made of air spheres in titania.*” *Science* **281**, 802-804 (1998).
- <sup>6</sup> Wijnhoven, J., Bechger, L. and Vos, W. L. “*Fabrication and characterization of large macroporous photonic crystals in titania.*” *Chemistry of Materials* **13**, 4486-4499 (2001).
- <sup>7</sup> Thijssen, M. S., *et al.* “*Inhibited light propagation and broadband reflection in photonic air-sphere crystals.*” *Physical Review Letters* **83**, 2730-2733 (1999).
- <sup>8</sup> Vos, W. L. and van Driel, H. M. “*Higher order Bragg diffraction by strongly photonic fcc crystals: onset of a photonic bandgap.*” *Physics Letters A* **272**, 101-106 (2000).
- <sup>9</sup> van Driel, H. M. and Vos, W. L. “*Multiple Bragg wave coupling in photonic band-gap crystals.*” *Physical Review B* **62**, 9872-9875 (2000).
- <sup>10</sup> Ho, K. M., Chan, C. T. and Soukoulis, C. M. “*Existence of a Photonic Gap in Periodic Dielectric Structures.*” *Physical Review Letters* **65**, 3152-3155 (1990).
- <sup>11</sup> Zachariassen W. H. “*Theory of X-Ray diffraction in crystals*”, Wiley, New York (1945).
- <sup>12</sup> Spry, R. J. and Kosan, D. J. “*Theoretical analysis of the crystalline colloidal array filter.*” *Applied Spectroscopy* **40**, 782-784. (1986).
- <sup>13</sup> Sample orientation for these samples was done in reference 6 by means of small angle x-ray scattering (SAXS).
- <sup>14</sup> Shung, K. W. K. and Tsai, Y. C. “*Surface Effects and Band Measurements in Photonic Crystals.*” *Physical Review B* **48**, 11265-11269 (1993).
- <sup>15</sup> Mittleman, D. M., *et al.* “*Optical properties of planar colloidal crystals: Dynamical diffraction and the scalar wave approximation.*” *Journal of Chemical Physics* **111**, 345-354 (1999).
- <sup>16</sup> James, R. W. “*The optical principles of the diffraction of X-Rays*”, Bell, London (1954) .
- <sup>17</sup> Koenderink, A. F., *et al.* “*Enhanced backscattering from photonic crystals.*” *Physics Letters A* **268**, 104-111 (2000).
- <sup>18</sup> Koenderink, A. F. and Vos, W. L., “*Optical loss due to intrinsic structural variations of photonic crystals*”, <http://arxiv.org/abs/physics/0406052>.

- 
- <sup>19</sup> Allard, M., Sargent, E. H., Kumacheva, E. and Kalinina, O. “*Characterization of internal order of colloidal crystals by optical diffraction.*” *Optical and Quantum Electronics* **34**, 27-36 (2002).
- <sup>20</sup> Deubel, M., *et al.* “*Direct laser writing of three-dimensional photonic-crystal templates for telecommunications.*” *Nature Materials* **3**, 444-447 (2004).

## Appendix 1

---

### Photonic band structures for opal based systems: PWEM vs. SWA

The SWA in the two-band model<sup>1</sup> is a simplification of the plane wave expansion (PWE) method outlined in chapter 1 which allows obtaining an analytical expression for the dispersion relation  $k(\omega)$  of a photonic crystal. In this way one can obtain valuable information regarding the optical performance of the crystal without turning to numerical calculations.

The model is based on two approximations. The first one is to ignore the vectorial character of the problem. In doing so one expects the obtained results to better reproduce the exact solution for high symmetry directions. This is in principle valid for some systems such as artificial opals, for which the growth process yields samples with the surface oriented along the (111) direction, and therefore the most accessible direction for optical probing is a high symmetry one.

The second approximation is to consider that in the spectral range of interest the Bragg condition is satisfied only for one family of planes. One may then retain only two terms in the expansions of the fields and the dielectric constant, corresponding to the incident beam and the diffracted one. This should apply to the low energy region in the case of artificial opals where the frequency considered only meets the first order Bragg condition for the family of planes parallel to the surface.

After taking these approximations, the wave vector as a function of frequency is obtained by solving a set of two equations:

$$\left[ k^2 - \epsilon_0 \frac{\omega^2}{c^2} \right] c_k = \frac{\omega^2}{c^2} \epsilon_G c_{k-G}$$

$$\left[ (k-G)^2 - \varepsilon_0 \frac{\omega^2}{c^2} \right] c_{k-G} = \frac{\omega^2}{c^2} \varepsilon_G c_k$$

where  $(\varepsilon_0, \varepsilon_G)$  and  $(c_k, c_{k-G})$  are the first two Fourier coefficients in the expansions of the dielectric constant and the electric field respectively. Here  $\varepsilon_0$  is the average dielectric constant and  $\varepsilon_G$  is given by:<sup>1</sup>

$$\varepsilon_G = 3f(\varepsilon_a - \varepsilon_b) \frac{\sin(GR) - GR \cos(GR)}{(GR)^3}$$

where  $f$  is the volume fraction of the spheres,  $R$  its radius,  $G$  the considered reciprocal lattice vector (in the particular case of normal incidence on artificial opals  $G_{111}$  is used) and  $\varepsilon_a$  and  $\varepsilon_b$  the dielectric constant of the spheres and air respectively.

Having an analytical expression for the dispersion relation one can define the fields  $E_1$  (incident on the sample),  $E_2$  (inside the sample) and  $E_3$  (transmitted):<sup>1</sup>

$$\begin{aligned} E_1 &= e^{ik_0x} + r e^{-ik_0x} \\ E_2 &= c_1(e^{ikx} + A e^{i(k-G)x}) + c_2(e^{-ikx} + A e^{-i(k-G)x}) \\ E_3 &= t e^{ik_0x} \end{aligned}$$

where  $r$  and  $t$  are the reflectance and transmittance, and  $A$  is the amplitude ratio between the incident and the diffracted wave inside the crystal. One can then obtain expressions for  $r$  and  $t$  by imposing the continuity of the electric field and its derivative at both sample interfaces.

The SWA in the two-band model approach has proven to be a valuable tool when modelling the optical properties of opal-based systems with a low refractive index contrast.<sup>2-6</sup> Further, some authors<sup>7</sup> have even used it to predict the conditions (regarding refractive index contrast and filling fractions) under which the relative width  $\Delta\omega/\omega_c$  of the pseudogap at the L and X points (and their overlapping) are optimized.

The predictions obtained with this approach were compared<sup>8</sup> with those obtained from other popular analytical approach for the study of colloidal crystals, the dynamical diffraction theory (DDT) borrowed from x-ray research.<sup>9</sup> In that study it was found that SWA yielded the same results as DDT in the limit of low refractive index contrast. But to date no comparison has been performed between the predictions of this approach and those of the exact PWEM (save from a result presented in reference 6 in which the relative width  $\Delta\omega/\omega_c$  predicted by SWA and PWEM for a Yablonovite structure was presented as a function of filling fraction). This comparison will ultimately show the validity of this approach in treating opal based photonic crystals. Here we concentrate on the evolution of the results of both approaches as we increase the refractive index contrast of an FCC crystal containing touching dielectric spheres in a dielectric medium with a different refractive index. The study is performed for two systems of interest; dielectric

spheres in air and air spheres in a dielectric background. The evolution of several parameters describing the pseudogap at the L point (the most accessible one for artificial opals) is presented in figure 1. These include the pseudogap high and low frequency edges, its relative width and centre frequency.

From figure 1 it can be seen that in the case of inverse opals, exact (PWEM) and approximated (SWA) predictions present an excellent agreement for low refractive index contrast in the range of 1-1.6 where materials of interest (such as silica and several polymers) are found. For the direct opal, this agreement is moderately good, and the refractive index range where most polymers are found ( $\sim 1.6$ ) is just on the limit where exact results begin to diverge from approximated ones. For the case of high refractive index materials such as silicon or gallium arsenide (necessary for opening a complete PBG in inverse structures), the disagreement becomes more pronounced.

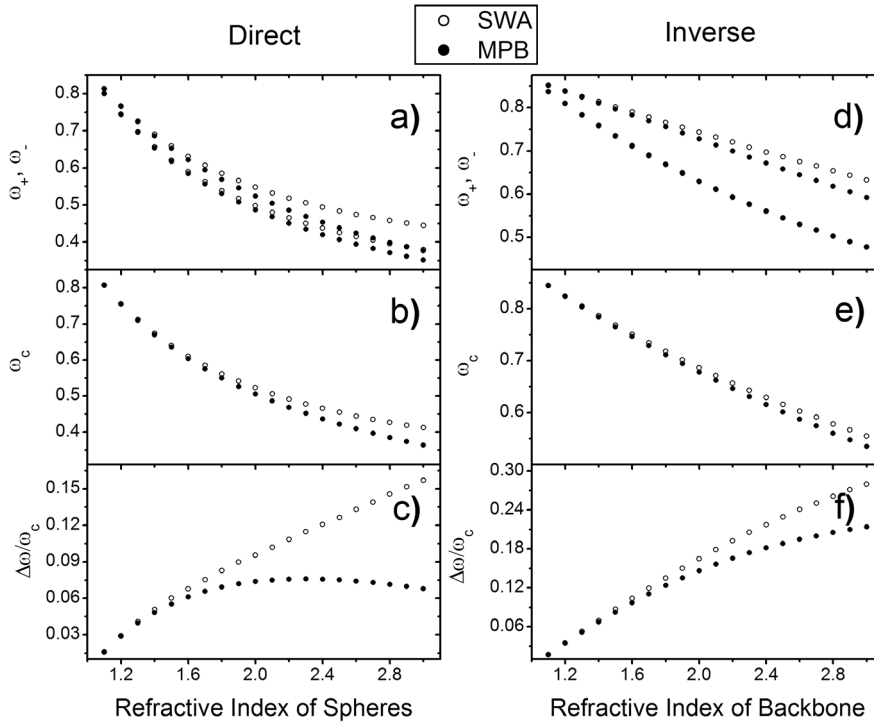


Figure 1: Evolution of the pseudogap edges ( $\omega_+$ ,  $\omega_-$ ), centre ( $\omega_c$ ) and relative width ( $\Delta\omega/\omega_c$ ) as a function of refractive index for a direct (a, b and c respectively) and an inverse (d, e and f respectively) opal based photonic crystals. All expressed in reduced frequency units  $a/\lambda$ .

This disagreement is probably due to the fact that in this version of the SWA only two reciprocal lattice vectors are considered, so the effect of bands associated with other families of planes is neglected. The effect of these bands becomes more pronounced for high refractive index contrasts, as evidenced in figure 2. Here band

structures (calculated with the PWEM and SWA) for direct opals with increasing refractive index of the spheres are shown. With increasing refractive index contrast, a stronger mode coupling takes place which is clearly not well described by the SWA. In this approach the bands defining the pseudogap follow an effective medium behavior (linear bands) with a gap at the edge of the Brillouin zone due to Bragg diffraction by the  $\{111\}$  family of planes. On the other hand, bands calculated with the PWEM start to deviate from the linear behavior and shift to lower energies as high energy band degeneracies are lifted and begin to flatten. For the case of a direct opal and a refractive index of  $n_{\text{sph}}=2.9$ , the pseudogaps obtained by both approaches barely overlap.

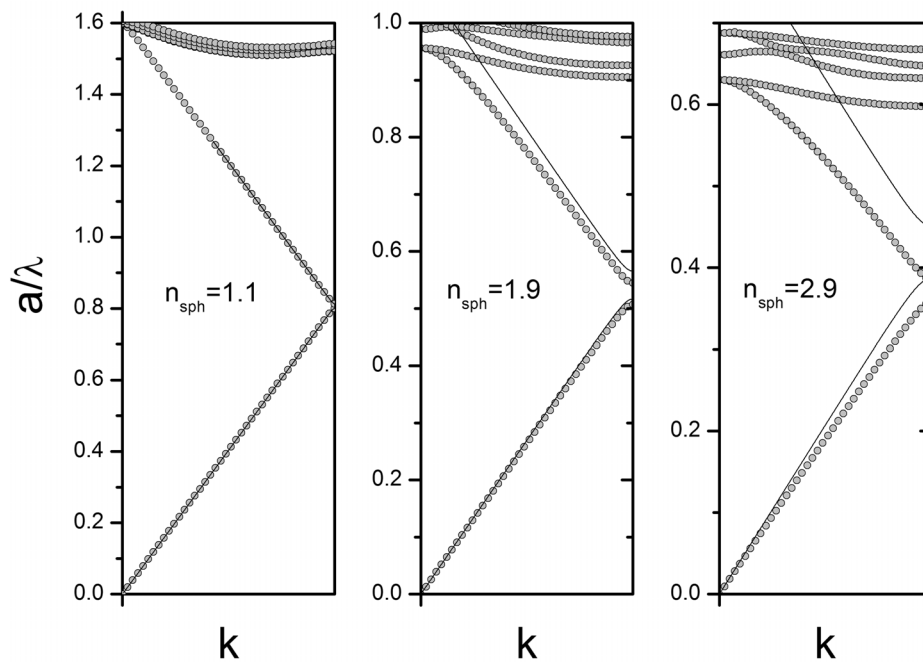


Figure 2: Band structures for wave vectors parallel to the  $\Gamma L$  direction calculated with the PWEM (open circles) and SWA (solid lines) for direct opals consisting of spheres with refractive index 1.1 (a), 1.9 (b) and 2.9 (c).

- 
- <sup>1</sup> Shung, K. W. K. and Tsai, Y. C. “Surface Effects and Band Measurements in Photonic Crystals.” *Physical Review B* **48**, 11265-11269 (1993).
- <sup>2</sup> Bertone, J. F., et al. “Thickness dependence of the optical properties of ordered silica-air and air-polymer photonic crystals.” *Physical Review Letters* **83**, 300-303 (1999).
- <sup>3</sup> Vlasov, Y. A., Deutsch, M. and Norris, D. J. “Single-domain spectroscopy of self-assembled photonic crystals.” *Applied Physics Letters* **76**, 1627-1629 (2000).

- 
- <sup>4</sup> Miguez, H., Yang, S. M. and Ozin, G. A. "Colloidal photonic crystal microchannel array with periodically modulated thickness." *Applied Physics Letters* **81**, 2493-2495 (2002).
- <sup>5</sup> Galisteo-Lopez, J. F., Palacios-Lidon, E., Castillo-Martinez, E. and Lopez, C. "Optical study of the pseudogap in thickness and orientation controlled artificial opals." *Physical Review B* **68**, art. no.-115109 (2003).
- <sup>6</sup> Tetreault, N., *et al.* "Dielectric planar defects in colloidal photonic crystal films." *Advanced Materials* **16**, 346-349 (2004).
- <sup>7</sup> Tarhan, II and Watson, G. H. "Analytical expression for the optimized stop bands of fcc photonic crystals in the scalar-wave approximation." *Physical Review B* **54**, 7593-7597 (1996).
- <sup>8</sup> Mittleman, D. M., *et al.* "Optical properties of planar colloidal crystals: Dynamical diffraction and the scalar wave approximation." *Journal of Chemical Physics* **111**, 345-354 (1999).
- <sup>9</sup> Zachariassen, W. H. "Theory of x-ray diffraction in crystals", Wiley, New York (1945).



## Appendix 2

### INFILTRATION OF POLYSTYRENE THIN FILM OPALS WITH $\text{SiO}_2$

$\text{SiO}_2$  infiltration in thin film opals was performed following a chemical vapour deposition method originally proposed by Míguez and co-workers.<sup>1</sup> The experimental set-up employed (see figure 1) has been thoroughly described elsewhere.<sup>2</sup> The two reactants,  $\text{SiCl}_4$  and doubly distilled water (DDW), are alternatively transported by a  $\text{N}_2$  flow from two separate bubblers. The stream carries the vapour phases to the reactor containing the sample.

In a typical procedure DDW is bubbled at a  $\text{N}_2$  flow of 200 mL/min in a pre-treatment step in order to moisten the reactor for 30 seconds. After that, the sample is placed in the reactor and water is again bubbled during a period of 30 seconds (200 mL/min  $\text{N}_2$  flow). By doing this, a water layer is deposited on the surface of the spheres.

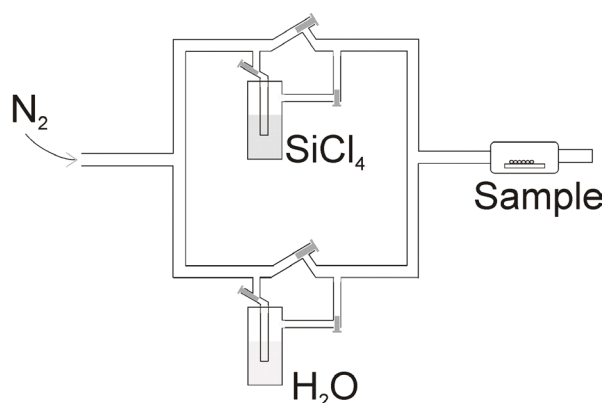


Figure 1: Diagram of chemical vapour deposition set-up.

Next, the container with the SiCl<sub>4</sub> is bubbled (100 mL/min N<sub>2</sub> flow) for a period of 30 seconds. The hydrolysis of SiCl<sub>4</sub> takes place on the sphere surface and SiO<sub>2</sub> forms in a laminar way around them. Under these conditions the pore filling could be controlled in steps of ~5% for spheres 1090 nm in diameter.

After taking away the sample, a N<sub>2</sub> purge (200 mL/min) is used to sweep the possible remnants from the set up as a previous step to a new cycle.

---

<sup>1</sup> Miguez, H., *et al.* “Mechanical stability enhancement by pore size and connectivity control in colloidal crystals by layer-by-layer growth of oxide.” *Chemical Communications*, 2736-2737 (2002).

<sup>2</sup> E. Palacios-Lidón, “*Caracterización óptica de sistemas fotónicos basados en ópalos*”, PhD Thesis, Universidad Autónoma de Madrid, Madrid (2004)

## Conclusiones generales:

- Se han fabricado ópalos artificiales de esferas de poliestireno en lámina delgada sobre diferentes sustratos mediante el método de la deposición vertical. Una caracterización estructural de los mismos mediante diversas técnicas ha permitido obtener información sobre la forma en que estas muestras crecen así como su orientación cristalográfica. Esto ha facilitado una posterior caracterización óptica.
- Se ha estudiado la respuesta óptica de ópalos artificiales de poliestireno en lámina delgada en la región de bajas energías mediante espectroscopias de reflexión y transmisión. Se ha encontrado que los efectos de finitud en la respuesta óptica de este tipo de muestras desaparecen con 35 capas de esferas. Los resultados se han reproducido cualitativamente con un modelo basado en la aproximación de onda escalar.  
Se ha estudiado el efecto del desorden en la respuesta óptica. Se ha encontrado que la variación espectral de la intensidad difusa producida por defectos estructurales depende de las bandas de energía.  
Se ha medido la reflexión a lo largo de trayectorias que unen direcciones de alta simetría. Los resultados coinciden con la estructura de bandas.
- Se ha estudiado la respuesta óptica en la zona de altas energías para ópalos artificiales en lámina delgada. Se ha relacionado la difracción con bandas de energía. La respuesta óptica en esta región presenta un comportamiento complejo, determinado por la interacción entre las bandas asociadas a la difracción y aquellas asociadas a la propagación en la dirección de incidencia.
- Se han presentado medidas de interferometría con luz blanca en ópalos artificiales en lámina delgada. Las medidas han permitido obtener la fase acumulada, a partir de la cual se ha obtenido la velocidad de grupo.  
En la zona de baja energía se ha extraído de la fase un índice de refracción efectivo que presenta una región de dispersión anómala. La velocidad de grupo en esta región se explica con las bandas de energía y corrobora el comportamiento de la intensidad difusa.  
En la zona de altas energías la velocidad de grupo presenta un comportamiento complejo con valores mayores que  $c$  e incluso negativos. Esta respuesta coincide con la presencia de bandas asociadas a la difracción.
- Se ha estudiado la respuesta óptica de ópalos artificiales en volumen para direcciones diferentes a la incidencia normal mediante espectroscopia de reflexión. Se ha verificado su dependencia con la polarización en la región de bajas energías.
- Se ha medido la reflexión en función del ángulo sobre monodominios de ópalos inversos de  $\text{TiO}_2$  en volumen. De esta forma se ha obtenido información estructural de las muestras. Asimismo se han medido valores de reflexión mucho mayores que los obtenidos con haces de mayor diámetro. Los resultados muestran acuerdo con cálculos de bandas.



## Lista de publicaciones:

Publicaciones en revistas internacionales :

Galisteo-López, J. F., García-Santamaría, F., Golmayo, D., Juárez, B. H., López, C. and Palacios-Lidón, E. “*Self-assembly approach to optical metamaterials.*” *Journal of Optics a-Pure and Applied Optics* **7**, S244-S254 (2005).

Galisteo-López, J. F., García-Santamaría, F., Golmayo, D., Juárez, B. H., López, C. and Palacios-Lidón, E. “*Design of photonic bands for opal based photonic crystals.*” *Photonics and Nanostructures – Fundamentals and Applications* **2/2**, 117-125 (2004).

Galisteo-López, J. F. and López, C. “*High-energy optical response of artificial opals.*” *Physical Review B* **70**, art. no.-035108 (2004).

Palacios-Lidón, E., Galisteo-López, J. F., Juárez, B. H. and Lopez, C. “*Engineered planar defects embedded in opals.*” *Advanced Materials* **16**, 341-345 (2004).

Galisteo-López, J. F., Palacios-Lidón, E., Castillo-Martínez, E. and López, C. “*Optical study of the pseudogap in thickness and orientation controlled artificial opals.*” *Physical Review B* **68**, art. no.-115109 (2003).

Galisteo-López, J. F., López-Tejeira, F., Sánchez-Dehesa, J. and López, C. “*Experimental evidence of polarization dependence in the optical response of opal-based photonic crystals.*” *Applied Physics Letters* **82**, 4068-4070 (2003).

Galisteo-López, J. F. and Vos, W. L. “*Angle-resolved reflectivity of single-domain photonic crystals: Effects of disorder.*” *Physical Review E* **66** (2002).

Koenderink, A. F., Johnson, P. M., Galisteo-López, J. F. and Vos, W. L. “*Three-dimensional photonic crystals as a cage for light.*” *Comptes Rendus Physique* **3**, 67-77 (2002).

Publicaciones en congresos:

Galisteo-López, J. F., García-Santamaría, F., Golmayo, D., Juárez, B. H., López, C. and Palacios-Lidón, E., “*Materials aspects of photonic crystals.*” *Proceedings of ICTON 2004, IEEE publications*, **2**, 139; ISBN 0-7803-8343-5, Wroclaw, Poland (2004).

Galisteo-López, J. F. and López C. “*In-depth study of the pseudogap in artificial opals.*” *Proceedings of SPIE* vol. **540**, p.1 (2004).

Vos, W. L., Koenderink A. F., Bechger L. and Galisteo-López J. F. “*Optical experiments on self-assembled photonic crystals.*” Abstracts of papers of the American Chemical Society, 221 U:245-246, 123-PHYS Part 2, Apr. 1 (2001).